T-3790

MODELING AND INVERSION IN THE OCEAN WAVEGUIDE USING BORN AND RYTOV APPROXIMATIONS

by

Linda Boden

ProQuest LLC.
789 East Eisenhower Parkway
P.O. Box 1346
Ann Arbor, MI 48106 – 1346

T-3790

A thesis submitted to the Faculty and the Board of Trustees of the Colorado School of Mines in partial fulfillment of the requirements for the degree of Doctor of Philosophy (Geophysical Engineering).

Golden, Colorado
Date Oct 4, 1989

Signed: Linda Boden
Linda Boden

Approved: John A DeSanto
John DeSanto
Thesis Advisor

Golden, Colorado
Date 5 October 1989

P R Romig
Dr. Philip Romig,
Professor and Head,
Geophysics Department

ABSTRACT

The deep ocean has a refractive waveguide velocity structure created by variations in temperature, salinity and pressure. Because the sound speed changes slowly with range and average depth-dependent profiles are known from measurements, an approximate solution to the acoustic field in the waveguide can be formed using perturbation techniques. We then seek to formulate a direct inversion algorithm based on the perturbative solutions. Under certain restrictions, the unknown velocity perturbations about a background profile and the scattered field data can be written as a Fourier transform pair.

In this thesis, we investigate two well-known perturbative solutions; the Born amplitude expansion and the Rytov phase expansion. The approximations, although closely related, behave quite differently depending on the size of the perturbation, the distance traveled in the perturbed media and the local field gradient. Studying the behavior of the approximations in the forward problem gives an indication of the size and type of perturbations recoverable in the inverse problem.

We begin by investigating the perturbative solution behavior for simple velocity structures. In a constant velocity or a layered waveguide, the solutions and the first order errors can be derived explicitly. Although not representative of

a true ocean, the behavior of the Born and Rytov solutions for these simple velocity structures permits us to qualitatively predict their behavior in an inhomogeneous ocean environment. Numerical examples using depth-dependent background profiles confirm that the range of validity of the distorted-wave approximations is consistent with that found in the constant background test cases.

The inverse technique consists of relating the scattered data and the perturbation as a Fourier transform pair. In order to derive the inverse relation, the phase of the transform must be monotonic. Because the energy propagates via refraction in the ocean, this criteria can not be met globally. In fact, the regions in the ocean waveguide in which the phase is monotonic are shadow zones; regions where the waveguide is not well-illuminated. In a insonified waveguide, however, the phase is not monotonic and the inversion algorithm is invalid.

Although inverse algorithms using Fourier techniques were found to be inappropriate for perturbation reconstruction in the ocean, the range of validity of the Born and Rytov propagation models in a depth-dependent environment was established. This has not been previously done, and, as a result, the knowledge obtained can be used to investigate other inverse formulations based on these perturbative solutions.

TABLE OF CONTENTS

LIST OF FIGURES

LIST OF TABLES

ACKNOWLEDGMENTS

I would like to thank the Office of Naval Research, Ocean Acoustics Division and the Naval Research Laboratory in Washington, DC for partially supporting this research. I also thank Brian Sumner for writing the plot package used in generating the graphics in this thesis.

Special thanks goes to the Center for Wave Phenomena, especially my advisor, John DeSanto, for providing support and encouragement throughout both my Master's and Ph.D. programs at the School of Mines.

Last of all, I thank my parents who always believed in me and my husband, Russell, for enduring my manic-depressive pre-Ph.D. personality. I love you, Russell.

INTRODUCTION

In the last decade, the inverse problem in the ocean has received considerable attention from the ocean acoustics and oceanographic scientific communities. In 1979, Munk and Wunsch proposed a inverse method that is now known as ocean acoustic tomography. This technique consists of measuring ray travel times between source-receiver pairs and inverting these to determine perturbations to an assumed background profile. Many experiments have been conducted proving the validity and usefulness of the technique as well as its limitations (for some of the earliest results see Spiesberger, Spindel and Metzger 1980; Brown et al. 1980; Munk and Wunsch 1982; Spiesberger 1983; Munk and Wunsch 1983). Because the travel time equations are linearized, the background or guess profile must be known to within $\sim$2 m/s of the true profile. The inversion methodology is in the class known as indirect inversion techniques; a background profile is chosen, the forward model is run repeatedly and the results compared to the experimental data. In other words, the technique is based on iteration of a forward model.

In this thesis, we attempt a different approach and formulate a direct inversion algorithm. Using first order perturbation expansions, the scattered field data as a function of frequency and the profile perturbation as a function of the phase can be directly related as a Fourier transform pair. However, because the

inversion is based on the forward model we first must investigate the range of validity of the perturbative solutions in the ocean waveguide. The theoretical analysis of the forward model is done in chapter 2 and numerical examples are presented in chapters 3 and 4.

We study two perturbative solutions; the Born amplitude expansion (Born 1926) and the Rytov phase expansion (Rytov 1937; Chernov 1960). The background field, on which the perturbative solutions are based, is chosen to be the proper mode solution; the discrete part of the normal mode solution. The normal mode representation, which contains both the discrete and continuous spectrum, is exact under certain restrictions (see chapter 1). In the far field, the continuous spectrum can be neglected and the proper or propagating modes are the main contribution to the solution.

In order to obtain simple error estimates for a waveguide geometry, we first investigate the perturbative solutions in a constant background environment. When the background is chosen to be a constant, the solutions are known simply as the Born and the Rytov approximations.

Although the maximum deviation in the sound speed in the deep ocean is only about 10% over the entire waveguide, the background velocity structure in the ocean cannot be assumed constant. Therefore, we must choose a depth-dependent background sound speed structure to obtain valid zeroth order solutions in the

refractive ocean waveguide. In this case, the perturbative approximations are called the distorted-wave Born (DWB) and the distorted-wave Rytov (DWR) to distinguish the solutions from those based on a homogeneous background.

Once the forward model has been investigated, we have an estimate of the magnitude and extent of perturbations that can be recovered in an inversion. In chapter 5, we determine the applicability of a Fourier inverse technique by studying the attributes of the transform kernel as a function of depth and frequency. Although no inversions were obtained due to phase averaging, band-limiting and stationary phase points in depth, the analysis leads to a better understanding of the type of direct inversion algorithms that could be used to reconstruct depth-dependent perturbations.

The major new work presented in this thesis is the characterization of the direct propagated acoustic field using approximation methods and the formulation of inversion representations using these approximations.

1. MODELING THE SOUND FIELD IN THE OCEAN WAVEGUIDE

1.1 Introduction

The underwater sound channel or SOFAR (Sound Fixing And Ranging) channel, discovered in the early 1940's by M. Ewing and J.L. Worzel (1948), is the most characteristic feature of the deep ocean at moderate and equatorial latitudes. This acoustic channel is formed by temperature, pressure and salinity variations in the ocean. The temperature and salinity decrease below the ocean surface causing a corresponding decrease in the sound speed. At approximately 1 kilometer (km) below the surface, a leveling off of the temperature decrease and steadily increasing pressure causes a nearly linear increase in the sound speed as the depth is further increased. Thus, an acoustic waveguide is created in which sound can propagate, through refraction, for hundreds of kilometers.

Although the ocean has both regular and random inhomogeneities, this thesis will only deal with regular or deterministic effects; in particular, propagation in the underwater sound channel. The sound field is modeled using the acoustic wave equation assuming a pressure release surface and either a rigid bottom or an infinite half space below the waveguide bottom. We will use a point cylindrical monochromatic source representation and assume the medium is cylindrically symmetric. In general, the sound speed is a function of both depth and range.

In the next section, we briefly discuss the attributes of several numerical propagation models in use today (for a summary of numerical propagation loss models, see DiNapoli and Deavenport 1979); in particular, the choice of a background model on which the perturbative solutions are based. The last section of this chapter illustrates the variation of the sound field as a function of source depth and frequency for several sound speed profiles. These plots are generated from the proper or discrete mode solution; the background model used throughout this thesis.

1.2 Numerical Models

A variety of propagation codes have been developed to model the sound field in the ocean. Each is valid within a certain range of chosen medium parameters. Including even a condensed discussion of all the computer codes currently in use is impossible. Instead, we first briefly describe two propagation loss models; the classical ray method and the parabolic approximation to the Helmholtz equation. Next, we focus on a third, the discrete mode solution, which is the background model used in this thesis. The rationale for basing the perturbative solutions on this particular model will be made clear in the remainder of this section.

The classical ray equations and the parabolic approximation are derived based on assumptions about the propagation environment. The ray equations are formed

from a high frequency assumption and by neglecting diffraction effects (Born and Wolf 1965). The parabolic equation, originated by Leontovich and Fock (1946) and introduced to the ocean acoustics community by Hardin and Tappert (1973), is based on a narrow angle approximation. In both of these cases, approximate equations are derived from the Helmholtz equation and it is from these equations that the solutions are found.

The ray representation has a intuitive geometric appeal. Rays are lines orthogonal to the wavefronts and so point in the direction of propagation. The rays can be found from the eikonal equation independent of the amplitude. The amplitude can be calculated by finding the intensity along each ray assuming no coupling between rays. However, the theory is invalid in shadow zones (regions in which trapped rays do not penetrate) and near caustics (envelopes of the family of rays) because the diffraction effects are neglected in deriving the equations. As the range increases, the caustic regions become wider, further limiting the applicability of ray theory. In addition, the eikonal and transport equations are derived under the high frequency assumption; the length scales in the problem must be much greater than the wavelength of sound. By studying the ray-mode connection, corrections have been made to increase the accuracy of the ray models (Pedersen and Gorden 1972) or alternately, a hybrid ray-mode propagation model can be implemented (Kamel and Felsen 1982). Nonetheless, in order to avoid the limitations of ray theory, we turn to full-wave representations of the field.

The parabolic approximation to the Helmholtz equation is based on narrow angle assumption. The limited angular aperture, characteristic of long range sound propagation in the ocean, makes a parabolic approximation ideal for the deep ocean environment. Another advantage of the parabolic equation solution is that it is numerically solved using the split-step algorithm, which permits the solution to be marched in range. However, the parabolic is exact only for horizontal rays; any angle off the horizontal results in a distortion of the modal phase which increases with range (Brekhovskikh and Lysanov 1982). As with the ray equations, corrections have been made to the parabolic which reduce the phase error substantially (DeSanto, Perkins and Baer 1978), but nonetheless, the solution is derived from a parabolic equation instead of the elliptical Helmholtz equation.

The normal mode representation of the field is an exact solution of the Helmholtz equation if the sound speed depends only on depth and the boundaries of the waveguide are planar; parallel to the range coordinate. In the near field of the source, the normal mode solution includes both the discrete and continuous spectrum. Away from the source, however, the continuous spectrum is negligible and only the propagating modes contribute significantly to the field solution (Ewing, Jardetzky and Press 1957); accordingly, only these modes are computed numerically. As contrasted with the ray and parabolic solutions, the exact solution to the Helmholtz equation is found and then a portion of the solution discarded in the far field. The normal mode solution is accurate for all frequencies and the

proper mode solution becomes increasingly accurate the farther we are from the source (Tolstoy and Clay 1985). Because we are interested in long range low frequency sound propagation, the proper mode solution was chosen to be the background model from which the distorted-wave Born and Rytov solutions are constructed.

1.3 Examples of Waveguide Propagation

In this section, several examples of waveguide propagation are illustrated with the use of color pixel maps. The field strength in the waveguide is represented by the transmission loss in decibels (dB). The transmission loss is defined by $-20\log_{10}|P/P_{ref}|$, where P is the pressure field and P_{ref} is the field strength at 1 meter (m) from the source.

In order to illustrate the focusing effect that the SOFAR channel has on sound propagation, we compare the propagation loss in a constant velocity waveguide to that of a bilinear profile with a sound speed minimum at 1 km depth. Effects of source placement in depth and changes in the source frequency are also compared. Before illustrating the acoustic field behavior for different waveguide geometries, we first briefly discuss the discrete modal solution.

Recall that we are solving the Helmholtz equation. If the sound speed in the waveguide is constant or at most depends on depth, the homogeneous form of the

equation is separable. The range solution is an outgoing wave Hankel function. The vertical wave function, ψ, satisfies the equation

$$\left[\frac{d^2}{dz^2} + \left(k_o^2 n^2(z) - \xi^2\right)\right]\psi = 0$$

with boundary conditions at the surface and bottom of the ocean. The index of refraction, $n(z)$, is given by $c_o/c(z)$ and the reference wavenumber is $k_o = 2\pi f/c_o$; c_o is the reference sound speed, usually chosen as the minimum value in the waveguide, $c(z)$ is the depth-dependent sound speed and f is the source frequency. Because we are solving a boundary value problem, there are non-trivial solutions, ψ_n only for a discrete set of values of the parameter, ξ_n. Therefore, the ψ_n are the eigenfunctions and the ξ_n are the eigenvalues of the problem. As will be illustrated, the number of eigenvalues contributing to the solution depends on the boundary conditions, the source frequency and the sound speed structure in the waveguide.

Figures 1 and 2 illustrate the transmission loss in a constant velocity waveguide for source frequencies of 25 and 100 Hertz (Hz), respectively. (The maximum allowable phase velocity is chosen to be 1600 m/s.) The source is placed at a depth of 500 m. We have a pressure release surface ($P = 0$ at the ocean surface) and a hard bottom ($P_z = 0$, where the subscript denotes the depth derivative).

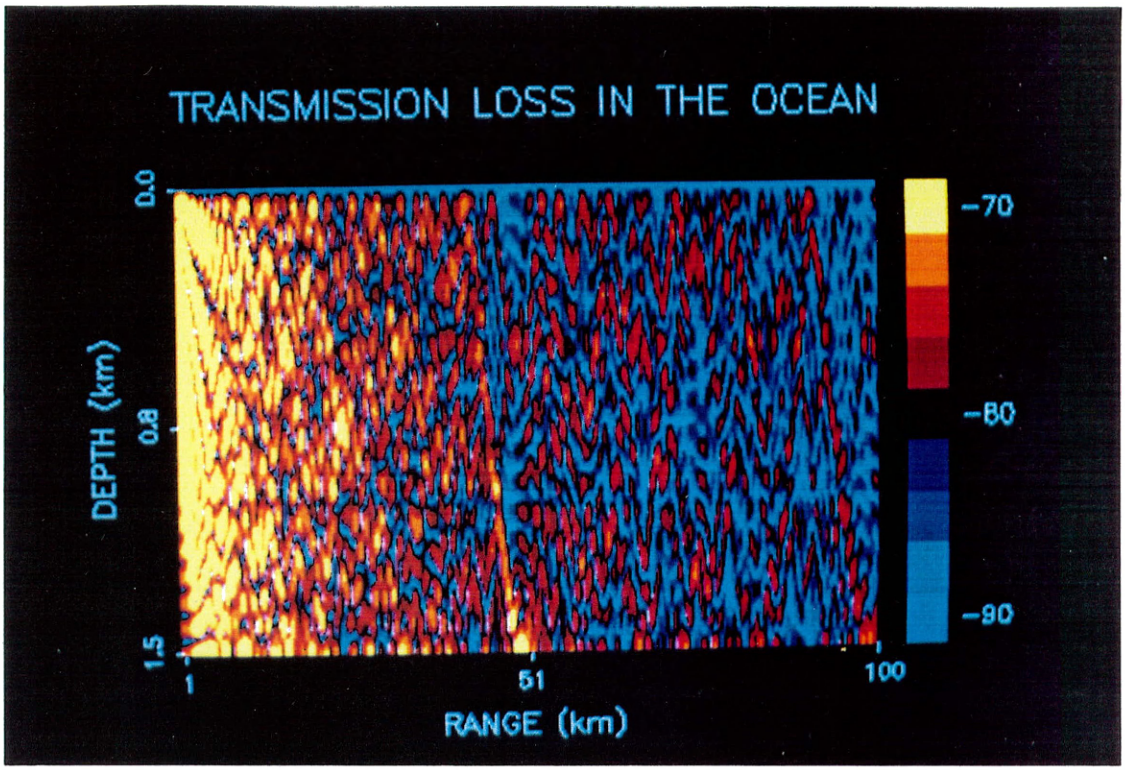

Figure 1. Transmission loss in a constant velocity waveguide. The source frequency is 25 Hz.

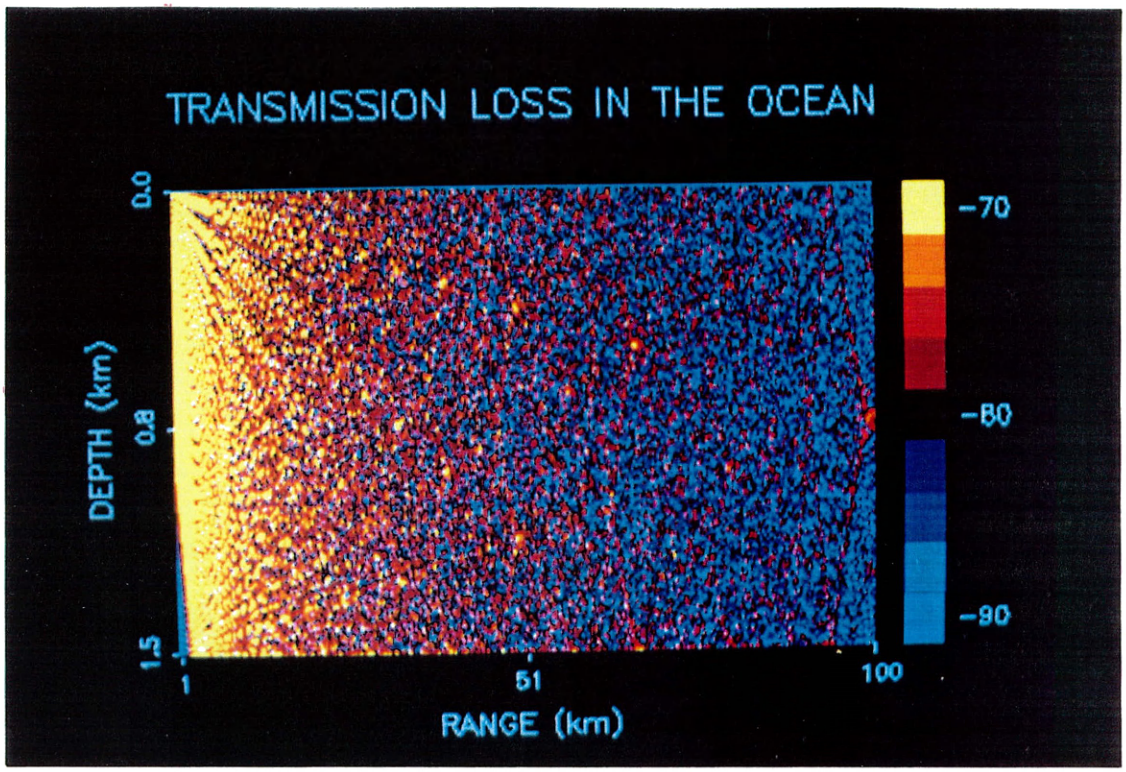

Figure 2. Transmission loss in a constant velocity waveguide. The source frequency is 100 Hz.

Because the velocity is constant over the full waveguide, there is no refraction; the energy propagates through surface and bottom reflections. We have total internal reflection due to the bottom boundary condition; in general, the angular aperture extends from 0 to $\pm 90^\circ$ measured from the horizontal at the source position. As is evident from the isolated bright spots, the energy focuses only locally.

The different structure in Figures 1 and 2 is due solely to the change in source frequency. At 25 Hz, there are 50 modes contributing to the field, while at 100 Hz, we have 4 times as many. A higher source frequency does not imply higher angles but instead, results in a larger number of modes in the angular aperture. This is easily seen from the relationship $k_o^2 n_c^2 = \xi_n{}^2 - \lambda_n{}^2$. In a constant velocity medium, the index of refraction, n_c, is 1, so that horizontal wavenumber eigenvalues are given by $\xi_n{}^2 = k_o^2 - \lambda_n{}^2$. The λ_n vertical wavenumbers are given explicitly by $\lambda_n = (2n-1)\pi/2h$ where h is the width of the waveguide and n = 1,2,... If $\xi_{\min} = 0$, we have only vertical propagation (the takeoff angle is $\pm 90^\circ$) and $k_o = (2N-1)\pi/2h$ so N = number of propagating modes = $k_o h/\pi + 1/2$. Determining N for source frequencies of 25 and 100 Hz using this equation, results in the above values of 50 and 200 modes, respectively.

We now look at sound propagation in a refractive waveguide. In this case, the waveguide lies over an infinite half-space having a sound speed that matches the

sound speed at the bottom of the waveguide. Therefore, there are no bottom reflections; only surface reflections and refraction. Illustrated in Figure 3 is the sound speed profile used to generate the plots in Figures 4, 5, and 6. Figures 4 and 5 are the transmission loss plots for source frequencies of 25 and 100 Hz, respectively. The source is placed on the channel axis at 1 km. The number of propagating modes is found to be 16 (Tolstoy and Clay 1987) in Figure 4 and 64 in Figure 5. In these examples, the number of modes depends on the change in sound speed above and below the channel axis, the distance of the channel axis from the surface and bottom of the ocean and, of course, the source frequency.

In contrast with the constant velocity waveguide, the refraction and

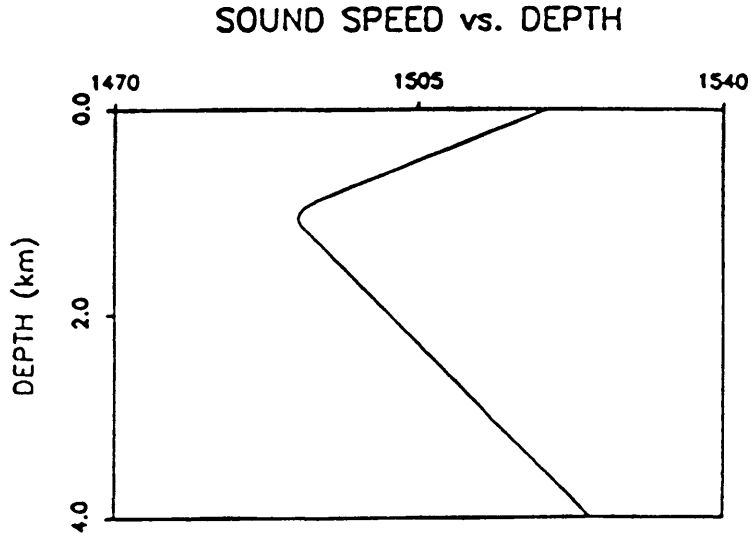

Figure 3. Sound speed profile used in generating the results in Figures 4, 5 and 6. We assume an infinite half-space below the waveguide in which the sound speed is constant and matches the sound speed at the bottom of the waveguide.

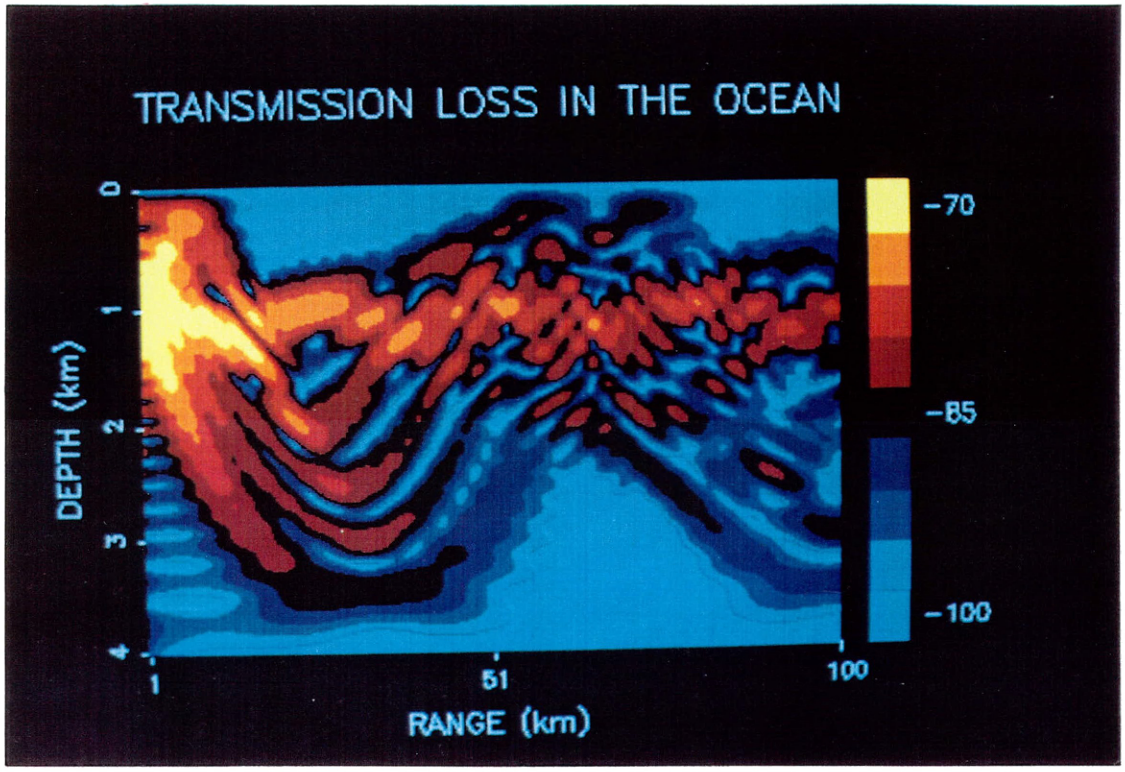

Figure 4. Transmission loss in a refractive medium generated using the profile in Figure 3. The source is placed on the channel axis at 1 km and the source frequency is 25 Hz.

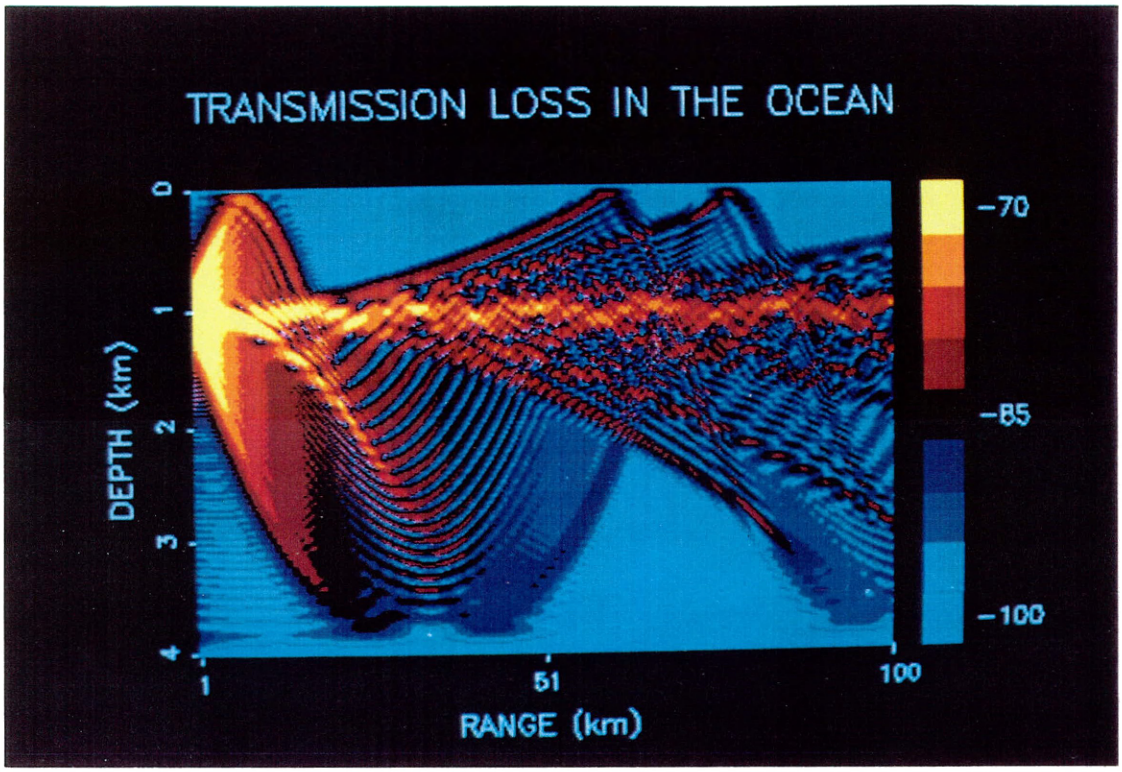

Figure 5. Transmission loss in a refractive medium generated using the profile in Figure 3. The source is placed on the channel axis at 1 km and the source frequency is 100 Hz.

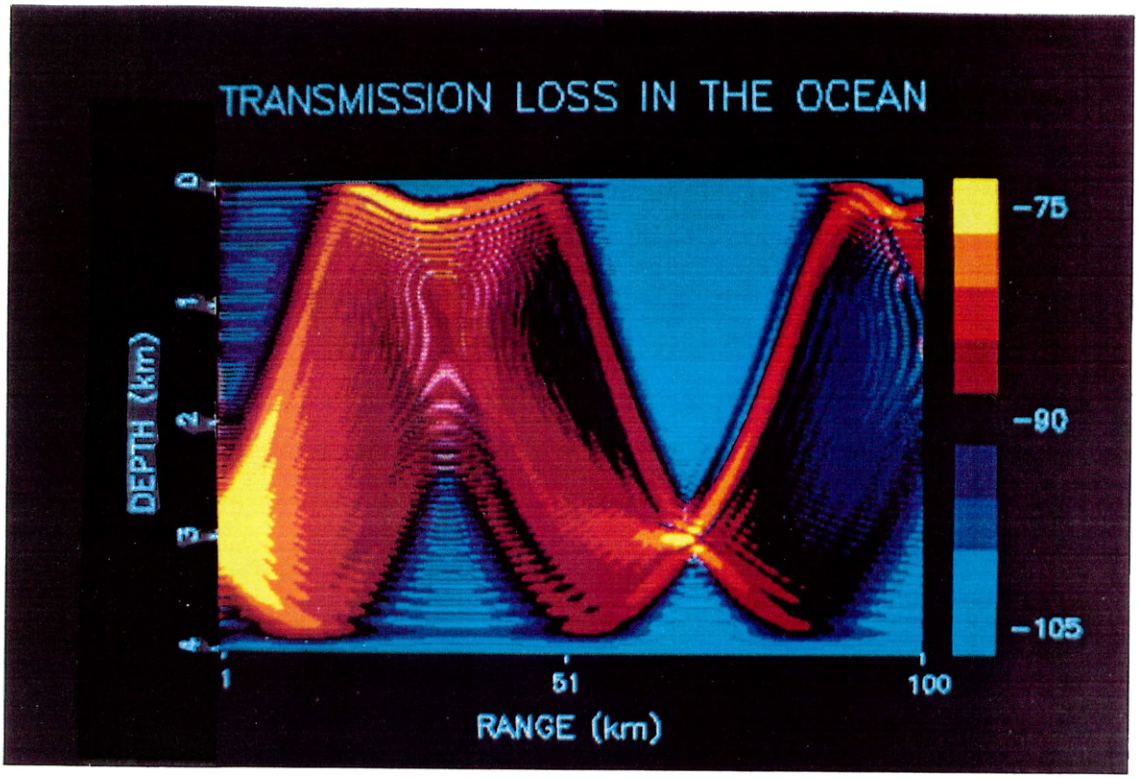

Figure 6. Transmission loss in a refractive medium generated using the profile in Figure 3. The source is placed at a depth of 3 km and the source frequency is 100 Hz.

channeling of the energy is clearly seen. Because the source is placed on the channel axis, a large portion of the energy is propagating at nearly horizontal angles with very little loss. It is also interesting to note the distinct ray-like structure of Figure 5 as compared to Figure 4. As is well-known, a ray is the locus of neighboring modes propagating in phase (Officer 1958; Tolstoy and Clay 1966), and the higher the frequency, the greater the number of modes. Therefore, we obtain a ray-like picture of the acoustic field.

Figure 6 illustrates the effect of moving the source below the channel axis; the source is now located at a depth of 3 km. Although the waveguide is still refractive, the source placement prohibits the trapping of energy in the vicinity of the channel axis. The beam has narrowed and the width of the shadow zones has increased. Instead of focusing over the entire range of propagation as in Figure 5, the energy is locally focused at the source depth, at 65 km in range.

As illustrated in the previous three figures, the deep ocean waveguide is an inhomogeneous environment in which sound propagates mainly through refraction. This is contrasted with the field structure in a constant velocity waveguide in which the energy propagates via reflection from the waveguide boundaries. In a waveguide with a refractive velocity profile, the field structure depends on the source frequency, the sound speed gradient and the source placement with respect to the channel axis. If the source is placed in the vicinity of the channel axis the

waveguide will be well-illuminated. As we move the source away from the axis, the energy is progressively restricted to a narrower angular aperture and as a result, the width of the shadow zones increases.

In subsequent chapters, we will investigate the behavior of two perturbative solutions to the total acoustic field in which the background solution is chosen to be the discrete part of the normal mode representation. Although the solutions and their errors are initially analyzed in several constant velocity waveguides, we stress that a constant background solution is not a valid zeroth order solution in a refractive ocean waveguide. The analysis is done simply to better understand and predict the validity of the solutions in the inhomogeneous ocean environment.

2. THE FORWARD MODEL

2.1 Introduction

The pressure field, P, in the ocean, can be shown to satisfy the inhomogeneous Helmholtz equation. In general, closed form solutions cannot be found due to complicated velocity structures. Instead, approximate solutions are constructed based on our knowledge of the characteristics of the medium in which the wavefield is propagating.

One method used in analyzing differential equations is perturbation theory. Perturbation theory permits the formulation of approximate solutions if 1) a small parameter, ϵ, can be identified in the differential equation, 2) a zeroth order ($\epsilon = 0$) solution can be found and 3) the true solution is closely approximated by the first several terms in the perturbation series (Bender and Orszag 1978). Therefore, in solving the Helmholtz equation for an arbitrary velocity model using perturbation techniques, we must be able to construct a background solution which is close to the true solution or equivalently, the guess profile must be close to the true profile. It is important to note that although the field is expanded in a perturbation series in ϵ, this is for convenience only. The actual small parameter is later identified as the difference in the true and background refractive indices and ϵ will be set equal to 1.

Because the ambient range variability in the ocean is at most a few percent of the depth variability, the background profile is chosen to be strictly depth-dependent. The pressure field or zeroth order solution in this environment can be written as a modal sum if the receiver is in the far field of the source. The background solution in this thesis is computed using the Kraken normal mode code (Porter 1985) and we perturb around this solution to form an approximation to the total field. This is a major difference in approach from that generally used in other disciplines such as atmospheric wave propagation and seismic exploration. A constant background assumption will not give the correct zeroth order physics in the ocean.

Two perturbation expansions are investigated in this thesis. The first, the distorted-wave Born (DWB) solution, is formed by expanding the amplitude of the field, and the second, the distorted-wave Rytov (DWR) by expanding the complex phase. Although the DWB and DWR solutions are derived for arbitrary depth and range-dependent profiles, only constant velocity and depth-dependent examples are investigated numerically.

2.2 The Background Solution

The acoustic field in the ocean satisfies the inhomogeneous Helmholtz equation

$$\left[\nabla^2 + k_o^2 n^2(r,z)\right] P(k_o,r,r_o,z,z_o) = -\frac{\delta(r-r_o)\delta(z-z_o)}{2\pi r} \tag{1}$$

in cylindrical coordinates. $P(k_o,r,r_o,z,z_o)$ is the total acoustic pressure field that we wish to approximate, ∇^2 is the cylindrical Laplacian, $n(r,z) = c_o/c(r,z)$ is the normalized sound speed in a depth and range dependent environment, and $k_o = \omega/c_o$ is the reference wavenumber. The source is located at a range $r = r_o$ and a depth $z = z_o$. We consider the general case of $r_o \neq 0$ in order to construct the scattered field.

The choice of the reference sound speed, c_o, is arbitrary. Because the Helmholtz equation is independent of c_o, so are its solutions. From this it follows that any approximate solution must depend only weakly on the choice of the reference sound speed in order to be a valid representation of the total field.

The distorted-wave perturbative solutions are derived with the assumption that information regarding the gross (i.e. purely depth-dependent) sound speed structure of the ocean waveguide is known. Using this knowledge, a background field, $P_o(k_o,r,r_o,z,z_o)$, which satisfies

$$\left[\nabla^2 + k_o^2 n_o^2(z)\right] P_o(k_o,r,r_o,z,z_o) = -\frac{\delta(r-r_o)\delta(z-z_o)}{2\pi r}, \tag{2}$$

can be calculated. Since $n_o(z)$ is known, the P_o field can be thought of as an *incident* field in this inhomogeneous environment. Because the oceanic sound speed structure has an inherent depth variability, but depends weakly on range, the

background, $n_o(z)$, is chosen to be strictly depth-dependent, but is 'close' (in a sense specified below) to the true index of refraction, $n(r,z)$, for all ranges and depths. By perturbing around the incident field solution, approximate solutions to the total field can be formed.

2.3 The Distorted-Wave Born (DWB) Solution

The DWB solution is formed by expanding the total field, $P(k_o,r,r_o,z,z_o)$, and the index of refraction, $n^2(r,z)$, in powers of a small parameter, ϵ. The total field, which satisfies Eq. (1), is written as

$$P(k_o,r,r_o,z,z_o) = P_o + \epsilon P_1 + \cdots \tag{3}$$

and the square of the index of refraction as

$$n^2(r,z) = n_o^2(z) + \epsilon n_1(r,z) + \cdots \tag{4}$$

Substituting Eqs. (3) and (4) into Eq. (1), equating powers of ϵ and retaining terms only up to $O(\epsilon)$ results in two equations. The $O(\epsilon^o)$ equation is Eq. (2). and the $O(\epsilon)$ equation is

$$\left[\nabla^2 + k_o^2 n_o^2(z)\right] P_1(k_o,r,r_o,z,z_o) = -k_o^2 n_1(r,z) P_o \,. \tag{5}$$

Because Eq. (5) is the Helmholtz equation with a source term, and our Green's function is the incident field, P_o, the solution to Eq. (5) is formed by integrating over all source points. The field solution is independent of theta due to cylindrical

symmetry. Performing the theta integration we obtain

$$P_1(k_o,r,r_o,z,z_o)$$

$$= 2\pi k_o^2 \int_0^\infty \int_0^h P_o(k_o,r,r',z,z') n_1(r',z') P_o(k_o,r',r_o,z',z_o) r' dr' dz' \qquad (6)$$

for the first term in the perturbation expansion. Therefore, to first order in ϵ, the total field is given by

$$P(k_o,r,r_o,z,z_o) \sim P_1^{(B)}(k_o,r,r_o,z,z_o) = P_o + \epsilon P_1 , \qquad (7)$$

where $P_1^{(B)}(k_o,r,r_o,z,z_o)$ is defined as the *first* DWB approximation to the field (e.g. Butkov 1968). Because P_1 is commonly called the *scattered* field, Eq. (7) is rewritten as

$$P_1^{(B)}(k_o,r,r_o,z,z_o) = P_o + P_s . \qquad (8)$$

where ϵ has now been set equal to 1.

The validity of the approximation is based on the assumption that the total field is close to the incident field. Equivalently, $| P_s/P_o |$ must be much less than 1; i.e. the scattered field is small compared to the incident field. The accuracy of the approximation depends on the size of the perturbation, the propagation distance in the perturbed medium and the source frequency. We discuss this further below.

2.4 The Distorted-Wave Rytov (DWR) Solution

The *first* DWR approximation is simply related to the *first* DWB and can therefore be derived from Eq. (8) (Fiddy 1986). Dividing both sides of Eq. (8) by P_o and taking the natural logarithm gives

$$\ln\left[\frac{P_1^{(B)}}{P_o}\right] = \ln\left[1 + \frac{P_s}{P_o}\right], \tag{9}$$

or since $\ln(1+\alpha)\sim\alpha$ when $\alpha\ll 1$, we can define the *first* DWR approximation, $P_1^{(R)}$ by

$$\ln\left[\frac{P_1^{(R)}}{P_o}\right] \sim \frac{P_s}{P_o}. \tag{10}$$

Exponentiating both sides and multiplying by P_o gives the *first* DWR approximation

$$P_1^{(R)}(k_o, r, r_o, z, z_o) \sim P_o e^{\phi_1}. \tag{11}$$

where $\phi_1 = P_s/P_o$ is the first term in a formal phase expansion,

$$\Phi = \phi_1 + \phi_2 + \cdots \tag{12}$$

and ϕ_1 is $O(\epsilon)$, ϕ_2 is $O(\epsilon^2)$, etc. The full DWR field is derived in Appendix C.

Because we are mainly interested in the behavior of the first order approximations, the terms DWB and DWR will denote the first order approximations unless otherwise indicated.

2.5 Discussion of Errors

As is evident from Eqs. (7) and (11) and the derivation of the DWR from the DWB, the first order solutions are closely related. However, as derived by Keller (1969) for the constant background solutions, and by Belykin (1985) for the distorted-wave solutions, the first order relative error in the two approximations is quite different. By relating terms in the series in Eqs. (3) and (12), Beylkin establishes the relative DWB error

$$\frac{P - P_1^{(B)}}{P} = O\left[\phi_2 - \frac{1}{2}{\phi_1}^2\right], \tag{13}$$

while the relative DWR error is

$$\frac{P - P_1^{(R)}}{P} = O\left[\phi_2\right]. \tag{14}$$

Although both expressions are order ϵ^2, the DWB error has an extra term, ${\phi_1}^2$. Since (as we shall see later) both ϕ_1 and ϕ_2 depend on range to the first power, the DWB error term is $O(\epsilon^2 r^2)$, while the DWR is $O(\epsilon^2 r)$. Because of this, the amplitude of the DWB field will grow like r as we propagate in range. The DWR is expected to give a better approximation to the transmitted field.

We must keep in mind, however, that these are only first order errors and, in addition, they are based on the assumption that the scattered field is much less than the incident field. As previously discussed, the DWB requires that

$| P_s/P_o | \ll 1$ in order for the approximation to be valid. But, although the DWR was derived from the DWB using this assumption, the latter is not a necessary condition for the validity of the DWR.

However, the DWR approximation has additional terms which are not evident in the simple derivation of the DWR from the DWB. In Appendix C, where the full DWR approximation is derived, the assumption is made that the integral of $[\nabla\Phi]^2$, where Φ is the full DWR phase, is of lower order. This term will be of $O(\epsilon^2)$ only if the phase gradient is small; we can have no sharp discontinuities in the complex phase term. This makes the behavior of the DWR difficult to predict because the above error estimate is locally inaccurate if the ratio P_s/P_o is changing rapidly.

2.6 Explicit Solutions

The solution to Eq. (2) can be written in several ways. In this thesis, the incident field is written as a sum of discrete modes. The solution is accurate if we are in the far field; i.e. the continuous spectrum is negligible and only the discrete modes contribute significantly to the field. The modal solution for an arbitrary source point, derived in Appendix A, is

$$P_o(k_o,r,r_o,z,z_o) = \frac{i}{4}\sum_n \psi(z_o,\xi_n)\psi(z,\xi_n)H_o^{(2)}(\xi_n r)J_o(\xi_n r_o) \qquad r>r_o \quad (15.a)$$

$$P_o(k_o,r,r_o,z,z_o) = \frac{i}{4}\sum_n \psi(z_o,\xi_n)\psi(z,\xi_n)H_o^{(2)}(\xi_n r_o)J_o(\xi_n r) \qquad r<r_o \quad (15.b)$$

where the sum over n includes all the discrete modes. The radial wavenumber eigenvalue is ξ_n and $H_o^{(2)}(\xi_n r)$ is the outgoing wave Hankel function of zeroth order with harmonic time convention, $e^{i\omega t}$. The DWB solution is written as

$$P_1^{(B)}(k_o,r,r_o,z,z_o)$$

$$= P_o + 2\pi k_o^2 \int_o^\infty \int_o^h P_o(k_o,r,r',z,z')n_1(r',z')P_o(k_o,r',r_o,z',z_o)r'\,dr'\,dz' \,. \quad (16)$$

Substituting Eqs. (15) into (16), and setting $r_o = 0$, we obtain

$$P_1^{(B)}(k_o,r,0,z,z_o) = P_o - \frac{\pi k_o^2}{8}\int_r^\infty \int_o^h \sum_n \psi(z',\xi_n)\psi(z,\xi_n)H_o^{(2)}(\xi_n r')J_o(\xi_n r)$$

$$\cdot \sum_m \psi(z',\xi_m)\psi(z_o,\xi_m)H_o^{(2)}(\xi_m r')n_1(r',z')r'\,dr'\,dz'$$

$$- \frac{\pi k_o^2}{8}\int_o^r \int_o^h \sum_n \psi(z',\xi_n)\psi(z,\xi_n)H_o^{(2)}(\xi_n r)J_o(\xi_n r')$$

$$\cdot \sum_m \psi(z',\xi_m)\psi(z_o,\xi_m)H_o^{(2)}(\xi_m r')n_1(r',z')r'\,dr'\,dz' \,. \quad (17)$$

The range integration can be done analytically if the true profile is strictly depth-dependent and we assume this here; i.e. we set $n_1(r',z') = n_1(z')$. The range integrals, which we define as I(n,m), are evaluated for two cases; $\xi_m \neq \xi_n$ and $\xi_m = \xi_n$ (see Appendix D).

If $\xi_m = \xi_n$ in Eq. (17), then we write the solution symbolically as

$$P_1^{(B)}(k_o, r, 0, z, z_o) = P_o + P_{sn}\,. \tag{18.a}$$

P_{sn}, the scattered field term for $\xi_m = \xi_n$, is given by

$$P_{sn}(k_o, r, r_o, z, z_o) = -\frac{ik_o^2 r}{8}\int_o^h \sum_n \psi(z', \xi_n)\psi(z, \xi_n) n_1(z') \cdot \psi(z', \xi_n)\psi(z_o, \xi_n)\frac{H_1^{(2)}(\xi_n r)}{\xi_n}\, dz'\,. \tag{18.b}$$

where $H_1^{(2)}(\xi_n r)$ is the first order Hankel function. If $\xi_m \neq \xi_n$ then

$$P_1^{(B)}(k_o, r, 0, z, z_o) = P_o + P_{snm} \tag{18.c}$$

and the scattered field defined as P_{snm} is

$$P_{snm}(k_o, r, r_o, z, z_o) = \frac{ik_o^2}{4}\int_o^h \sum_n \psi(z', \xi_n)\psi(z, \xi_n)\, n_1(z') \cdot \sum_m \psi(z', \xi_m)\psi(z_o, \xi_m)\frac{H_o^{(2)}(\xi_m r)}{\xi_m^{\,2} - \xi_n^{\,2}} dz'\,. \tag{18.d}$$

The DWR, formed from the DWB as previously described, is

$$P_1^{(R)}(k_o, r, 0, z, z_o) = P_o \exp\left[\frac{P_{sn}}{P_o}\right] \tag{19.a}$$

if $\xi_m = \xi_n$. Similarly, for $\xi_m \neq \xi_n$, we obtain

$$P_1^{(R)}(k_o, r, 0, z, z_o) = P_o \exp\left[\frac{P_{snm}}{P_o}\right]. \tag{19.b}$$

In the next chapter, the above equations will be evaluated for several constant velocity profiles (i.e. the depth dependent solutions are found explicitly) and the behavior of the Born and Rytov in these simple cases is investigated. Although not representative of the velocity structure in an ocean waveguide, analyzing these cases gives an indication of how the DWB and DWR approximations will behave in a complex environment.

3. CONSTANT BACKGROUND TEST CASES

3.1 Introduction

In this chapter, the behavior of the Born and Rytov approximations in two constant velocity environments is discussed. Although a constant velocity waveguide is not representative of a deep ocean, the solutions and error estimates can be found analytically. Studying the behavior of the approximations using simple velocity models often gives an intuitive feel for how the solutions will behave in a variable velocity waveguide.

In the first example, the true and guess profile are chosen to be constant over the entire waveguide. The total field is calculated using the true profile and the incident field using the guess profile. The Born and Rytov solutions to the total field are calculated and compared with the true solution. This case indicates how the approximate solutions will behave if the incident or guess profile is different from our true profile over the width of the waveguide, or equivalently, dictates how closely our guess profile must match the true when the profile perturbation extends over the full waveguide.

The second model investigated is a two-layer waveguide. The true profile has two constant velocity layers and the first guess to this profile is a constant velocity waveguide. Although, again not representative of an ocean waveguide, this case

provides information on how the Born and Rytov approximations will behave when the difference in the true and guess fields arises from a small velocity perturbation (confined to a portion of the waveguide) about a known background. The goal in this thesis is to recover small perturbations about a depth-dependent background profile, and approximate estimates of the magnitude and spatial extent of allowable perturbations for the variable velocity case can be obtained from this example.

In both of these cases, the solutions can be found analytically and so simple error estimates can be written explicitly. In addition, the constant velocity cases serve as a check on the accuracy of the numerical calculations.

3.2 Constant Velocity Waveguide

3.2.1 Derivation of the Solutions

The total field in a constant velocity waveguide, $n(z) = n_c$, is given by

$$P(k_o, r, 0, z, z_o) = \frac{i}{4} \sum_n \frac{2}{h} \sin\lambda_n z_o \sin\lambda_n z \, H_o^{(2)}(\varsigma_n r), \tag{20}$$

where the ς_n denote the horizontal wavenumber eigenvalues for the total field and are defined by ${\varsigma_n}^2 = k_o^2 n_c^2 - {\lambda_n}^2$. The reference wavenumber is $k_o = \frac{\omega}{c_o}$ and the vertical wavenumbers are the λ_n. The sine eigenfunctions arise from a particular choice of boundary conditions. The pressure field is chosen to be zero at the

surface and the z-derivative (since we have a flat bottom) to be zero at the ocean bottom. The factor $(2/h)^{1/2}$ is the normalization constant for this set of orthonormal eigenfunctions.

The initial guess field, for the constant velocity waveguide with index of refraction, n_o is given by

$$P_o(k_o,r,0,z,z_o) = \frac{i}{4}\sum_n \frac{2}{h}\sin\lambda_n z_o \sin\lambda_n z\, H_o^{(2)}(\xi_n r)\,, \tag{21}$$

where the horizontal wavenumber eigenvalues for the background solution are given by the ξ_n which are defined by ${\xi_n}^2 = k_o^2 n_o^2 - {\lambda_n}^2$. As is evident from Eqs. (20) and (21), the eigenfunctions are identical. In a constant velocity waveguide, the only difference in the two solutions are the values of the horizontal wavenumbers.

From Eq. (17), the Born solution in a constant velocity medium is given by

$$\begin{aligned} P_1^{(B)}(k_o,r,0,z,z_o) = P_o &- \frac{k_o^2 n_1 \pi}{2h^2}\int_o^r\int_o^h \sum_n \sin\lambda_n z \sin\lambda_n z'\, H_o^{(2)}(\xi_n r) J_o(\xi_n r') \\ &\cdot \sum_m \sin\lambda_m z' \sin\lambda_m z_o\, H_o^{(2)}(\xi_m r') r'\, dr'\, dz' \\ &- \frac{k_o^2 n_1 \pi}{2h^2}\int_r^\infty\int_o^h \sum_n \sin\lambda_n z \sin\lambda_n z'\, H_o^{(2)}(\xi_n r') J_o(\xi_n r) \\ &\cdot \sum_m \sin\lambda_m z' \sin\lambda_m z_o\, H_o^{(2)}(\xi_m r') r'\, dr'\, dz' \end{aligned} \tag{22}$$

where n_1, the constant velocity perturbation, is the difference, $n_c^2 - n_o^2$, in the

squares of the true and background refractive indices.

Because the perturbation is constant, both the range and depth integrals can be evaluated explicitly. Evaluating the range integrals (see Appendix D) and following the notation of Eqs. (18), the Born scattered field for $\xi_n = \xi_m$ is

$$P_{sn}(k_o,r,r_o,z,z_o) = \frac{ik_o^2 n_1 r}{2h^2}\int_o^h \sum_n \sin\lambda_n z \sin^2\lambda_n z' \sin\lambda_n z_o \frac{H_1^{(2)}(\xi_n r)}{\xi_n}\, dz' . \qquad (23.a)$$

For $\xi_n \neq \xi_m$, we obtain

$$P_{snm}(k_o,r,r_o,z,z_o)$$

$$= -\frac{ik_o^2 n_1}{h^2}\int_o^h \sum_n \sin\lambda_n z \sin\lambda_n z' \sum_m \sin\lambda_m z' \sin\lambda_m z_o \frac{H_o^{(2)}(\xi_m r)}{\xi_m{}^2 - \xi_n{}^2} dz' . \qquad (23.b)$$

Because the eigenfunctions are orthogonal over the width of the waveguide and there is no mode coupling due to the absence of a depth-dependent perturbation, Eq. (23.b) is always zero. Evaluating the depth integral in Eq. (23.a), results in the constant velocity scattered field solution

$$P_{sn}(k_o,r,r_o,z,z_o) = \frac{ik_o^2 n_1 r}{4h}\sum_n \sin\lambda_n z \sin\lambda_n z_o \frac{H_1^{(2)}(\xi_n r)}{\xi_n} . \qquad (24)$$

Therefore, the Born and Rytov solutions are formed by substituting Eq. (24) into Eqs. (18.a) and (19.a), respectively.

The first order errors in the two solutions are discussed in the next section. Because the errors have the form of a ratio of sums, explicit expressions are found

for a single mode only. However, as will be seen in the numerical examples, the single mode error estimates closely approximate the error for the multi-modal solutions.

3.2.2 Error Analysis

As discussed in section 2.5, the first order errors can be derived in terms of the first two Rytov phase terms, ϕ_1 and ϕ_2. The first phase term in a constant velocity waveguide is just

$$\phi_1(k_o,r,0,z,z_o) = \frac{ik_o^2 n_1 r}{4h\,P_o} \sum_n \sin\lambda_n z \sin\lambda_n z_o \frac{H_1^{(2)}(\xi_n r)}{\xi_n}. \tag{25}$$

The second phase term, ϕ_2, is derived from the expression for the full Rytov solution (see Eq. C.7). Assuming that the perturbation difference, n_1, is known exactly, then to first order ϕ_2 is given by

$$\phi_2(k_o,r,0,z,z_o) = \frac{2\pi}{P_o} \int_o^\infty \int_o^h P_o(k_o,r,r',z,z') \cdot \left[\nabla\phi_1(k_o,r',0,z',z_o)\right]^2 P_o(k_o,r',r_o,z',z_o) r'\,dr'\,dz' \tag{26}$$

therefore, the gradient of ϕ_1 and the incident field, $P_o(k_o,r,0,z,z_o)$, are needed to calculate ϕ_2.

Because the phase terms have the form of a ratio of sums, a simple error estimate can not be established for all modes. However, if we choose to look at the errors for a single mode only, $P_o(k_o,r,0,z,z_o)$ can be written explicitly as

$$P_{o1}(k_o,r,0,z,z_o) = \frac{i}{2h}\sin\lambda_1 z \sin\lambda_1 z_o \, H_o^{(2)}(\xi_1 r) \tag{27}$$

where $P_{o1}(k_o,r,0,z,z_o)$ denotes the field expression for the first mode, λ_1 is the corresponding vertical wavenumber while ξ_1 is the corresponding horizontal wavenumber. This notation will be used throughout in deriving the subsequent single mode expressions.

Using Eq. (27), the first phase term can now be written

$$\phi_{11}(k_o,r,0,z,z_o) = \frac{k_o^2 n_1 r}{2\,H_o^{(2)}(\xi_1 r)} \, \frac{H_1^{(2)}(\xi_1 r)}{\xi_1} . \tag{28}$$

Using the asymptotic forms of the Hankel functions

$$H_o^{(2)}(\xi_1 r) = \left[\frac{2}{\pi\xi_1 r}\right]^{1/2} e^{-i(\xi_1 r - \frac{\pi}{4})}$$

$$H_1^{(2)}(\xi_1 r) = \left[\frac{2}{\pi\xi_1 r}\right]^{1/2} e^{-i(\xi_1 r - \frac{3\pi}{4})}, \tag{29}$$

and canceling terms, $\phi_{11}(k_o,r,0,z,z_o)$ is given by

$$\phi_{11}(k_o,r,0,z,z_o) = \frac{ik_o^2 n_1 r}{2\xi_1} \tag{30}$$

so the gradient of ϕ_{11} is just

$$\nabla\phi_{11}(k_o,r,0,z,z_o) = \frac{ik_o^2 n_1}{2\xi_1}\hat{r}\,. \tag{31}$$

Substituting Eq. (31) into Eq. (26) and evaluating the range integral for a single mode, ϕ_{21} becomes

$$\phi_{21}(k_o,r,0,z,z_o) = -\frac{k_o^2 n_1 r}{H_o^{(2)}(\xi_1 r)}\frac{H_1^{(2)}(\xi_1 r)}{\xi_1 h}\left[\frac{k_o^2 n_1}{2\xi_1}\right]^2 \int_o^h \sin^2\lambda_1 z'\,dz'\,. \tag{32}$$

Performing the depth integration and cancelling like factors, the second phase term becomes

$$\phi_{21}(k_o,r,0,z,z_o) = -\frac{irk_o^4 n_1^2}{8{\xi_1}^3} \tag{33}$$

and we can now write the first order error estimates.

From Eq. (13), the first order Born error expression for a single mode is

$$\frac{P-P_1^{(B)}}{P} = O\left[-\frac{r^2 k_o^4 n_1^2}{8{\xi_1}^2}\right] + O\left[-\frac{irk_o^4 n_1^2}{8{\xi_1}^3}\right] \tag{34}$$

and from Eq. (14), the first order Rytov error estimate is

$$\frac{P-P_1^{(R)}}{P} = O\left[-\frac{irk_o^4 n_1^2}{8{\xi_1}^3}\right]. \tag{35}$$

As discussed in section 2.5, the Born error has a term that is of the order $r^2 n_1^2$, while the Rytov error is order $r\,n_1^2$. The growth in the Born approximation to the transmitted field is well-known (e.g. Keller, 1969) and the Rytov solution is

expected to give a better approximation to the true field solution.

Although the first order error estimates suggest in general how the two solutions will behave, a modal analysis of the fields in the next section, yields the errors in the first order solutions exactly for a single mode. The errors are seen through the projection of the mode coefficient.

3.2.3 Modal Decomposition of the Born and Rytov Fields

Because the background solution is a modal representation of the field, the Born and Rytov representations to the total field can also be considered to be composed of a sum of normal modes. In general, the true mode functions would be the unknowns, but in a constant velocity waveguide the functional form of the eigenfunctions for the guess profile are identical to those of the true profile. This permits a straightforward evaluation of the errors in the Born and Rytov solutions.

From Eq. (E.5), the Born coefficient for a single mode is

$$C_{1B} = \left[\frac{2}{h}\right]^{1/2} \sin\left(\frac{\pi z_o}{2h}\right)\left[1 + \frac{irk_o^2 n_1}{2\xi_1}\right] \tag{36}$$

and Eq. (E.6) for the Rytov coefficient is

$$C_{1R} = \left[\frac{2}{h}\right]^{1/2} \sin\left(\frac{\pi z_o}{2h}\right)\exp\left[\frac{irk_o^2 n_1}{2\xi_1}\right]. \tag{37}$$

Clearly, if $\left|\frac{irk_o^2 n_1}{2\xi_1}\right| \ll 1$, then the two coefficients are the same to first order. If,

however, this quantity is not small, the Born exhibits an algebraic amplitude growth, while the Rytov error is oscillatory. Therefore, although the Born error estimates in section 3.2.2 are valid for any profile perturbation, the Rytov error estimate is correct only if the scattered field is small with respect to the incident field.

In the next section, the numerical results for a constant velocity waveguide are presented and the analytical results of this section will be verified.

3.3 Constant Velocity Waveguide Example

The parameters for the constant velocity waveguide example are given in Table 1. The true and background profiles are illustrated in Figure 7. The transmission loss curves for the profiles are illustrated in Figure 8. The transmission loss is defined as $-20\log(\frac{|P|}{|P_{ref}|})$, where P is the complex field and P_{ref} is the field at 1 meter from the source.

Because the perturbation is small and the eigenfunctions are identical in the constant velocity case, the true and background curves nearly overlay each other, except perhaps at the "nulls" where the modes have interfered destructively creating a minimum amplitude. The amplitude behavior of the Born and Rytov solutions can be qualitatively predicted by studying Figure 9; the ratios $|P_s/P_o|$ vs. range. The ratios match until approximately 5 km; this is the regime in which

Table 1. Input Parameters: Test Case 1

INPUT PARAMETERS: TEST CASE 1		
Range		1.-50. km
Source Depth		500. m
Receiver Depth		500. m
Source Frequency		25. Hz
	Depth (m)	Sound Speed (m/s)
True profile	0.	1500.
	1500.	1500.
Guess profile	0.	1501.
	1500.	1501.
Maximum Perturbation		1. m/s
Perturbation Width		1500. m

the ratio is less than 1/4. Beyond this range the Born ratio continues to grow while the Rytov peaks at a ratio of two and then begins to decrease. Although the behavior of the Born solution is easily predicted, determining the behavior of the Rytov is more difficult.

The Rytov ratio does not exhibit algebraic growth except at small ranges where both solutions are within their range of validity. From the modal decomposition in section 3.2.3, we could assume little or no amplitude error. However, neglecting the gradient of the ratio of the scattered to incident field in

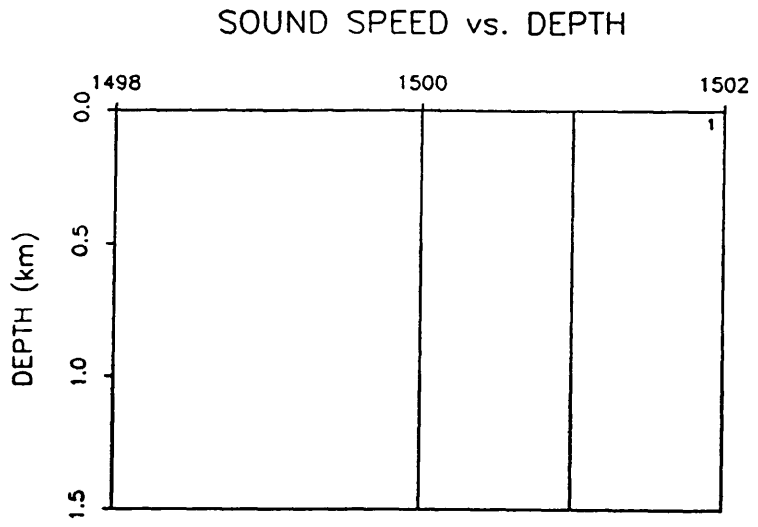

Figure 7. Constant velocity profiles. The true sound speed is 1500 m/s. The guess sound speed in 1501 m/s.

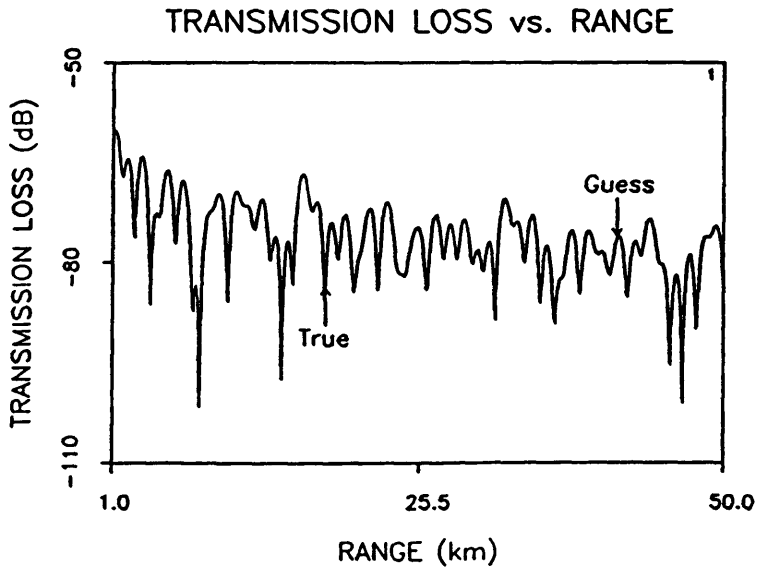

Figure 8. True and background transmission loss curves for test case 1. The curves are generated using the profiles in Figure 7. Because the eigenfunctions have the same functional form, the curves are indistinguishable.

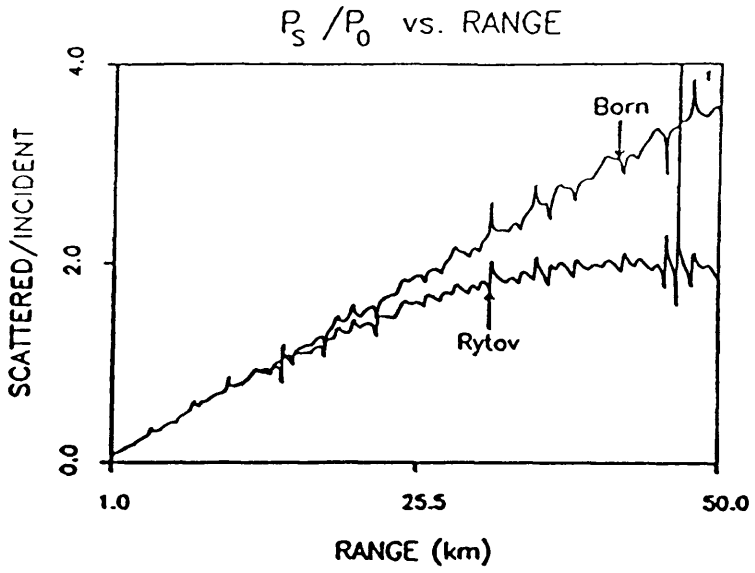

Figure 9. Ratio of the scattered field to the incident field for the Born and Rytov solutions for test case 1. The solutions are generated using the background profile in Figure 7.

this decomposition will, in some cases, cause local errors in the Rytov field. In this example, we might be inclined to predict a local error in the field solution at the spike near 50 km. However, estimating the value of the local gradient near this point, results in a value less than 1. Therefore, the Rytov solution is predicted to everywhere match the true solution.

The Born solution to the field and the true solution are illustrated in Figure 10. The growth of the Born solution with range is as predicted from the error analysis and the modal decomposition. The Rytov solution to the field and the true solution are illustrated in Figure 11. As expected from the results in the previous section and the above discussion, the Rytov exhibits no amplitude growth,

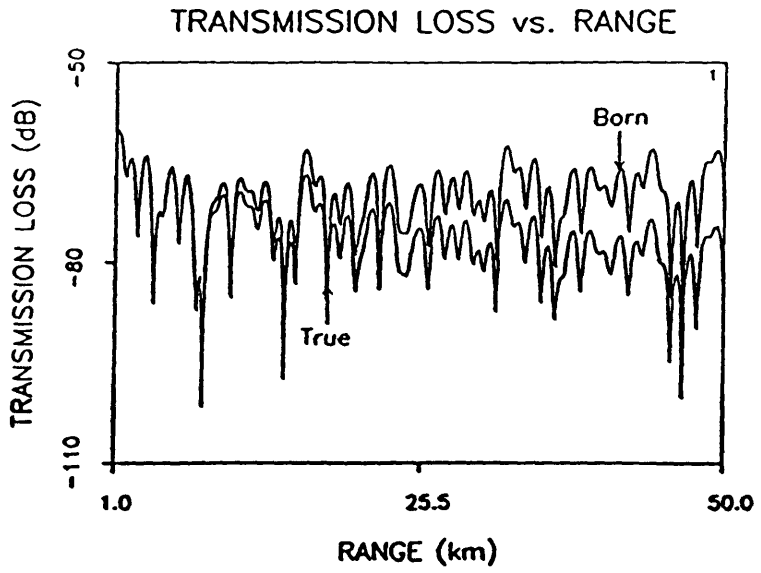

Figure 10. True and Born transmission loss curves for test case 1. The growth of the Born solution with range is clearly seen.

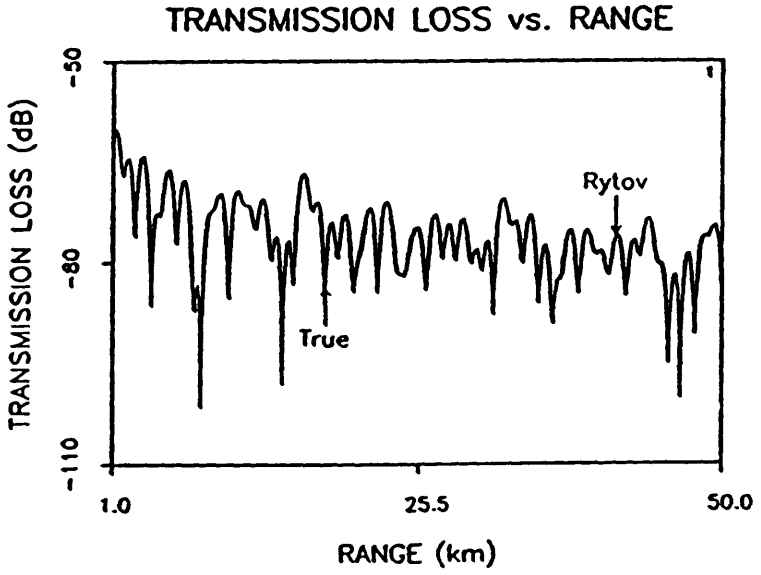

Figure 11. True and Rytov transmission loss curves for test case 1. Unlike the Born solution, the Rytov is unaffected by the extent of the perturbation.

and matches the true profile almost exactly.

The behavior of the approximations is clearly demonstrated by viewing the relative error in the transmission loss of the background, the Born and Rytov solutions (see Figure 12) with respect to the true transmission loss. The Rytov solution is the best fit; the small variations of the guess from the true have been smoothed. However, for large r, the relative error in the Born transmission loss grows approximately like $\frac{2\log(n_1\xi_1 r)}{\log \xi_1 r}$ as we propagate in range. This estimate is obtained from the single mode solution. For a single mode, the amplitude behavior with range for the true transmission loss is roughly $\log[1/(\xi_1 r)^{1/2}]$ and for the

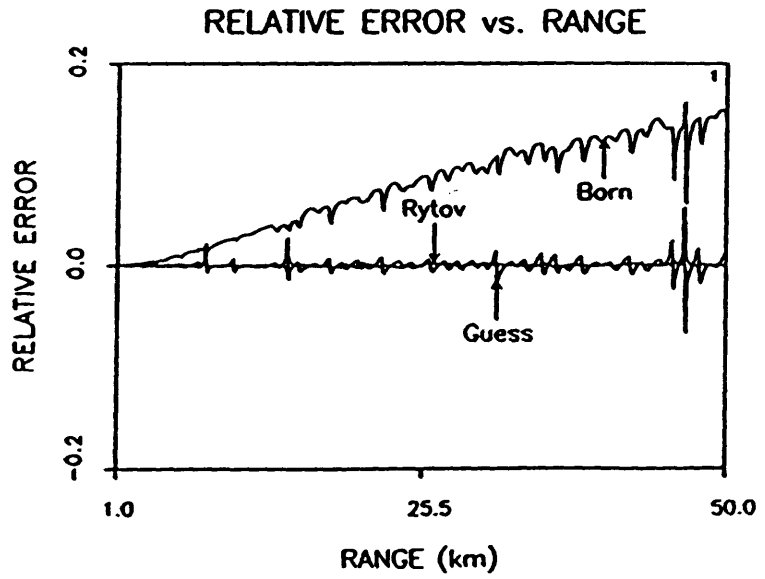

Figure 12. Relative error in the background, Born and Rytov transmission loss curves for test case 1. The Born error is approximately 17% at 50 km. The error in the Rytov solution is approximately zero over the entire range of propagation.

Born transmission loss is $\log[1/(\xi_1 r)^{1/2}\,(1+r^2 k_o^4 n_1^2/\xi_1^2)^{1/2}]$. By assuming $k_o \sim \xi_1$ and canceling terms, we obtain the above expression for the relative error.

To further confirm the results of the modal decomposition, we present some numerical examples. Figures 13 and 14 illustrate the results of the Born and Rytov modal decompositions, respectively, for a single mode. The amplitude of the Born coefficient and the real part of the Rytov coefficient confirm the validity of the expressions for the mode coefficients in the previous section. The amplitude of the Born coefficients grows with range while the error in the real part of the Rytov coefficients oscillate between 0 and 200 percent. On the other hand, the error in the real part of the Born coefficients remains stable about zero as does the amplitude of the Rytov coefficients.

To confirm that the multi-mode behavior matches that of the single mode, a modal decomposition of the solutions using the first seven modes is illustrated in Figures 15 and 16 over a range of 1-20 km. So, even for multiple modes, the errors predicted by the single mode decomposition are qualitatively correct. The accuracy of the multi-mode decompositions is verified by forming the transmission loss using the recalculated Born and Rytov coefficients.

The real part of the Born coefficients are used to recalculate the Born transmission loss. The resultant curve, labeled "MDB" is illustrated in Figure 17 along with the true transmission loss and the original Born solution. As expected,

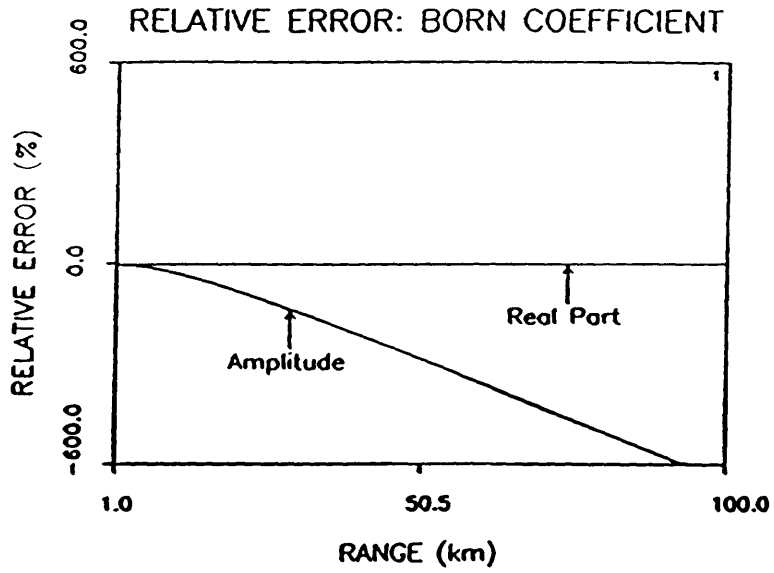

Figure 13. Relative error in the amplitude and real part of the Born mode coefficient for a single mode in test case 1. The real part of the Born coefficient is identically equal to the true coefficient.

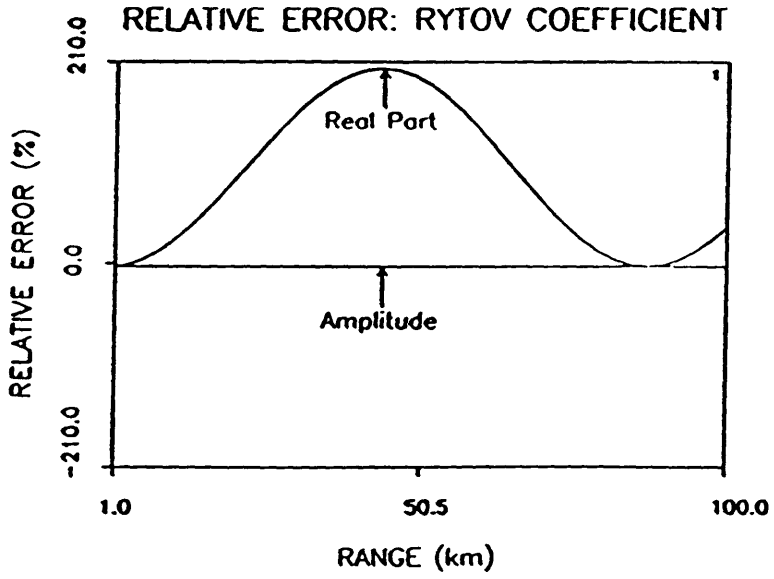

Figure 14. Relative error in the amplitude and real part of the Rytov mode coefficient for a single mode in test case 1. The amplitude of the Rytov coefficient is identically equal to the true coefficient.

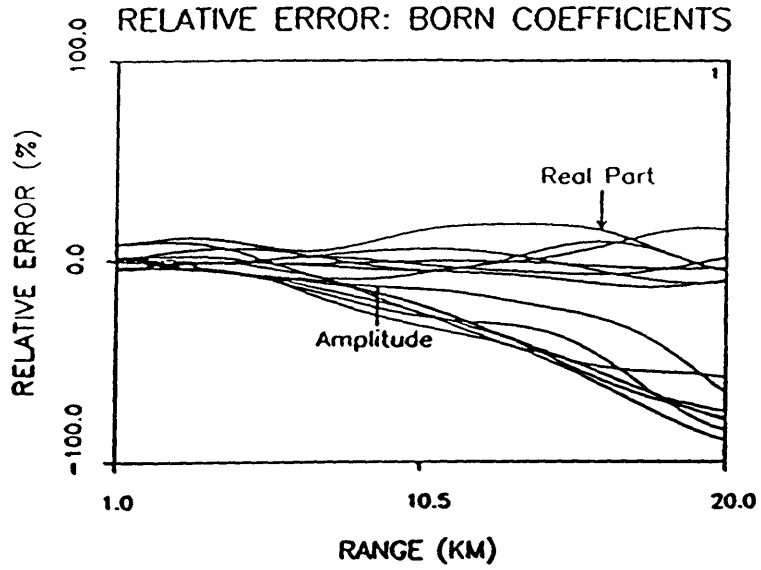

Figure 15. Relative error in the amplitude and real part of the Born mode coefficient for the first seven modes in test case 1.

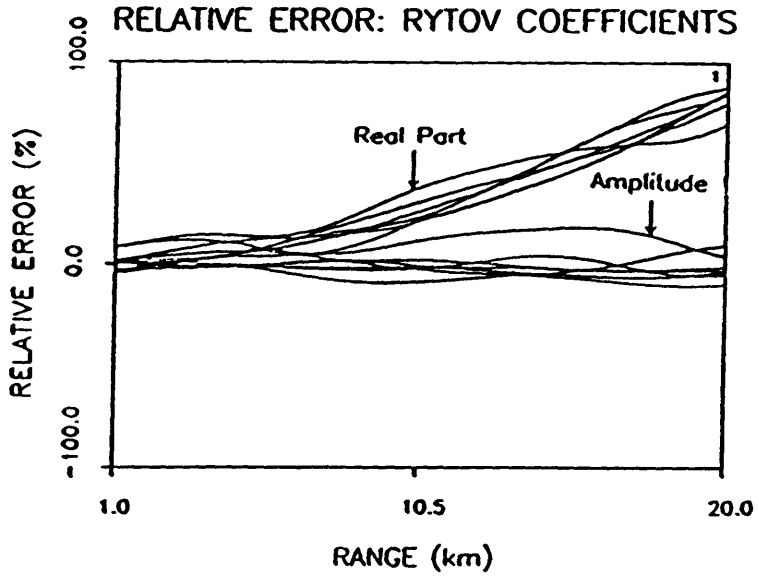

Figure 16. Relative error in the amplitude and real part of the Rytov mode coefficient for the first seven modes in test case 1.

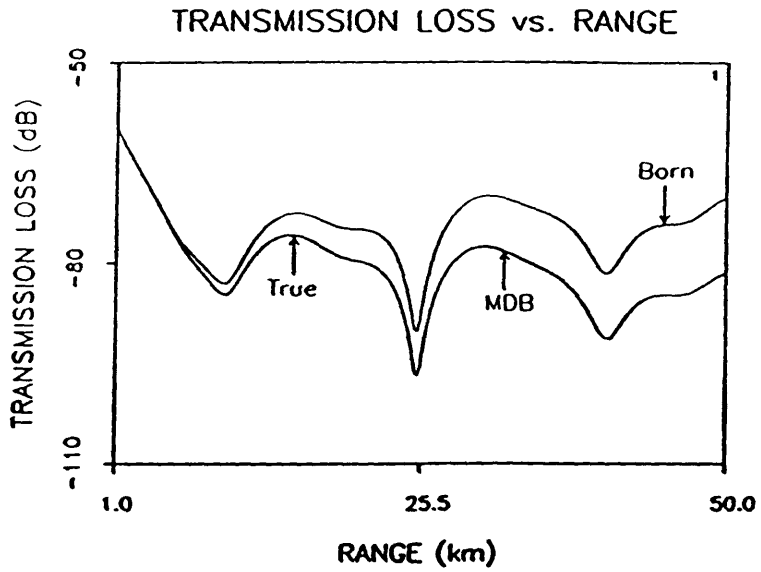

Figure 17. True, Born and the reconstructed Born transmission loss curves generated using the first seven modes in test case 1. The reconstructed Born solution is calculated using the real part of the projected mode coefficients.

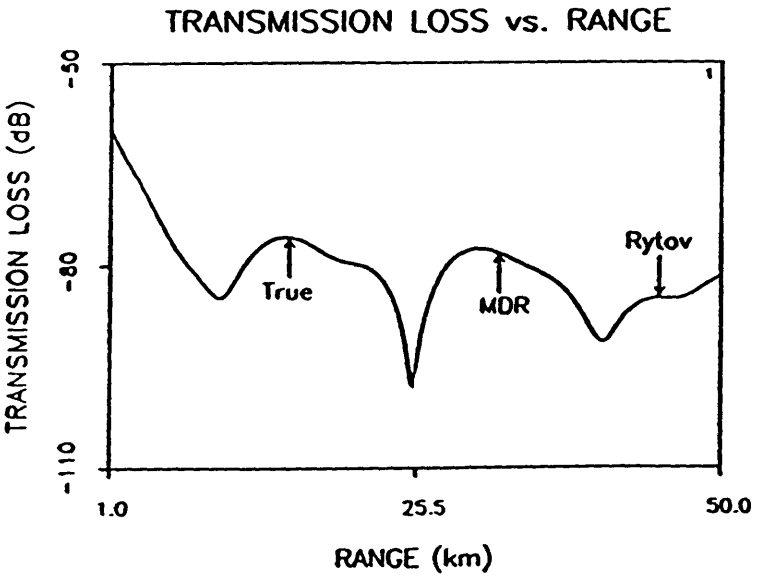

Figure 18. True, Rytov and the reconstructed Rytov transmission loss curves generated using the first seven modes in test case 1. The reconstructed Rytov solution is calculated using the amplitude of the projected mode coefficients.

the growth of the Born solution with range has disappeared. To recalculate the Rytov solution, we use the amplitude of the mode coefficients. The result, illustrated in Figure 18, and labeled "MDR" exhibits little change from the original Rytov solution.

In reviewing the results of this section, we conclude that although the amplitude of the Born approximation is strongly affected by a shift in the sound speed over the full waveguide, the Rytov approximation is insensitive to a perturbation of this magnitude and extent. In the next section, we study several two-layer waveguides in order to determine the magnitude and extent of perturbations recoverable about a known background profile.

3.4 Two-Layer Waveguide

3.4.1 Derivation of the Solutions

The two-layer model used in this section is illustrated in Figure 19. The sound speed in the upper layer is defined to be c_1, while the sound speed in the lower layer is defined to be c_o, to match the constant velocity case. The reference wavenumbers are k_1 and k_o, respectively. The depth of the layer is z_1. The total field for this geometry is

$$P(k,r,0,z,z_o)$$

$$= \frac{i}{4}\sum_n A_n \frac{\cos\lambda_{on}(h-z_o)\cos\lambda_{on}(h-z_1)}{\sin\lambda_{1n}z_1}\sin\lambda_{1n}z\, H_o^{(2)}(\zeta_n r) \qquad 0<z<z_1$$

$$P(k,r,0,z,z_o)$$

$$= \frac{i}{4}\sum_n A_n \cos\lambda_{on}(h-z_o)\cos\lambda_{on}(h-z)\, H_o^{(2)}(\zeta_n r) \qquad z_1<z<h \tag{38}$$

where A_n is given by

$$A_n = 2\lambda_{1n}\lambda_{on}\sin^2\lambda_{1n}z_1$$

$$\cdot\left[\lambda_{on}\cos^2\lambda_{on}(h-z_1)\left(z_1\lambda_{1n} - \sin\lambda_{1n}z_1\cos\lambda_{1n}z_1\right)\right.$$

$$\left. + \lambda_{1n}\sin^2\lambda_{1n}z_1\left[(h-z_1)\lambda_{on} + \sin\lambda_{on}(h-z_1)\cos\lambda_{on}(h-z_1)\right]\right]^{-1} \tag{39}$$

Again, the ζ_n are the horizontal eigenvalues for the total field, and are defined by

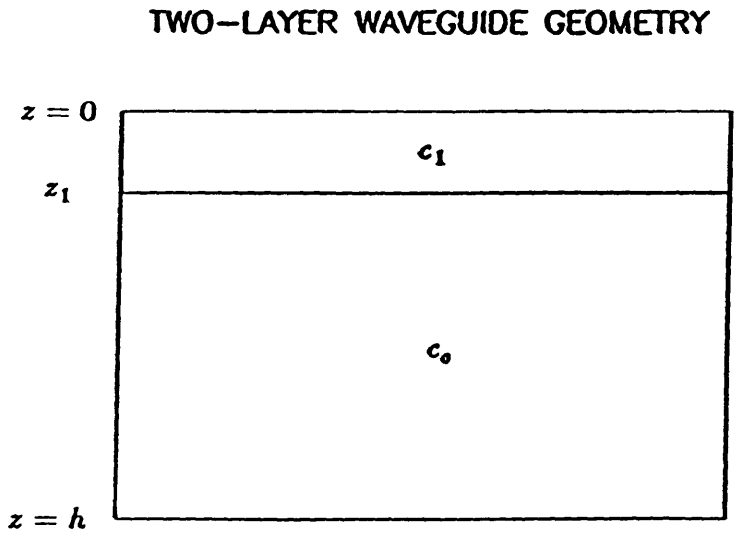

Figure 19. Two-layer geometry used in test cases 2 and 3.

$$\varsigma_n^2 = k_o^2 n_1^2 - \lambda_{1n}^2 \quad 0<z<z_1; \qquad \varsigma_n^2 = k_o^2 n_o^2 - \lambda_{on}^2 \quad z_1<z<h\,.$$

The initial guess field, calculated using a constant velocity waveguide, with index of refraction, n_o, is given in Eq. (21). Note, that although the eigenvalues in the lower layer in the total field are given in terms of k_o, they are not identical with those in the constant velocity case. The eigenvalues for the background profile are still given by $\xi_n^2 = k_o^2 n_o^2 - \lambda_n^2$.

The Born solution is given by Eqs. (18) where the integration is now over the support of the perturbation in depth, from 0 to z_1. Because the background eigenfunctions are not orthogonal over the perturbation extent in depth, Eq. (18.d) is non-zero in this example. The depth integral can still be evaluated in this case. The scattered Born solution for $\xi_n = \xi_m$ is given by

$$P_{sn}(k_o,r,r_o,z,z_o) = \frac{ik_o^2 n_1 r}{2h^2}\sum_n \left[\frac{z_1}{2} - \frac{1}{4\lambda_n}\sin 2\lambda_n z_1\right] \cdot \sin\lambda_n z \sin\lambda_n z_o \frac{H_1^{(2)}(\xi_n r)}{\xi_n}\,. \tag{40.a}$$

For $\xi_n \neq \xi_m$ the solution is

$$P_{snm}(k_o,r,r_o,z,z_o) = -\frac{ik_o^2 n_1 r}{h^2}\sum_n\sum_m \sin\lambda_n z \sin\lambda_n z_o \frac{H_o^{(2)}(\xi_m r)}{\xi_m^2 - \xi_n^2} \cdot \left[\frac{\lambda_m \cos\lambda_n z_1 \sin\lambda_m z_1 - \lambda_n \cos\lambda_m z_1 \sin\lambda_n z_1}{\lambda_n^2 - \lambda_m^2}\right]. \tag{40.b}$$

Analogous to the constant velocity example, the Born solution is formed by

substituting the scattered field solutions, P_{sn} and P_{snm}, into Eqs. (18.a) and (18.c), respectively; the Rytov solution is formed by substituting P_{sn} and P_{snm} into Eqs. (19.a) and (19.b), respectively.

The errors in the two-layer waveguide solutions are discussed in the next section. As in the previous example, the explicit error expressions will be derived for a single mode only and these simple estimates will be compared to the results from the multi-modal solutions.

3.4.2 Error Analysis

Following the analysis in section (3.2.2), we will derive the first order errors for the case of a single mode. From Eq. (40.a), the first phase term in a two-layer waveguide is

$$\phi_{11}(k_o,r,0,z,z_o) = \frac{ik_o^2 r n_1}{2h^2 P_o}\sin(\frac{\pi z}{2h})\sin(\frac{\pi z_o}{2h})\frac{H_1^{(2)}(\xi_1 r)}{\xi_1}\int_o^{z_1}\sin^2(\frac{\pi z'}{2h})\,dz' . \qquad (41)$$

Using P_o from Eq. (21), the asymptotic form of the Hankel functions (Eq. (29)), and evaluating the integral, we obtain

$$\phi_{11}(k_o,r,0,z,z_o) = \frac{ik_o^2 r n_1}{2\xi_1}\left[\frac{z_1}{h} - \frac{\sin(\frac{\pi z_1}{h})}{\pi}\right]. \qquad (42)$$

The gradient of ϕ_{11} is just

$$\nabla\phi_{11}(k_o,r,0,z,z_o) = \frac{ik_o^2 n_1}{2\xi_1}\left[\frac{z_1}{h} - \frac{\sin(\frac{\pi z_1}{h})}{\pi}\right]\hat{r}\,, \tag{43}$$

so, from Eq. (26), ϕ_{21} simply becomes

$$\phi_{21}(k_o,r,0,z,z_o) = -\frac{ik_o{}^4 r n_1^2}{8\xi_1{}^3}\left[\frac{z_1}{h} - \frac{\sin(\frac{\pi z_1}{h})}{\pi}\right]^2. \tag{44}$$

From Eqs. (42) and (44), the first order relative Born error is given by

$$\frac{P-P_1^{(B)}}{P} = O\left[-\left(\frac{ik_o{}^4 r n_1^2}{8\xi_1{}^3} + \frac{k_o{}^4 r^2 n_1^2}{8\xi_1{}^2}\right)\left[\frac{z_1}{h} - \frac{\sin(\frac{\pi z_1}{h})}{\pi}\right]^2\right] \tag{45}$$

and the first order relative Rytov error is

$$\frac{P-P_1^{(R)}}{P} = O\left[-\frac{ik_o{}^4 r n_1^2}{8\xi_1{}^3}\left[\frac{z_1}{h} - \frac{\sin(\frac{\pi z_1}{h})}{\pi}\right]^2\right]. \tag{46}$$

The behavior of the first order relative errors in range thus depends critically on the width of the layer in depth. If z_1 is small compared to h, the sine can be expanded around $z_1/h = 0$ and the errors now look like

$$\frac{P-P_1^{(B)}}{P} = O\left[-\left(\frac{ik_o{}^4 r n_1^2}{8\xi_1{}^3} + \frac{k_o{}^4 r^2 n_1^2}{8\xi_1{}^2}\right)\left[\frac{z_1}{h}\right]^6\right] \tag{47}$$

for the Born error and

$$\frac{P-P_1^{(R)}}{P} = O\left[-\frac{ik_o{}^4 r n_1^2}{8\xi_1{}^3}\left(\frac{z_1}{h}\right)^6\right]. \tag{48}$$

for the Rytov error. Therefore, if the depth of the layer is small with respect to the depth of the waveguide, the two-layer waveguide errors will be decreased from the constant velocity errors by a factor $(z_1/h)^6$. From these results, it would be expected that the errors in both solutions would decrease for any layer width less than the full extent of the waveguide.

3.4.3 Modal Decomposition of the Born and Rytov Fields

In contrast with the constant velocity example, the true and background mode functions are not identical in this case. The background eigenfunctions are sines but the true mode functions are more complicated due to the presence of the layer. Correspondingly, the expressions for the mode coefficients are more difficult to derive and interpret.

From Eq. (E.8), the Born coefficient for the single mode in the two-layer waveguide is

$$C_{1B} = 2\tilde{A}\sin(\frac{\pi z_o}{2h})\left[1 + \frac{ik_o^2 r n_1}{2h\xi_1}\left(\frac{z_1}{h} - \frac{\sin(\frac{\pi z_1}{h})}{\pi}\right)\right] \tag{49}$$

and from Eq. (E.10), the Rytov is

$$C_{1R} = 2\,\tilde{A}\sin(\frac{\pi z_o}{2h})\exp\left[\frac{ik_o^2 rn_1}{2h\xi_1}\left(\frac{z_1}{h} - \frac{\sin(\frac{\pi z_1}{h})}{\pi}\right)\right] \tag{50}$$

where $\tilde{A}$ is given in Eq. (E.9). As in the constant velocity case, the Rytov mode coefficient reduces to the Born if

$$\left|\frac{ik_o^2 rn_1}{2h\xi_1}\left[\frac{z_1}{h} - \frac{\sin(\frac{\pi z_1}{h})}{\pi}\right]\right| \ll 1$$

and we truncate the series to first order.

Superficially, the modal decompositions seem to suggest the same type of behavior as the first order errors. However, as will be seen in the next section, the quantity $\tilde{A}$ plays a significant role in determining the validity of the solutions.

3.5 Two-Layer Waveguide Examples

In this section, we discuss two velocity models; the first has a 100 m layer and the second a 400 m layer. The parameters for the first model are given in Table 2.

The true and background profiles are illustrated in Figure 20 and the transmission loss curves in Figure 21. Again, the guess overlays the true profile almost exactly due to the smallness of the perturbation and also its minimal extent.

We will first qualitatively predict the behavior of the Born and Rytov solutions by studying the ratio $|P_s/P_o|$ vs. range in Figure 22. Both of the

Table 2. Input Parameters: Test Case 2

INPUT PARAMETERS: TEST CASE 2		
Range		1.-50. km
Source Depth		500. m
Receiver Depth		500. m
Source Frequency		25. Hz
	Depth (m)	Sound Speed (m/s)
True profile	0.	1500.
	100.	1500.
	100.	1501.
	1500.	1501.
Guess profile	0.	1501.
	1500.	1501.
Maximum Perturbation		1. m/s
Perturbation Width		100. m

ratios are less than 1/4 (except at the spikes) and they match in amplitude except at the spikes which occur at the nulls in the amplitude of the incident field. This is a case where we are in the range of validity of both solutions; the ratio of the scattered to the incident field is small. Therefore, the solutions are expected to generate similar results.

The Born and the true solution are illustrated in Figure 23 and the Rytov and the true solution are illustrated in Figure 24. As expected, the approximate

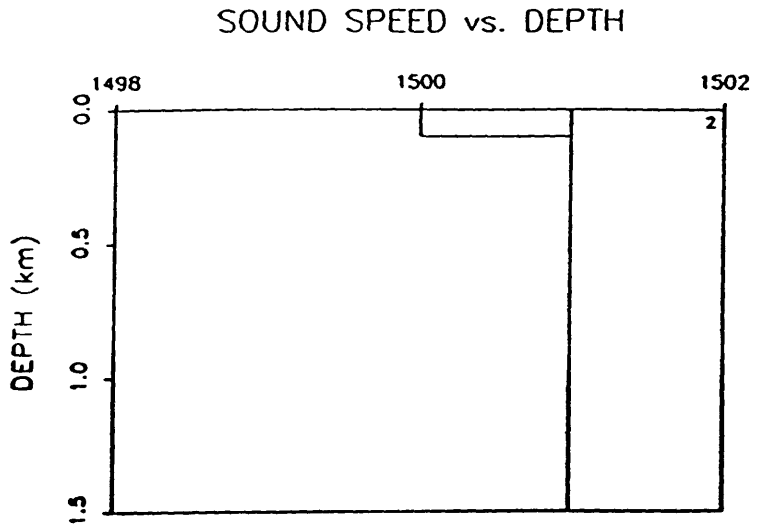

Figure 20. The true and background sound speed profiles used in test case 2. The background profile is constant over the entire waveguide at 1501 m/s. The true profile has a 100 meter layer in which the sound speed is 1500 m/s. Below the layer, the true and background sound speeds are identical.

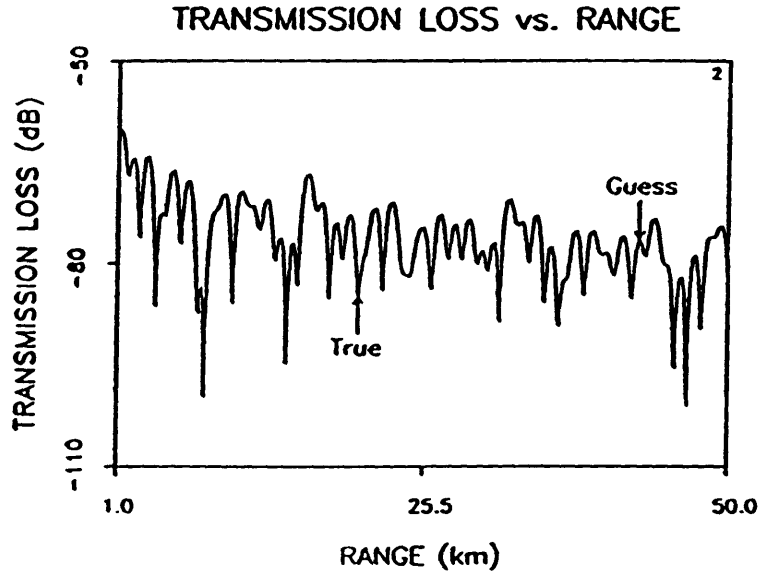

Figure 21. The true and background transmission loss curves for test case 2. Because the perturbation is small (1 m/s) and extends only 100 meters in depth, the two curves are nearly identical.

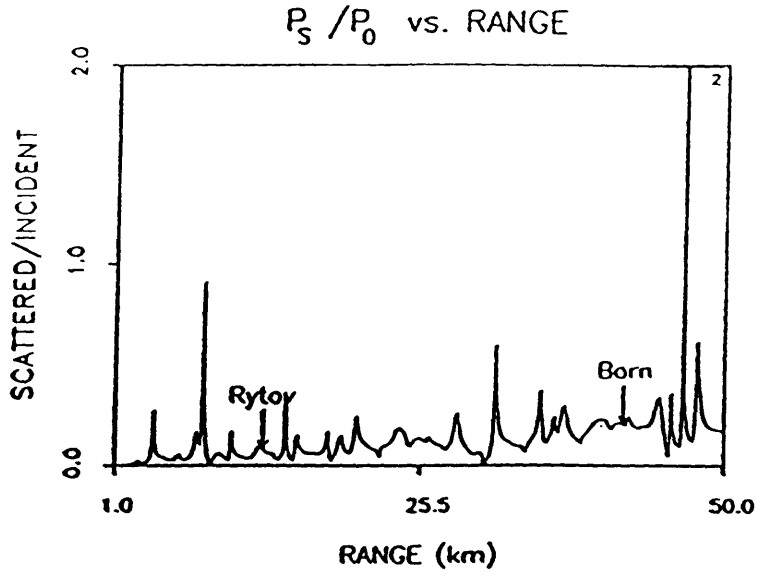

Figure 22. **Ratio of the scattered field to the incident field for the Born and Rytov solutions in the two-layer waveguide of test case 2. Because the trend of the ratio is less than 1/4 over the range of propagation, both solutions are expected to yield accurate results.**

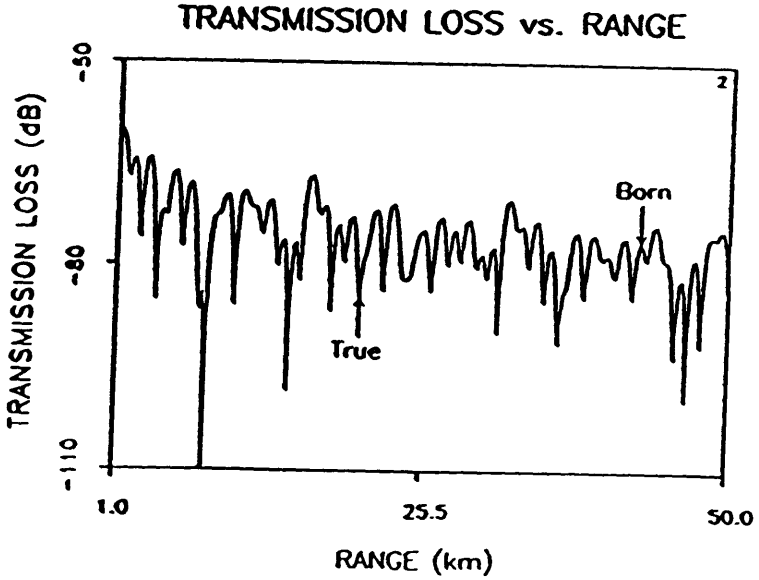

Figure 23. **The true and Born transmission loss curves for test case 2. The Born solution matches the true except at the nulls in the field.**

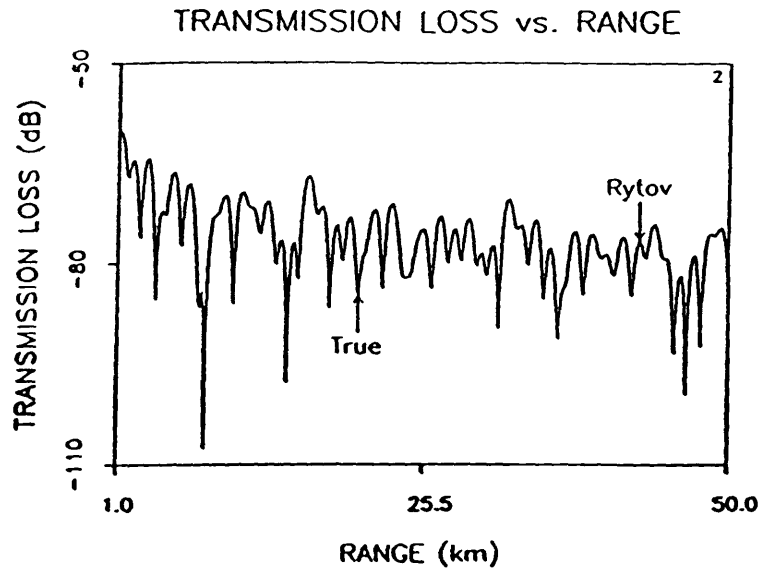

Figure 24. The true and Rytov transmission loss curves for test case 2. The Rytov solution matches the true except at the nulls in the field.

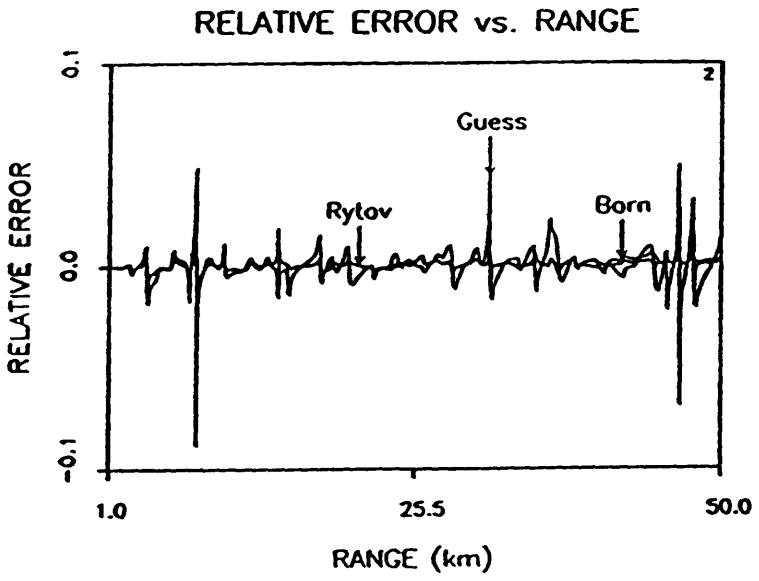

Figure 25. Relative error in the background, Born and Rytov transmission loss curves for test case 2. The error in the the solutions is always less than 10%.

solutions overlay the true solution, except at the nulls, as is illustrated in Figure 25, by the relative errors.

At this point, we could further confirm the above results by proving the errors to be minimal in the modal decomposition, but instead we will just conclude that for a 1 m/s perturbation extending over 7% of the waveguide the Born and Rytov are valid approximations over a range of 1 to 50 km.

The next case discussed is that of a layer extending over 28% (400 m) of the waveguide. The input parameters for this example are given in Table 3.

The true and background profiles are illustrated in Figure 26 and the transmission loss curves are illustrated in Figure 27. There is a visible difference in the true and guess curves. From test case 1, we know that when the perturbation is 1 m/s over the full waveguide, the transmission loss curves are basically identical. The reason for the variation in test case 3 is due to the change in the eigenfunctions. As the width of the layer increases to a certain depth, the difference in the true and background mode functions increases correspondingly. As the layer width extends to the full waveguide, the mode shapes return to those found in a constant velocity environment.

Figure 28 demonstrates the change in the first mode when the layer width is increased in 200 m increments. The first curve is the mode shape in a constant velocity waveguide; the second curve is the mode shape when a 200 m layer is

Table 3. Input Parameters: Test Case 3

INPUT PARAMETERS: TEST CASE 3		
Range		1.-50. km
Source Depth		500. m
Receiver Depth		500. m
Source Frequency		25. Hz
	Depth (m)	Sound Speed (m/s)
True profile	0.	1500.
	400.	1500.
	400.	1501.
	1500.	1501.
Guess profile	0.	1501.
	1500.	1501.
Maximum Perturbation		1. m/s
Perturbation Width		400. m

present, the third curve is the mode shape when a 400 m layer is present and so on.

To estimate the percentage change in the mode functions, we look at the change in the mode coefficient over the waveguide as the layer width is systematically increased. From Figure 29, we can estimate that a 400 meter layer with a 1 m/s change in the sound speed, results in approximately a 14% change in the mode coefficient as compared to the constant velocity case. It is evident, then,

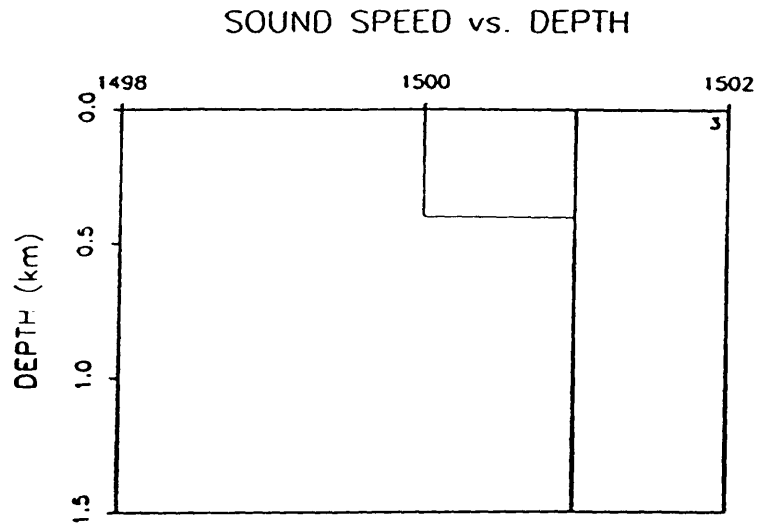

Figure 26. The true and background sound speed profiles used in test case 3. The background profile is constant over the entire waveguide at 1501 m/s. The true profile has a 400 meter layer in which the sound speed is 1500 m/s. Below the layer, the true and background sound speeds are identical.

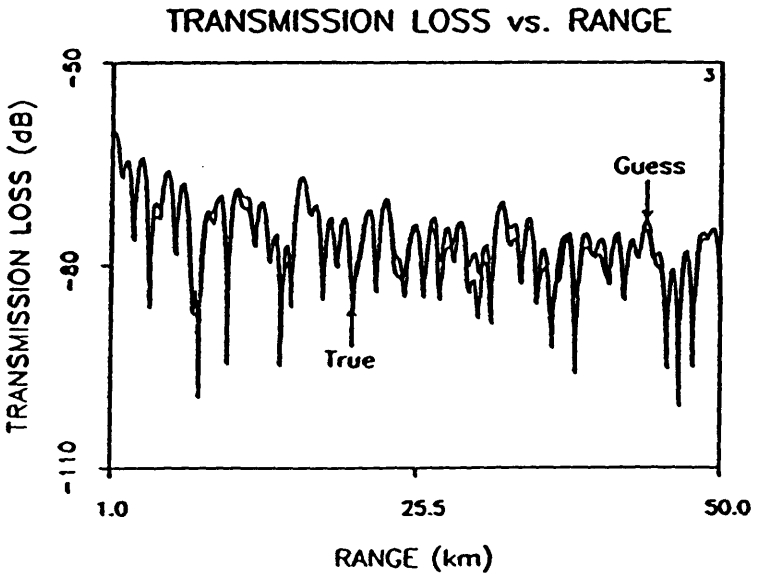

Figure 27. The true and background transmission loss curves for test case 3. Although the perturbation is small (1 m/s), it extends over 28% of the waveguide; therefore the guess transmission loss differs from the true.

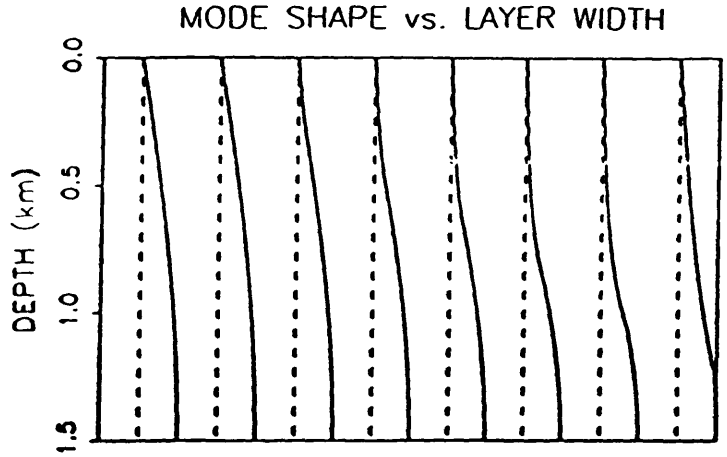

Figure 28. **Illustrated is the variation of the lowest order mode as a function of layer depth. The curve on the far left represents the mode shape in a constant velocity waveguide and the second curve from the left is the mode shape when a 200 m layer is present, etc. The curve on the far right is the shape of the lowest order mode when a 1.4 km layer is present. When the layer extends to 1.5 km, the shape returns to that in a constant velocity waveguide.**

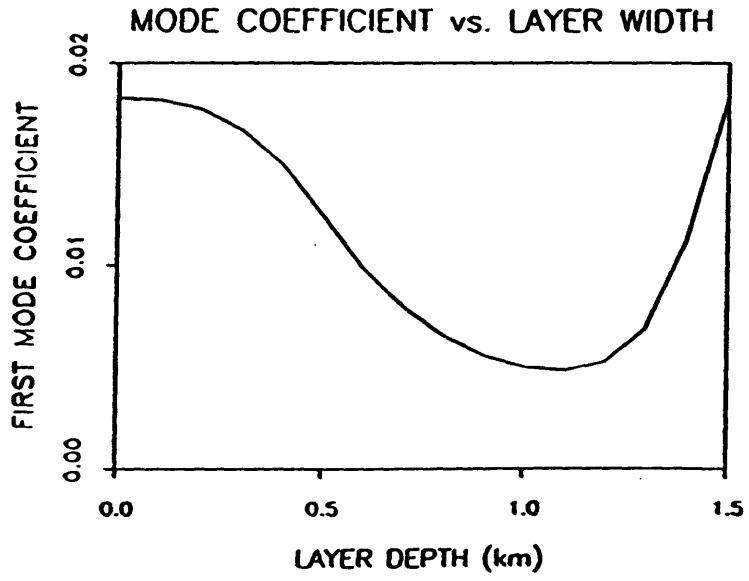

Figure 29. The change in the mode coefficient for the lowest-order mode as a function of the layer width. In a constant velocity waveguide, the numerical value is ~0.018. The value of the coefficient decreases to ~.005 at 1 km, and at 1.5 km returns to the original value of 0.018.

that a small change in the sound speed over 28% of the waveguide causes a large change in the value of the eigenfunctions and a corresponding change in the true and background transmission loss curves.

To predict the behavior of the Born and Rytov solutions, we again study the ratio of the scattered to the incident field for both approximations. From Figure 30 and a closeup in Figure 31, we see that the ratio in both cases has exceeded 1/4 by a range of approximately 13 km. Therefore, the Born solution is expected to grow for ranges greater than 13 km. The behavior of the Rytov solution is difficult to predict. Although the Rytov ratio also exceeds 1/4, we saw in the constant velocity case that a large ratio did not affect the validity of the Rytov solution.

The Born and true transmission loss plots are illustrated in Figure 32 and the Rytov and true in Figure 33. As expected, there is a slight growth in the Born solution. The Rytov solution is somewhat more accurate (see the relative error versus range in Figure 34), but again does not match the true solution; in addition, a spike in the solution appears at about 5 km in the same location as one of the spikes in the $|P_s/P_o|$ of Figure 30.

We now see the effect that a 14% change in the true and background eigenfunctions has on the accuracy of the Born and Rytov solutions. We also see the failure of the error predictions to account for this type of change. Only the factor $\sqrt{\tilde{A}}$ in the modal decompositions gives an indication that the solutions will

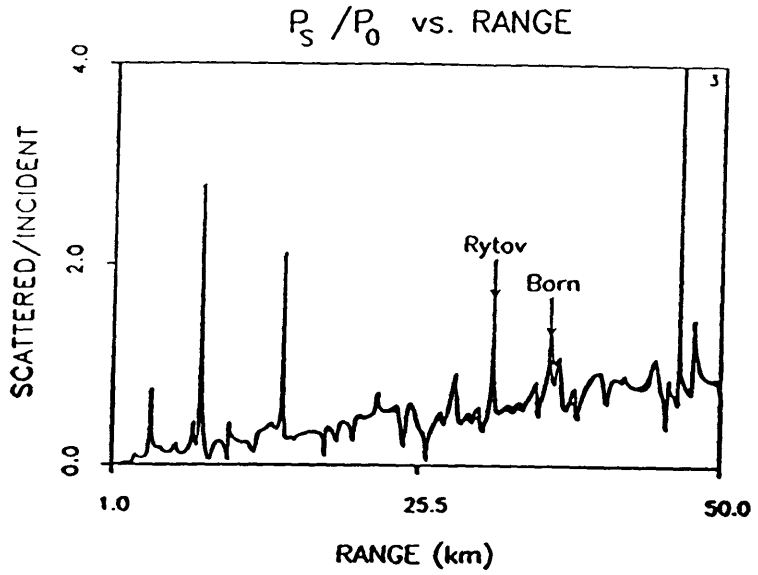

Figure 30. Ratio of the scattered field to the incident field for the Born and Rytov solutions for the two-layer waveguide of test case 3. Because large localized spikes are present in the ratios, the solutions are also expected to have large local errors.

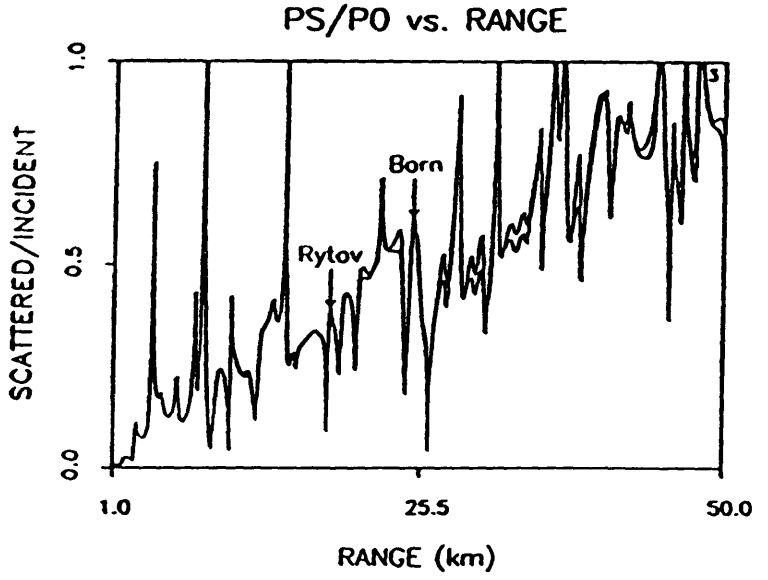

Figure 31. Expanded version of Figure 30. Note the trend of the ratio of both coefficients exceeds 1/4 by ~13 km; as a result a growth in the Born solution is predicted.

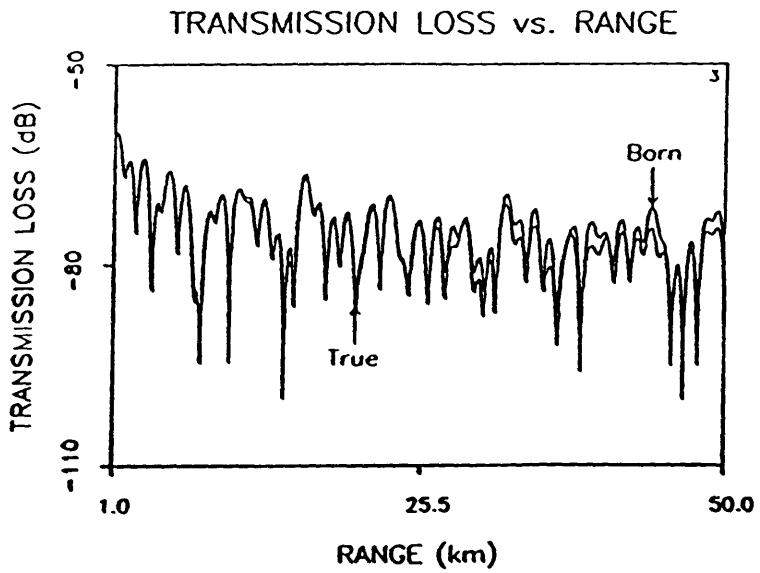

Figure 32. The true and Born transmission loss curves for test case 3. Although the Born reconstructs the general shape of the curve, the growth of the solution is apparent for ranges greater than ~13 km.

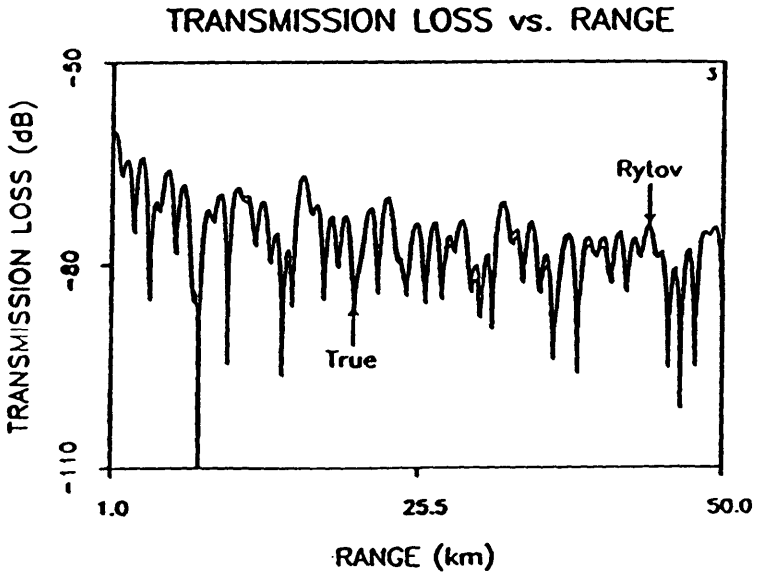

Figure 33. The true and Rytov transmission loss curves for test case 3. Although the Rytov approximates the true solution better than the Born, amplitude errors are apparent in both the nulls and peaks in the field.

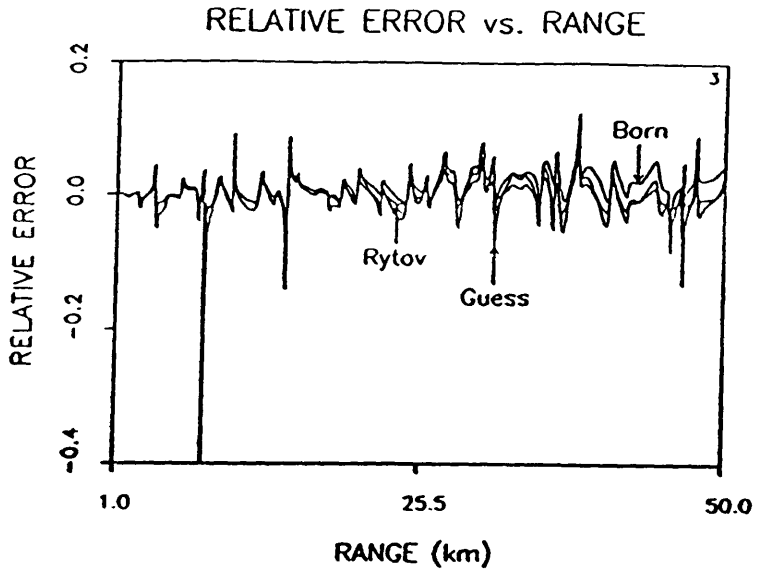

Figure 34. **Relative error in the background, Born and Rytov transmission loss curves for test case 3. Although the Rytov has the least error, neither of the perturbative solutions were able to duplicate the true transmission loss curve.**

become invalid for layer widths less than the full waveguide.

Although difficult to analyze quantitatively, the significance of $\sqrt{\tilde{A}}$ can be explained in terms of the constant velocity versus the two-layer solution. From Eq. (21), we know the true and background solutions in a constant velocity waveguide are constructed from an identical set of eigenfunctions; only the eigenvalues differ. In the two-layer waveguide, the eigenfunctions of the true solution vary (see Eq. (38)) depending on the receiver location in the waveguide with respect to the layer. The former case has a simple normalization factor of $\sqrt{(2/h)}$, while from Eq. (39) the latter has the expression, $\sqrt{A}$. From the modal

decomposition of the Born and Rytov approximations (Appendix E), the term $\sqrt{\tilde{A}}$ occurs which contains, in addition to the factor $\sqrt{A}$, other terms resulting from the projection of the coefficients over a depth 0 to z_1 where the constant velocity eigenfunctions are not orthogonal. Therefore, for the Born and Rytov solutions to be valid representations of the true field, the term $\sqrt{\tilde{A}}$ must give the right mode shapes for the two-layer waveguide. This is impossible because $\sqrt{\tilde{A}}$ is constant for a given layer depth and there still remains only a single set of eigenfunctions predicting the true behavior over the entire waveguide. As a result, the Born and Rytov solutions are unable to approximate the true solution if the true and guess eigenfunctions differ by more than about 7%.

The results of this section will now be used to predict the behavior, in the next chapter, of the perturbation expansions in a depth-dependent environment.

4. DEPTH-DEPENDENT BACKGROUND TEST CASES

4.1 Introduction

Although a constant background solution provides useful error estimates, it is not viable zeroth order solution in the deep ocean. For this reason, we now turn to the distorted-wave perturbative approximations in which the background profile depends on depth. Several depth-dependent velocity profiles are studied and the results compared to those predicted from the constant velocity analysis. In all cases, the trend of the sound speed profile is assumed to be known exactly; we look at the behavior of the DWB and DWR solutions when a perturbation is placed upon the background solution. Unlike the previous chapter, the results in this chapter cannot be derived explicitly even for a single mode. The reason is that the eigenfunctions are known only numerically. The DWB and DWR representations of the total field are obtained from Eqs. (7) and (10), respectively.

The background profile in the first two examples is the weakly refractive NORDA 2A test case (NORDA Parabolic Workshop 1984). Two different size perturbations (referred to as test cases 4 and 5) are placed on this profile and we study the ability of the DW approximations to construct the true solution.

In the second set of examples, the profile is strongly refractive. Two different test cases (referred to as test cases 6 and 7) are presented. The perturbation is the

same is both cases but the source position and, therefore, the illumination in the waveguide is varied.

4.2 NORDA 2A Examples

The parameters used in test case 4 are given in Table 4.

Table 4. Input Parameters: Test Case 4

INPUT PARAMETERS: TEST CASE 4		
Range		1.-50. km
Source Depth		500. m
Receiver Depth		500. m
Source Frequency		25. Hz
	Depth (m)	Sound Speed (m/s)
True profile	0.	1500.0
	300.	1506.0
	400.	1507.5
	500.	1510.0
	1000.	1520.0
	1500.	1563.0
Guess profile	0.	1500.0
	1000.	1520.0
	1500.	1563.0
Maximum Perturbation		0.5 m/s
Perturbation Width		200.0 m

The NORDA 2A bilinear profile, illustrated in Figure 35, is the background profile in this example. The true profile is constructed by placing a small perturbation of limited extent on top of the guess. The profile perturbation is illustrated in Figure 36; over the rest of the profile, the true and background sound speed values are identical.

The transmission loss curves for the perturbed and unperturbed profiles are illustrated in Figure 37. Even though the profile perturbation is only .5 m/s and only extends over 13% of the waveguide, there are visible differences between the two curves. However, from the results of section 3.5, we expect the DWB and DWR to give a good approximation to the true solution.

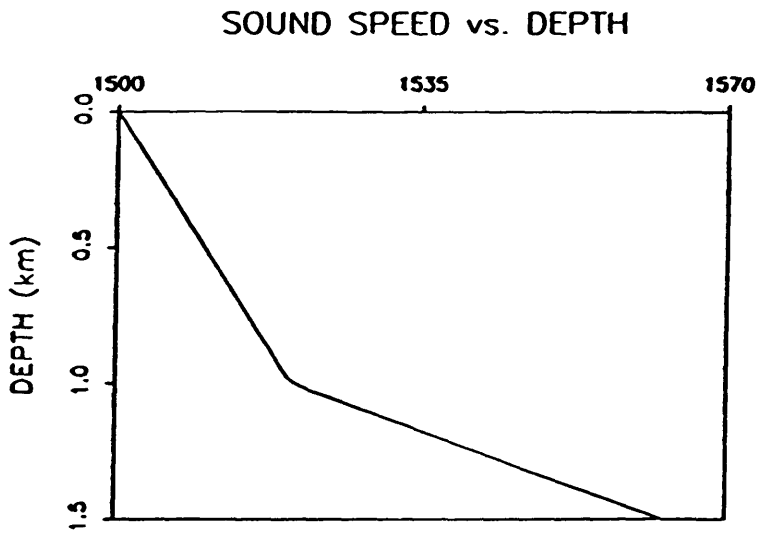

Figure 35. NORDA 2A bilinear background profile used in test cases 4 and 5.

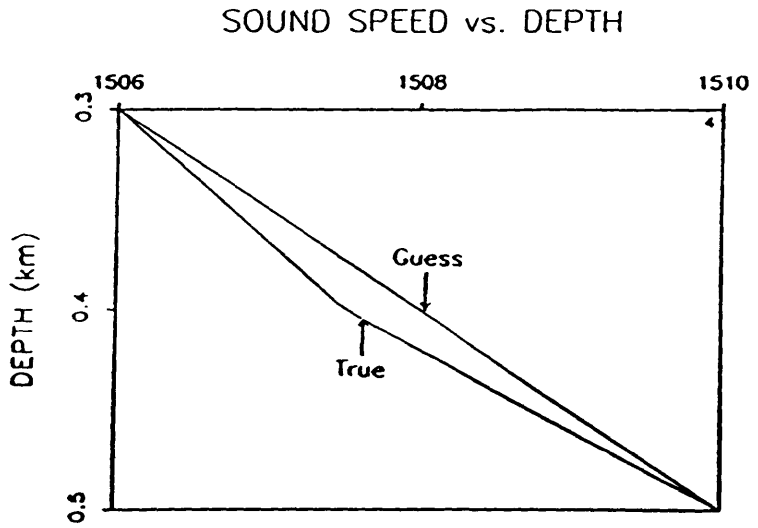

Figure 36. The profile perturbation used in test case 4. The perturbation extends from 300 to 500 m in depth and the maximum variation from the background is .5 m/s. In the remainder of the waveguide, the true sound speed matches the background.

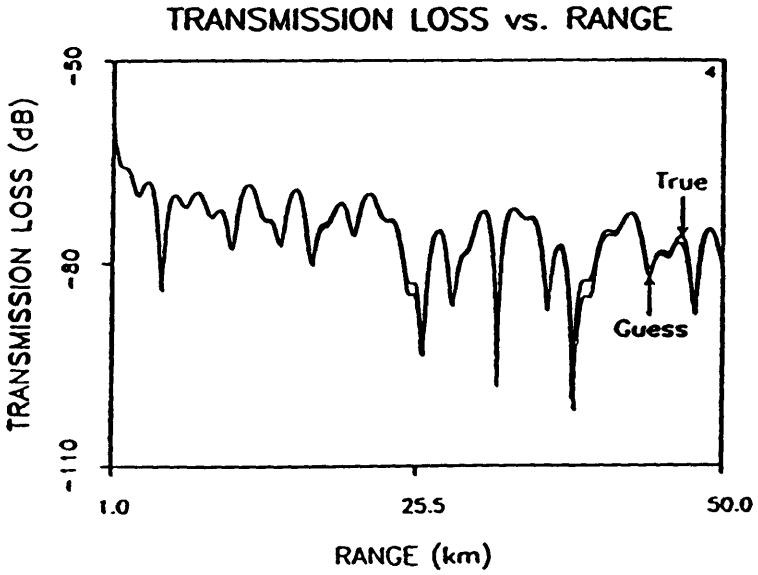

Figure 37. True and background transmission loss curves for test case 4. Although the maximum difference in sound speed is only 0.5 m/s, the perturbation extent is ~13% of the waveguide; therefore the curves differ as we propagate in range.

The ratios of the scattered to the incident field amplitudes as a function of range are illustrated in Figure 38. In order to clearly illustrate the trend of the ratios, the same curves are shown in Figure 39 with an expanded vertical scale. From Figure 38, we would predict the possibility of a large local error in the DWR solution due to the spike near 40 km. Figure 39, on the other hand, gives an indication of the global behavior of the solutions, particularly the DWB. Because the trend of the ratio does not exceed 1/4, we would expect to obtain an accurate solution from the DWB as well as the DWR. In fact, for this test case, the expansions are approximately equal for ranges less than 50 km.

Figures 40 and 41 illustrate the transmission loss results from the DWB and DWR solutions. The DWB exhibits minimal growth for ranges greater than about 40 km, while the DWR solution contains a spike at the null at the same range. But as illustrated by the relative errors in Figure 42, both solutions give a good approximation to the true transmission loss.

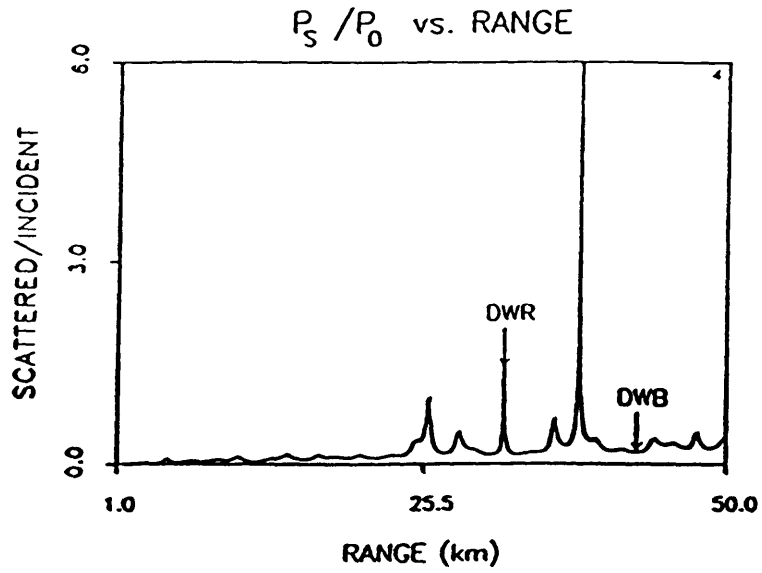

Figure 38. Ratio of the scattered field to the incident field for the DWB and DWR solutions for test case 4. The spike at ~40 km suggests the possibility of a local error in the solutions.

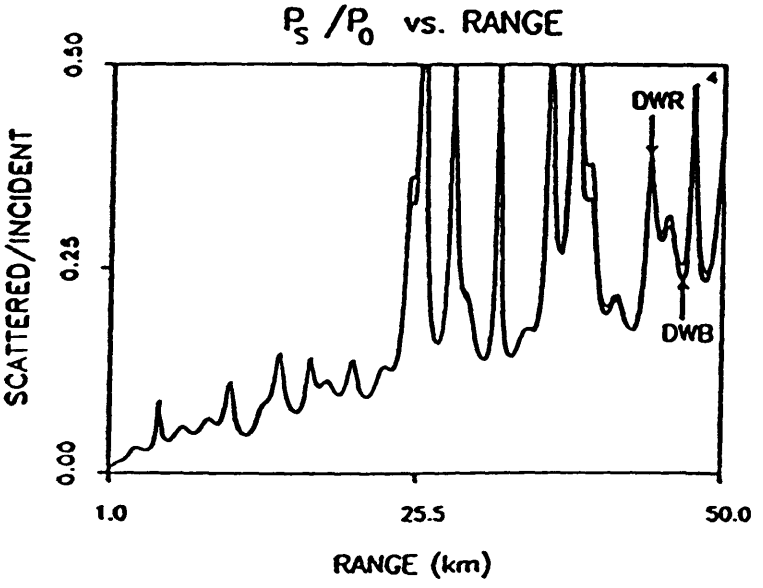

Figure 39. Expanded version of Figure 38. The trend of the ratios is less than 1/4 and the DWB and DWR are predicted to give accurate results.

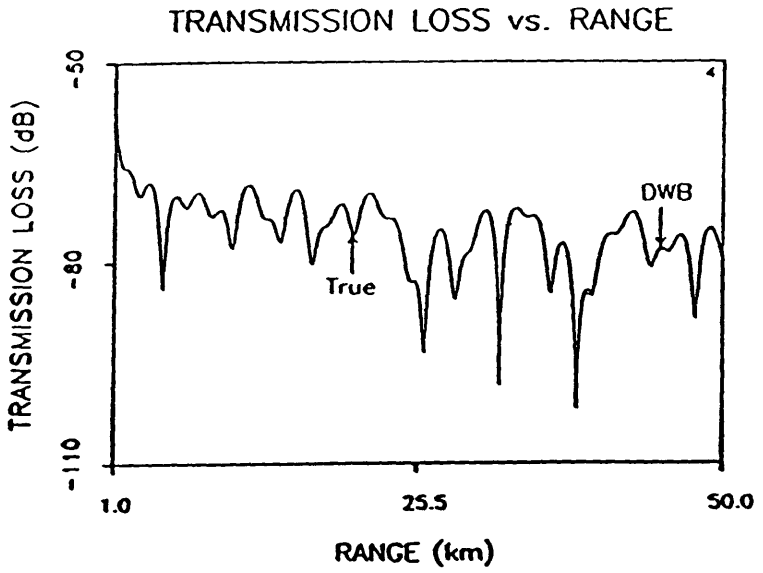

Figure 40. True and DWB transmission loss curves for test case 4. As predicted, the DWB is a good approximation to the true solution.

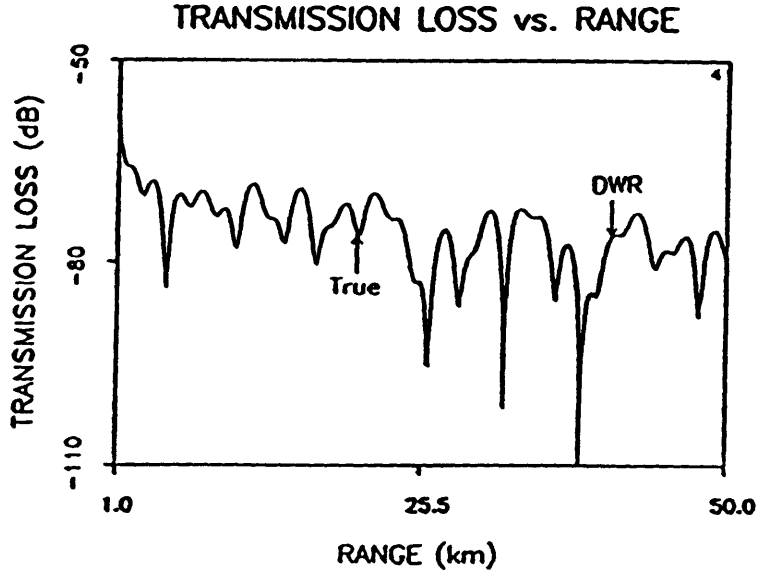

Figure 41. True and DWR transmission loss curves for test case 4. As predicted, the DWR is a good approximation to the true solution except at the null near 40 km.

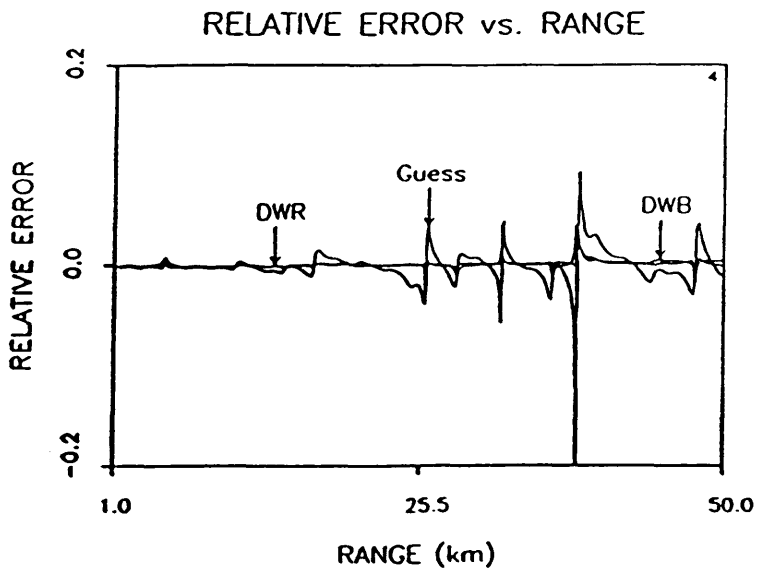

Figure 42. Relative error in the background, Born and Rytov transmission loss curves for test case 4.

In the next example, the size of the perturbation is increased to 1 m/s but the extent of the perturbation remains the same. The input parameters for test case 5 are given in Table 5. The background solution is again the NORDA 2A profile.

The profile perturbation is illustrated in Figure 43. The transmission loss curves for the true and background profiles are illustrated in Figure 44. As expected, the difference in the true and guess curves is greater than in the previous example. The guess and the true solutions differ both in magnitude and in the position of the nulls.

The scattered to incident field ratios are illustrated in Figure 45 and a closeup

Table 5. Input Parameters: Test Case 5

INPUT PARAMETERS: TEST CASE 5		
Range		1.-50. km
Source Depth		500. m
Receiver Depth		500. m
Source Frequency		25. Hz
	Depth (m)	Sound Speed (m/s)
True profile	0.	1500.
	300.	1506.
	400.	1507.
	500.	1510.
	1000.	1520.
	1500.	1563.
Guess profile	0.	1500.
	1000.	1520.
	1500.	1563.
Maximum Perturbation		1. m/s
Perturbation Width		200. m

of the same curves is illustrated in Figure 46. In this case, the magnitude of the spike (although not indicated by the plot scale) in Figure 45 near 40 km is over twice that in the previous example and we would expect a larger local error. From Figure 46, we would expect the DWB solution to fail at ranges greater than 25 km when the ratio exceeds 1/4. Again, the transmission loss curves illustrated in

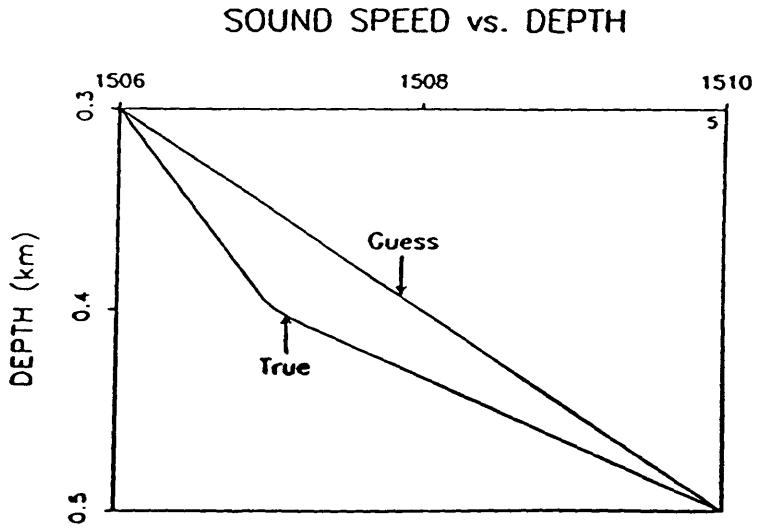

Figure 43. Profile perturbation for test case 5. The maximum variation from the background is now 1 m/s and the extent is ~13% of the waveguide.

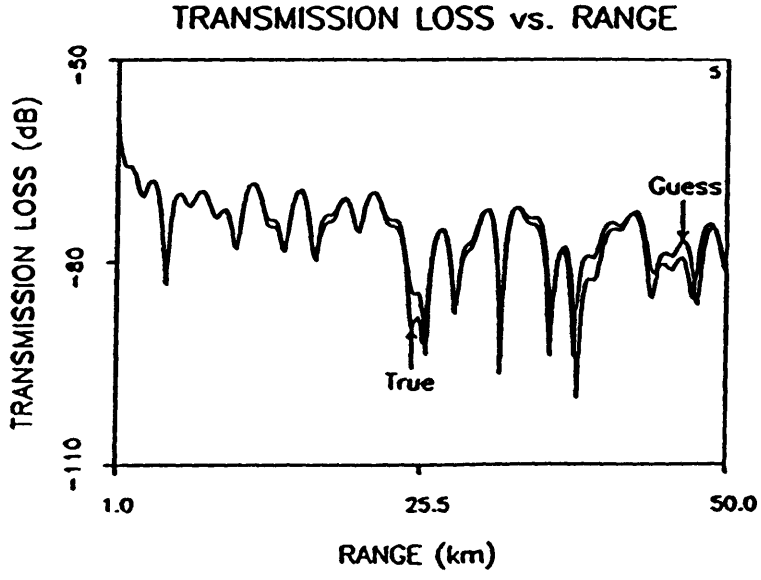

Figure 44. True and background transmission loss curves for test case 5. Note the difference in the two curves as compared to Figure 37.

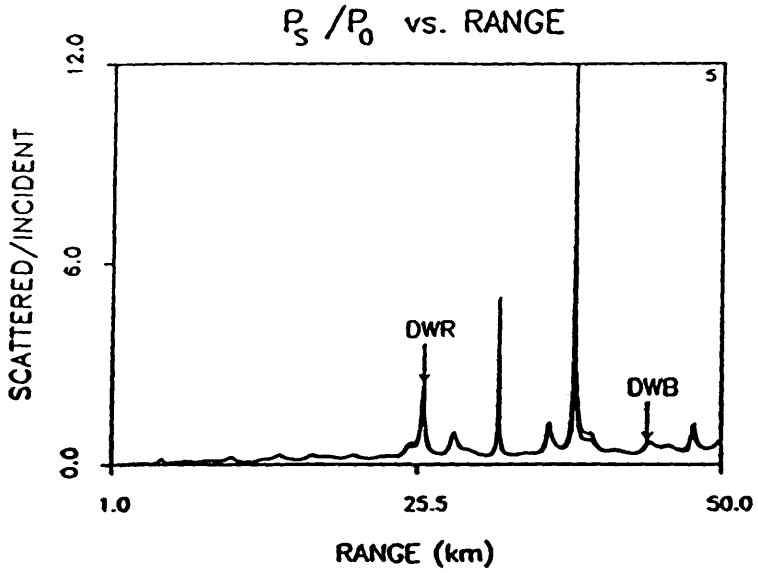

Figure 45. Ratio of the scattered field to the incident field for the DWB and DWR solutions for test case 5. As in Figure 38, the spike at ~40 km suggests the possibility of a local error the solutions.

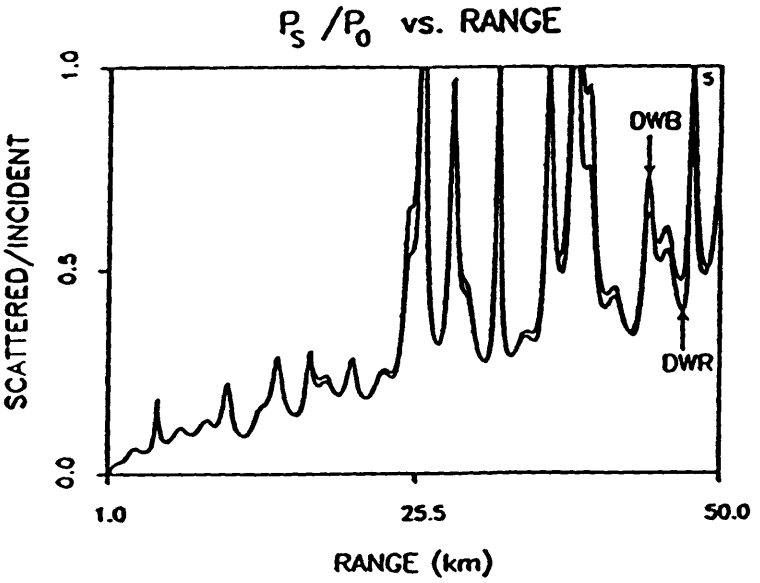

Figure 46. Expanded version of Figure 45. The DWB solution is expected to be in error past 25 km when the ratio exceeds 1/4.

Figures 47 and 48 verify the qualitative predictions. Although, the DWB solution has shifted from the guess to indicate correctly the position of the nulls, the growth in the solution becomes evident past 25 km. The DWR, on the other hand, contains a spike at the null near 40 km and, in addition, incorrectly positions the nulls. The amplitude behavior is, however, closer to the true solution than the DWB. The relative error in the transmission loss of the guess, DWB and DWR solutions is illustrated in Figure 49.

This is exactly the behavior predicted from the two-layer case in section 3.5. As the change in the true and background mode functions increases, the ability of the DWB and DWR to construct the true solution decreases.

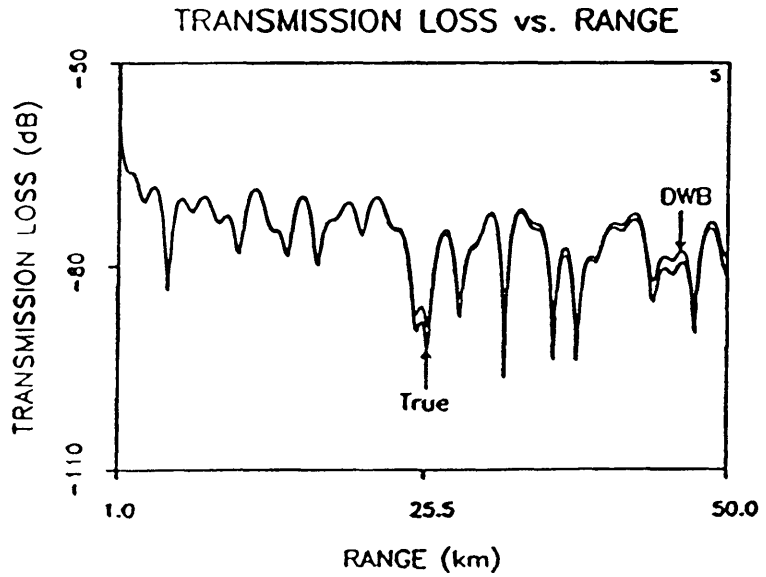

Figure 47. True and DWB transmission loss curves for test case 5. Although the shape of the curve is correct, the growth in the DWB solution for ranges greater than 25 km is evident.

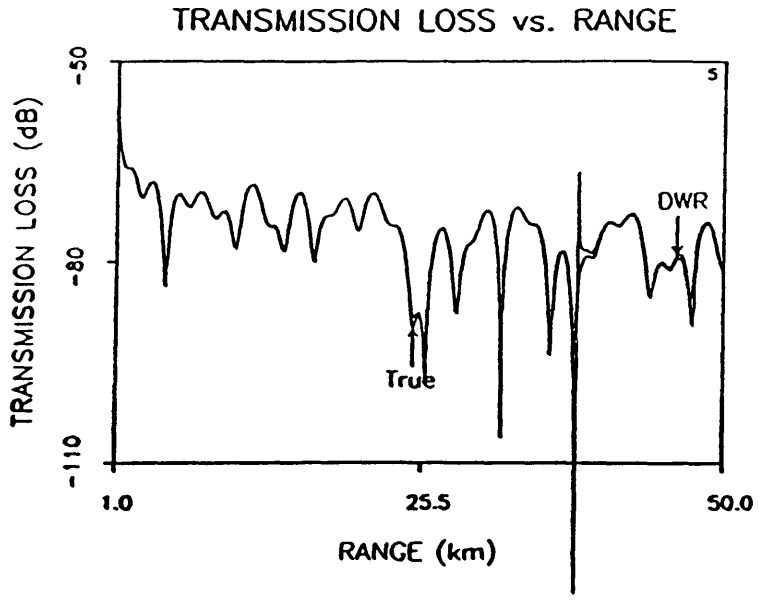

Figure 48. True and DWR transmission loss curves for test case 5. The error in the DWR solution near ~40 km has increased (compare Figure 41) and there are errors in the amplitude. In addition, the DWR fails to correctly position the nulls of the solution.

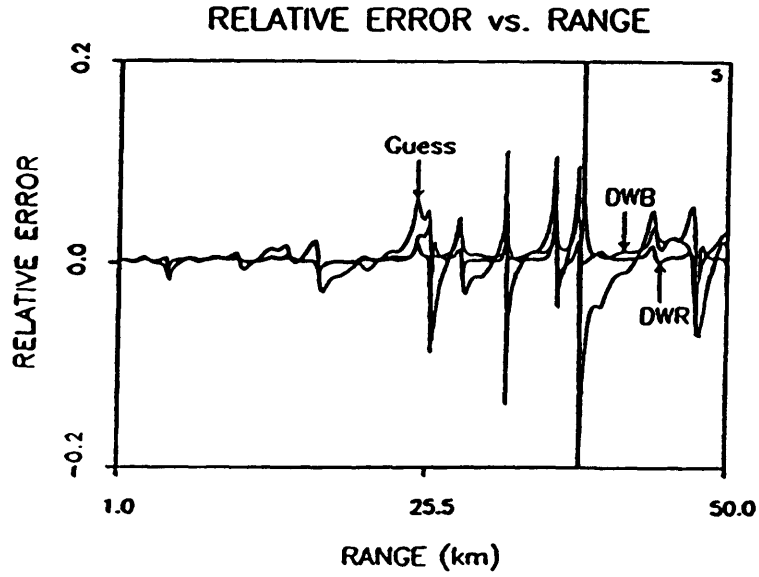

Figure 49. Relative error in the background, DWB and DWR transmission loss curves for test case 5. The vertical scale has been expanded to differentiate the errors.

We now turn to some deep ocean examples in which the sound energy propagates mainly through refraction.

4.3 SOFAR Channel Examples

As discussed in Chapter 1, the velocity structure of the SOFAR channel is characterized by a sound speed minimum (known as the channel axis) at about 1 km with the sound speed increasing both above and below the axis. In this section, we study the behavior of the DWB and DWR solutions when the perturbations are placed about a bilinear background sound speed profile. In particular, we investigate the effect of varying the source position with respect to the channel axis.

The parameters for the first example in this section, test case 6, are given in Table 6. The source is placed at 500 m, while the channel axis is at 1 km. Because the profile is strongly refractive, the entire waveguide is not insonified. Instead the energy in the waveguide travels in a relatively narrow beam.

The background profile is illustrated in Figure 50 and the perturbation about the background is illustrated in Figure 51. The true and background transmissions loss curves, illustrated in Figure 52, give an indication of the insonified and shadow zones in the waveguide. Near the source the energy is a maximum, but as we move out in range to approximately 13 km there is a broad low energy region

Table 6. Input Parameters: Test Case 6

INPUT PARAMETERS: TEST CASE 6		
Range		1.-50. km
Source Depth		500. m
Receiver Depth		500. m
Source Frequency		25. Hz
	Depth (m)	Sound Speed (m/s)
True profile	0.	1520.
	700.	1478.
	800.	1473.
	900.	1466.
	1000.	1460.
	4000.	1525.
Guess profile	0.	1520.
	1000.	1460.
	4000.	1525.
Maximum Perturbation		1. m/s
Perturbation Width		200. m

which extends to approximately 30 km. Past 30 km, the region around the receiver depth is again illuminated.

The ratios of the scattered to incident field, illustrated in Figure 53 with an closeup in Figure 54, indicate that the maximum error is expected to occur in the shadow zone; in particular, in the transition from low to high energy near a range

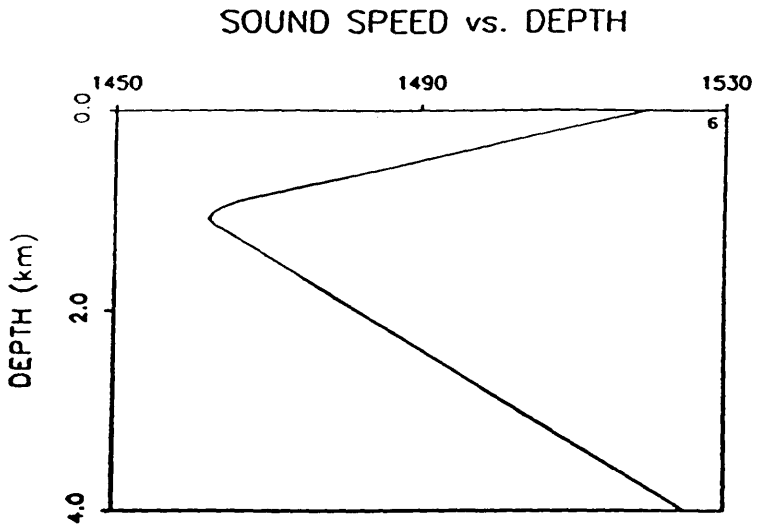

Figure 50. Background profile used in test cases 6 and 7.

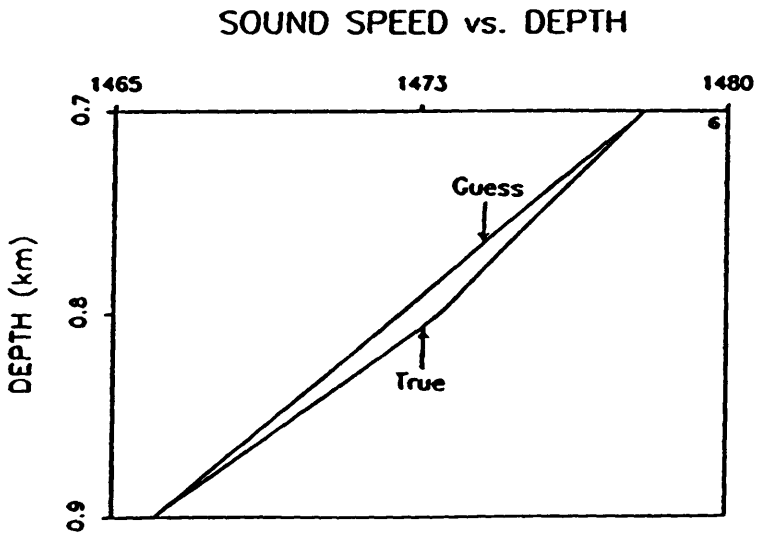

Figure 51. Profile perturbation for test cases 6 and 7. The maximum variation from the background is 1 m/s and the extent is ~5% of the waveguide.

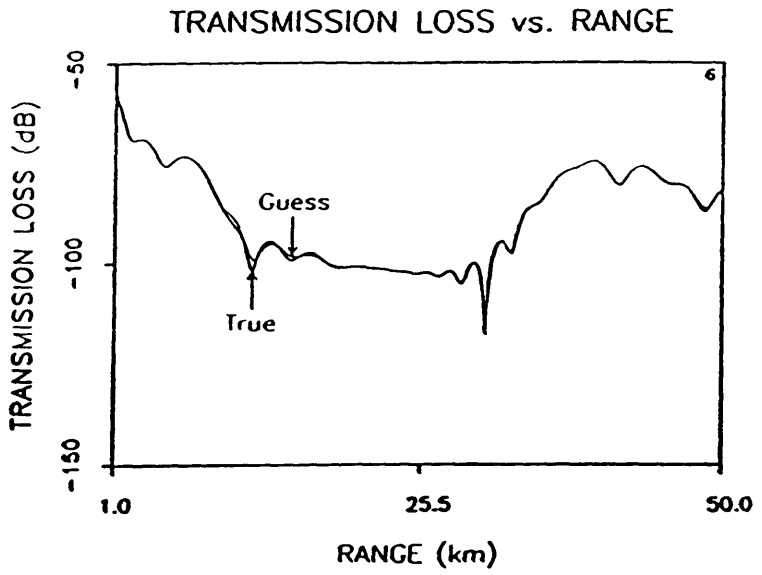

Figure 52. True and background transmission loss curves for test case 6. Note the broad region of low intensity.

of 30 km. However, except for isolated spikes the ratio is always less than 1/4 and, therefore the perturbative solutions are expected to yield accurate results.

The DWB and DWR transmission loss curves are illustrated in Figures 55 and 56. The vertical scales on both plots have been expanded to include the spike occurring near 29 km. The DWB and DWR solutions are nearly identical as predicted by the small $|P_s/P_o|$ ratios. Both solutions match the true solution in the regions of high intensity, but fail to give the correct values in the shadow zone and in fact exhibit a greater error than the guess near the deep null. A plot of the relative errors (Figure 57) in the two solutions substantiates this conclusion. Although qualitative predictions suggest that both solutions are within their range

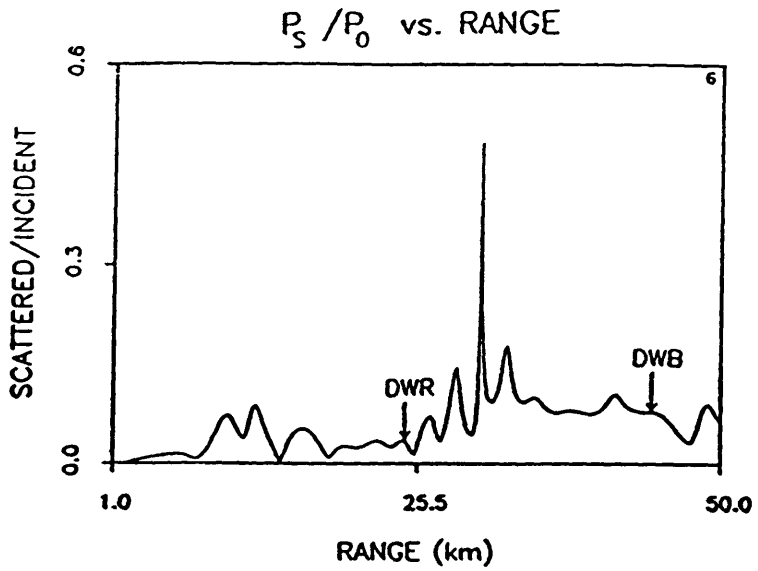

Figure 53. Ratio of the scattered field to the incident field for the DWB and DWR solutions for test case 6.

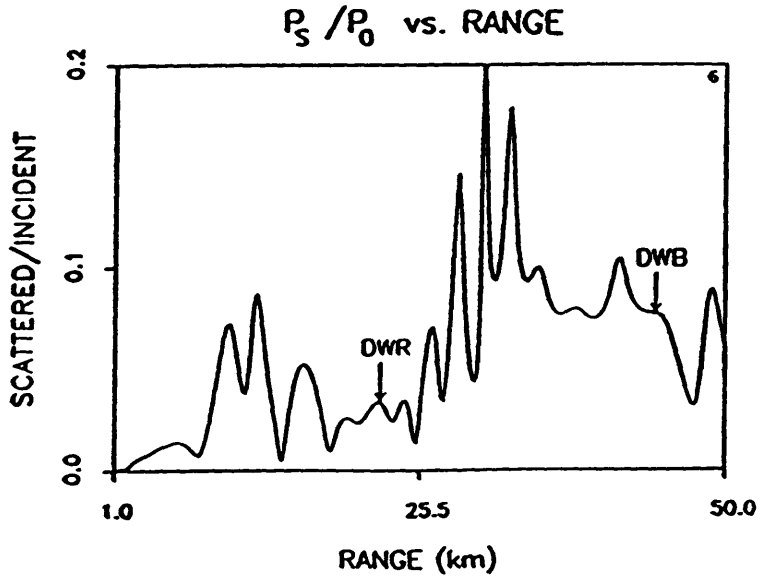

Figure 54. Expanded version of Figure 53. Note the maximum error occurs in the region of low intensity.

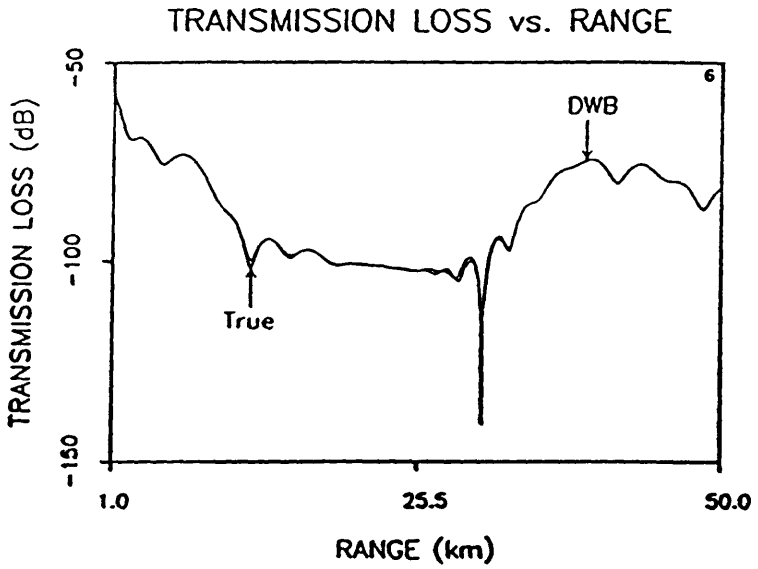

Figure 55. True and DWB transmission loss curves for test case 6. The vertical scale has been expanded to include the spike near 29 km.

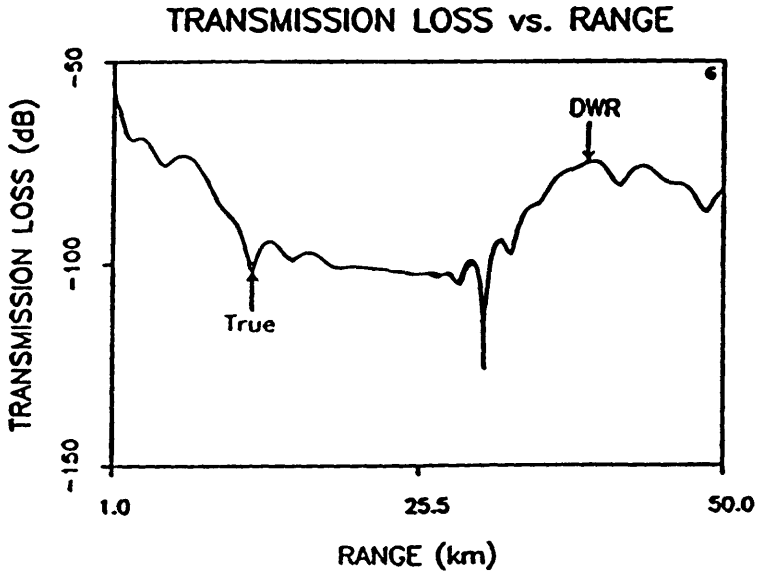

Figure 56. True and DWR transmission loss curves for test case 6. The vertical scale has been expanded to include the spike near 29 km.

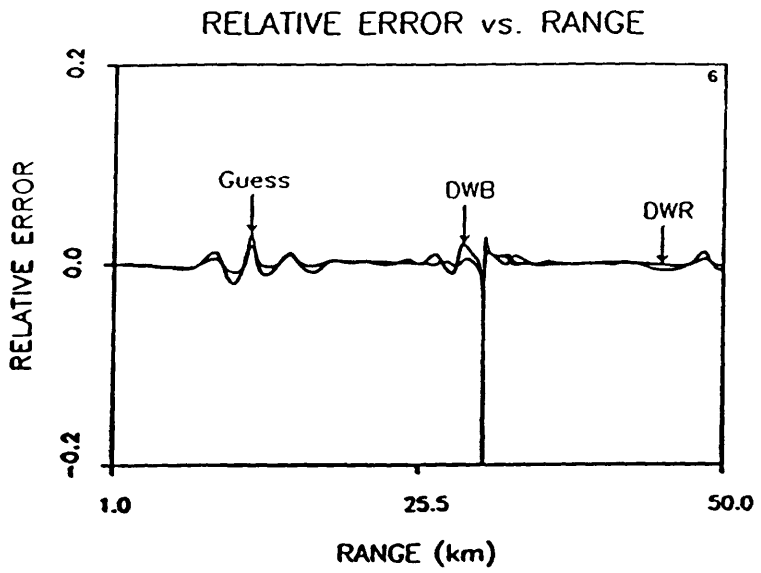

Figure 57. Relative error in the background, DWB and DWR transmission loss curves for test case 6.

of validity, this test case indicates that the DWB and DWR are invalid over broad regions of low intensity as well as at the isolated nulls in the field.

In the last example, the parameters are the same as in test case 6 except the source and receiver are placed on the channel axis at 1 km. The true and guess transmission loss plots are illustrated in Figure 58. The shadow zone has disappeared as expected and the background solution nearly overlays the true.

As illustrated in Figure 59, the DWB and DWR scattered to incident field ratios are nearly identical. A closeup of the plots in Figure 60 demonstrates the ratio of the trends to be less than 1/4. Although the spike at approximately 42 km

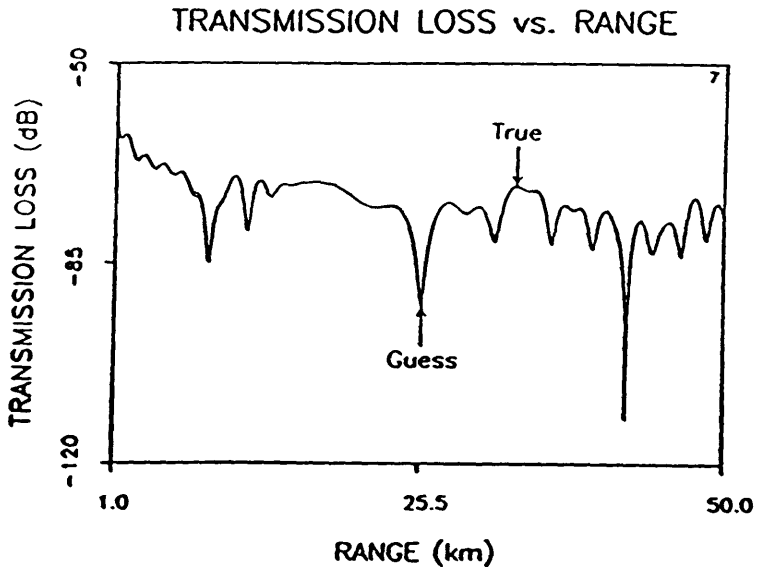

Figure 58. True and background transmission loss curves for test case 7. Because the source is placed on the channel axis, the shadow zone has disappeared.

indicates the possibility of a local error, the DWB and DWR solutions are predicted to give an accurate representation of the true transmission loss. This is confirmed by the transmission loss curves in Figures 61 and 62, and the relative errors in Figure 63.

The results of this chapter verify that the behavior of the DWB and DWR solutions can be qualitatively predicted from the quantitative single mode results of chapter 3. If the eigenfunctions do not change by more than approximately 7% and the receiver is well-illuminated, the perturbative solutions will give an accurate representation of the true field in the ocean waveguide to a range of 50 km.

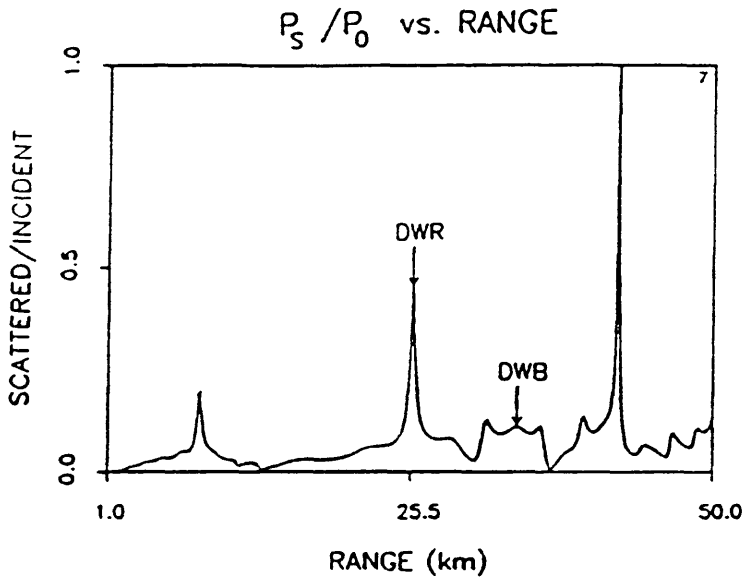

Figure 59. Ratio of the scattered field to the incident field for the DWB and DWR solutions for test case 7.

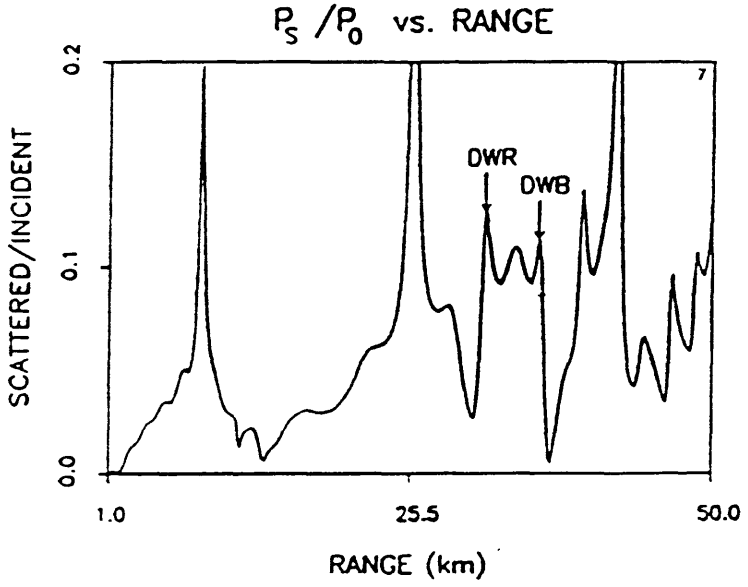

Figure 60. Expanded version of Figure 59. The ratio is always less than 1/4 and the DWB and DWR are expected to give accurate results.

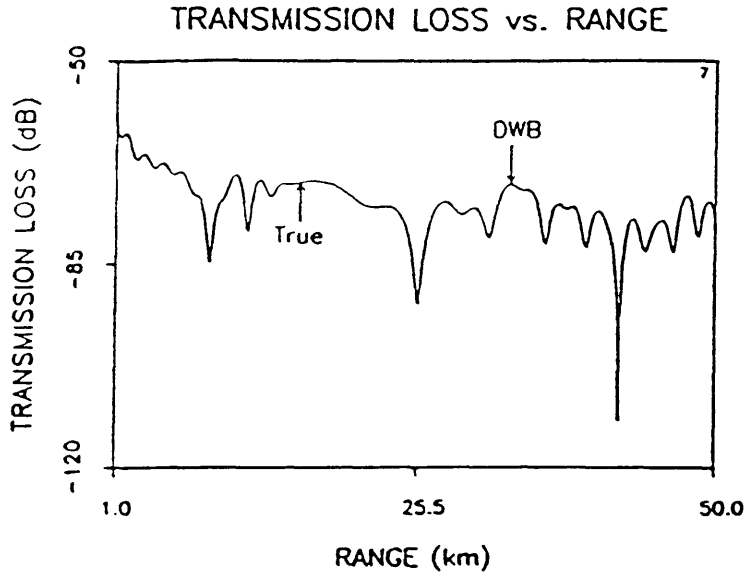

Figure 61. True and DWB transmission loss curves for test case 7. Because the waveguide is well-illuminated and the perturbation is small, the DWB gives a good approximation to the true solution.

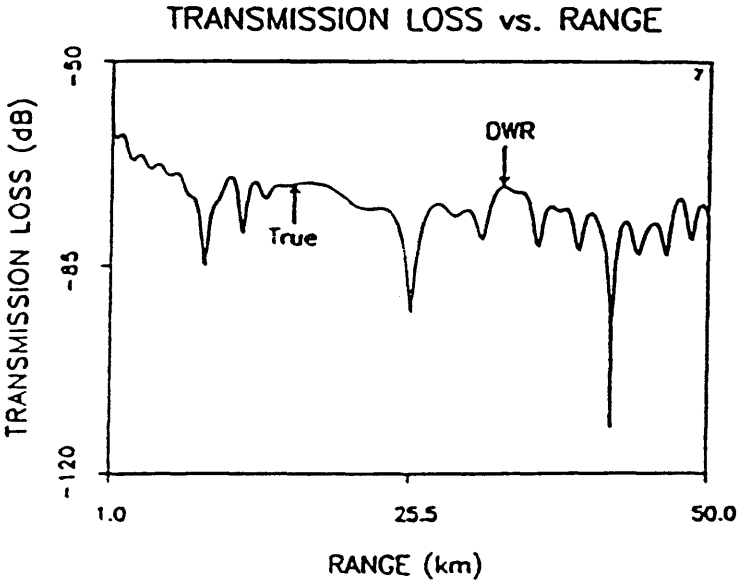

Figure 62. True and DWR transmission loss curves for test case 7. Because the waveguide is well-illuminated and the perturbation is small, the DWR gives a good approximation to the true solution.

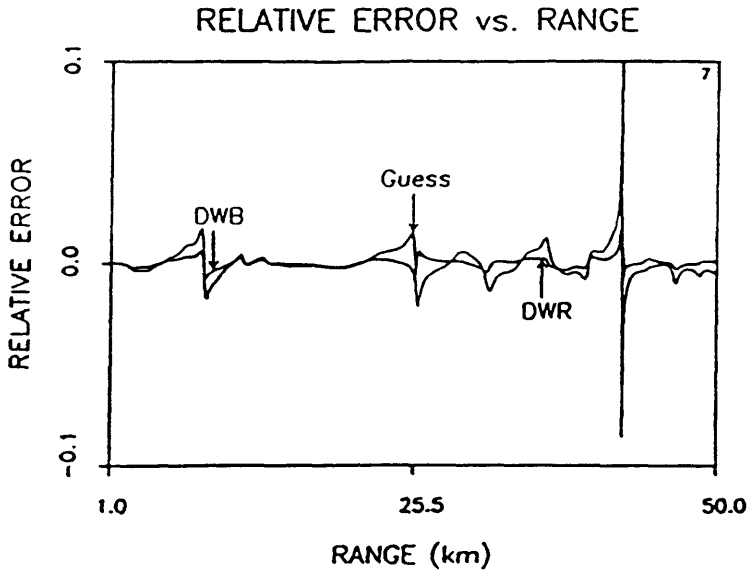

Figure 63. Relative error in the background, DWB and DWR transmission loss curves for test case 7.

5. INVERSION RESULTS

5.1 Introduction

Inverting for a depth-dependent perturbation in the ocean waveguide differs from the seismic case in which the location of and the impedance contrast across sharp boundaries in a layered earth is the goal (Cohen and Bleistein 1977; Raz 1981; Beydoun and Tarantola 1988). It also differs from the problem of object scattering for which the definition of the boundaries of a compact object placed in a constant background are desired (Mueller, Kaveh and Wade 1979; Slaney, Kak and Larsen 1984; Zapalowski, Leeman and Fiddy 1985).

In the ocean, the perturbations about the inhomogeneous background are smoothly varying functions of depth and extend over the entire range of propagation. The field structure in the deep ocean waveguide is characterized by multiply refracted energy as opposed to reflected energy. Therefore, if we think of the propagation paths in terms of rays, the raypaths can cross through a perturbation many times before reaching the receiver. Although in the seismic case, multiples (energy that has been reflected more than once from an acoustic boundary) are inherent in the data, they are removed by processing in order to display the primary reflection; energy that has traveled from the source to the layer back to the receiver directly. So while the multiply reflected energy is

removed in seismic processing, the multiply refracted energy in the ocean is the primary arrival.

The applicability of Fourier inversion techniques for recovering depth-dependent perturbations in the ocean waveguide is investigated in this chapter. Our goal is to relate the perturbation as a function of depth and the scattered field as a function of frequency as a Fourier transform pair within a linear transformation. As will be shown, the DWR and DWB scattered field data are constructed differently, but in both cases the transformation kernel is obtained from the DWB representation. Therefore, we concentrate on the attributes of the DWB kernel; the behavior of the amplitude and phase derivative with respect to depth as a function of depth, range and frequency. Certain criteria must be met in order for the transform relation to be valid; the amplitude must be a slowly varying function of frequency and the phase must be monotonic in depth and its frequency dependence known.

In the following sections, we discuss the inversion formalism, the attributes of the DWB kernel and the effect that band-limiting and phase averaging have on the reconstruction of a perturbation.

5.2 The Inversion Algorithm

The DWB scattered field representation is given in Eqs. (18.b) and (18.d).

Because the solution is given as a sum over all modes, explicit expressions for the amplitude and phase are not available. If, however, we perform the summation, we can write the scattered field, P_s, as

$$P_s(k_o,r,0,z,z_o) = \int_{z_1}^{z_2} B(k_o,r,z,z_o,z')e^{i\theta(k_o,r,z,z_o,z')} n_1(z')\,dz' , \tag{53}$$

where z_1 and z_2 define the limits of the perturbation in depth. The amplitude of the modal sum is defined as B, and the phase as θ. $Be^{i\theta}$ is defined as the transformation kernel relating the scattered field to the profile perturbation.

To construct the transform pair

$$P_s(k_o) \overset{FT}{<=>} n_1(\theta(z')) , \tag{54}$$

we generate the scattered data as a function of wavenumber using either DWB or DWR approximations. We then assume that the amplitude wavenumber dependence is known and can be absorbed into the scattered data and replace $B(k_o,r,z,z_o,z')$ with its wavenumber independent equivalent, $\tilde{B}(r,z,z_o,z')$; the modified scattered field is written as $\tilde{P}_s$. Next, we multiply both sides of Eq. (53) by the phase function, $e^{-i\theta(k_o,r,z,z_o,\overline{z'})}$, and integrate over wavenumber to obtain

$$\int_{-\infty}^{\infty} P_s(k_o,\tilde{r},0,z,z_o)e^{-i\theta(k_o,r,z,z_o,\overline{z'})}dk_o$$

$$= \int_{z_1}^{z_2} n_1(z')\tilde{B}(r,z,z_o,z')\int_{-\infty}^{\infty} e^{i\theta(k_o,r,z,z_o,z') - i\theta(k_o,r,z,z_o,\overline{z'})}dk_o\,dz' . \tag{55}$$

Assuming that the phase, θ, depends linearly on wavenumber, $\theta = k_o\tilde{\theta}$ where $\tilde{\theta}$ is

independent of k_o (or if not a transformation has been made to account for the dependence), and the phase is monotonic in z', then the k_o–space integral is identically equal to a delta function. The argument of the δ-function is the difference of our k_o-independent phase terms, $\tilde{\theta}(z')$ and $\tilde{\theta}(\overline{z}')$. Because the delta function is in terms of the phase instead of depth, we make a transformation obtaining the integrand as a function of the phase. As a result, the transform variables are k_o and $\tilde{\theta}(z')$. Therefore, we write Eq. (55) as

$$\int_{-\infty}^{\infty} \tilde{P}_s(k_o) e^{-ik_o\tilde{\theta}(\overline{z}')} dk_o = \int_{\tilde{\theta}z_1}^{\tilde{\theta}z_2} \frac{n_1(\tilde{\theta}(z'))\tilde{B}(\tilde{\theta}(z'))\, 2\pi\delta\left[\tilde{\theta}(z') - \tilde{\overline{\theta}}(\overline{z}')\right]}{|\, d\tilde{\theta}/dz'\,|_{z=\overline{z}'}} d\tilde{\theta}, \tag{56}$$

where $d\tilde{\theta}/dz'$ is the Jacobian of the transformation. For simplicity, we have excluded the parameter dependence in the expression; we retain only the transform variables $\tilde{\theta}(z')$ and k_o explicitly. Evaluation of the phase integral gives

$$n_1(\tilde{\theta}(z')) = \frac{|\, d\tilde{\theta}/dz'\,|_{z=\overline{z}'}}{2\pi\tilde{B}(\tilde{\theta}(z'))} \int_{-\infty}^{\infty} \tilde{P}_s(k_o) e^{-ik_o\tilde{\theta}(\overline{z}')} dk_o\,. \tag{57}$$

Thus, we have obtained a linear transform relation between the scattered field data as a function of wavenumber and the perturbation as a function of the phase.

To form the DWB scattered field, we generate the true, P, and background, P_o, field representations as a function of wavenumber and subtract thereby obtaining

$$P_s^{(B)}(k_o) = P(k_o) - P_o(k_o)\,. \tag{58}$$

The DWR scattered field is

$$P_s^{(R)}(k_o) = P_o(k_o)\ln\frac{P(k_o)}{P_o(k_o)}\,. \tag{59}$$

The DWB and DWR representations of the scattered field will closely approximate the data generated from Eq. (53) if the solutions are within their range of validity and the inversion criteria discussed above are satisfied. In the next section, we investigate the behavior of the amplitude and the phase derivative of the DWB kernel for two sound speed profiles. We also outline the processing steps necessary to formulate the inversion and the effects that these processing steps have on the output of the Fourier inversion.

5.3 Investigation of the DWB kernel

The first case investigated is the NORDA 2A profile whose parameters where listed previously in Table 1. A pixel map of the transmission loss over a range of 1 to 50 km is illustrated in Figure 64. The source frequency is 50 Hz. Because the sound speed minimum is located at the ocean surface, there are multiple surface reflections interfering with the refracted energy in the waveguide.

As indicated in section 5.1, it is necessary to determine the behavior of the amplitude and phase derivative of the DWB kernel as a function of wavenumber.

Figure 65 illustrates the amplitude of the DWB kernel while Figure 66 illustrates the phase derivative arising from the transformation from z' to $\tilde{\theta}(z')$.

Comparing Figures 64 and 65, we see that they contain similar but shifted features. The shift is most apparent in the location of the lower turning points of the field. The range dependence of the background field is $H_o^{(2)}(\xi r) = J_o(\xi r) - iY_o(\xi r)$ while the range dependence of the scattered field is $H_1^{(2)}(r) = J_1(\xi r) - iY_1(\xi r)$. In the far field, $J_1(\xi r) \sim Y_o(\xi r)$ and $J_o(\xi r)$ and $Y_1(\xi r)$ are π out of phase (Abramowitz and Stegun 1984).

The structure in Figure 66 is essentially the instantaneous vertical wavenumber, k_z, analogous to the instantaneous frequency in complex seismic trace analysis (Taner, Koehler and Sheriff 1979). The yellows and reds denote positive values, black is the zero transition and the blues are negative values. The association of the phase derivative with k_z is verified by the zero transition regions in Figures 65 and 66. For instance, at the deep turning points of the amplitude, the phase derivative is zero; i.e. the propagation is horizontal. Many other zero crossings are evident in the figure and each corresponds to $k_z = 0$.

Recalling that the phase needs to be monotonic for a valid inverse, we see that at least globally this criterion cannot be met. However, if we can find a region where the phase is locally monotonic, and the rest of the inversion criteria are met, then we can attempt a perturbation reconstruction over a limited range in depth.

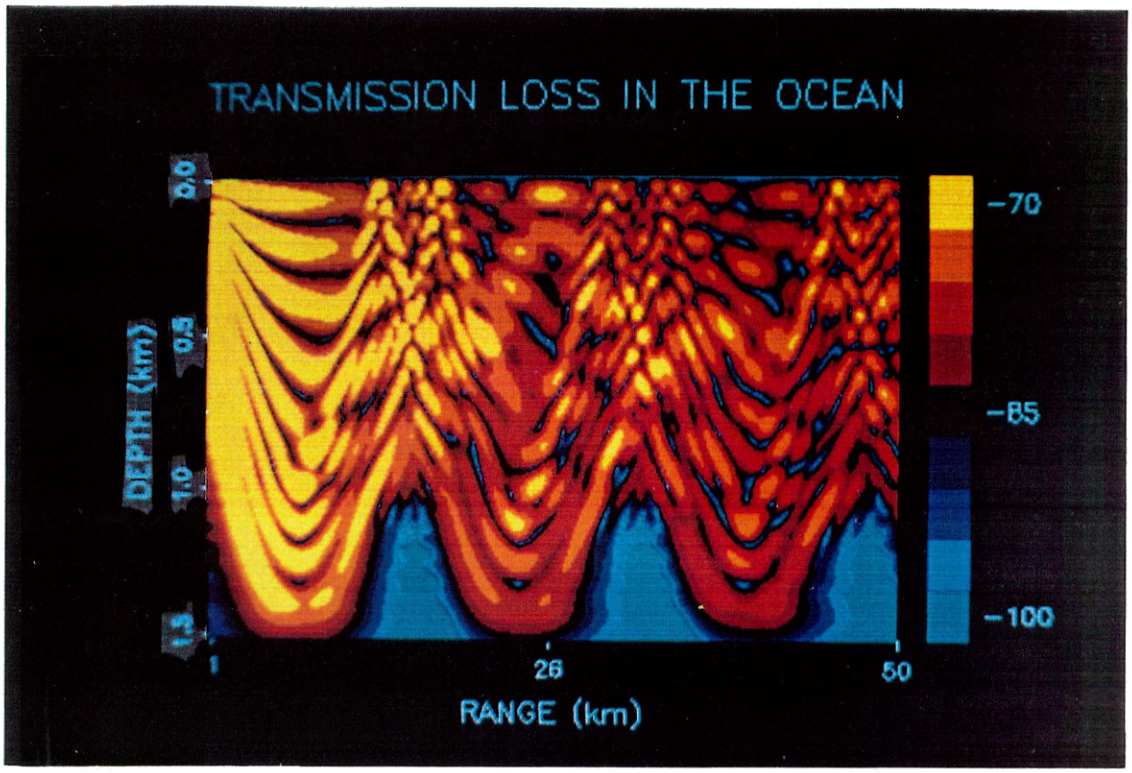

Figure 64. Transmission loss for the NORDA 2A profile illustrated in Figure 35. The source is placed at a depth of .5 km and the source frequency is 50 Hz.

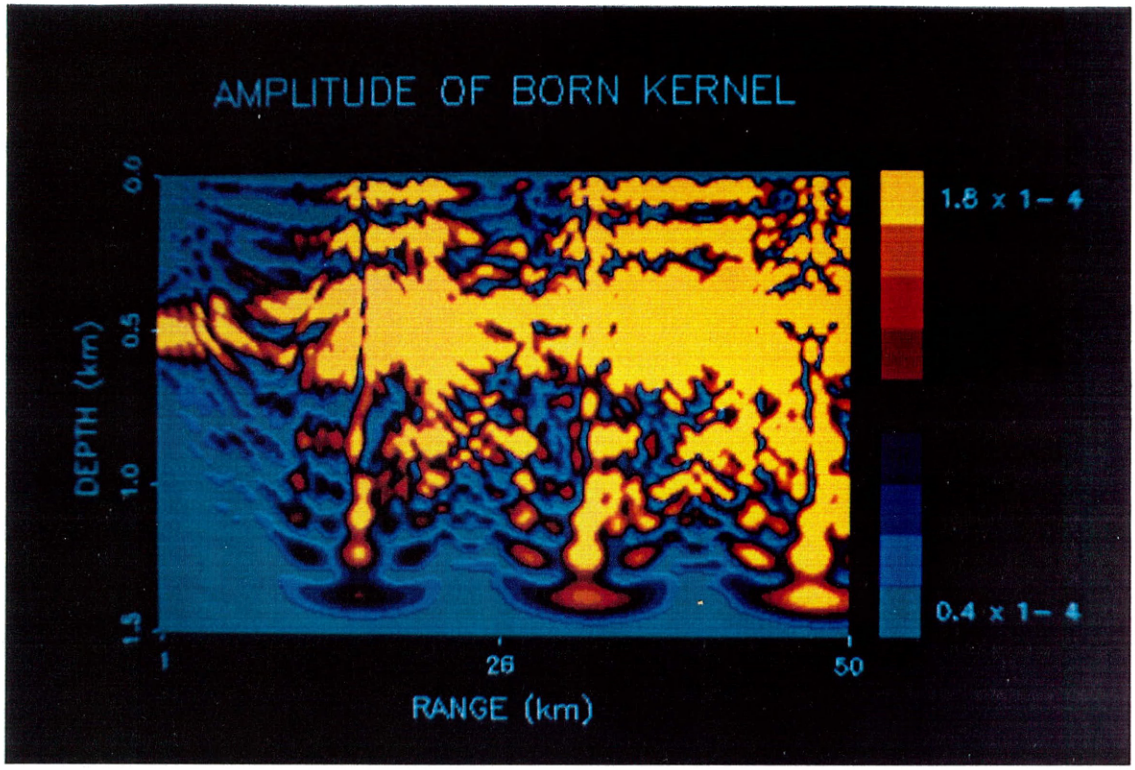

Figure 65. Amplitude of the DWB kernel for the NORDA 2A profile. The source is placed at a depth of .5 km and the source frequency is 50 Hz. Note the position of the lower turning points as compared to Figure 64.

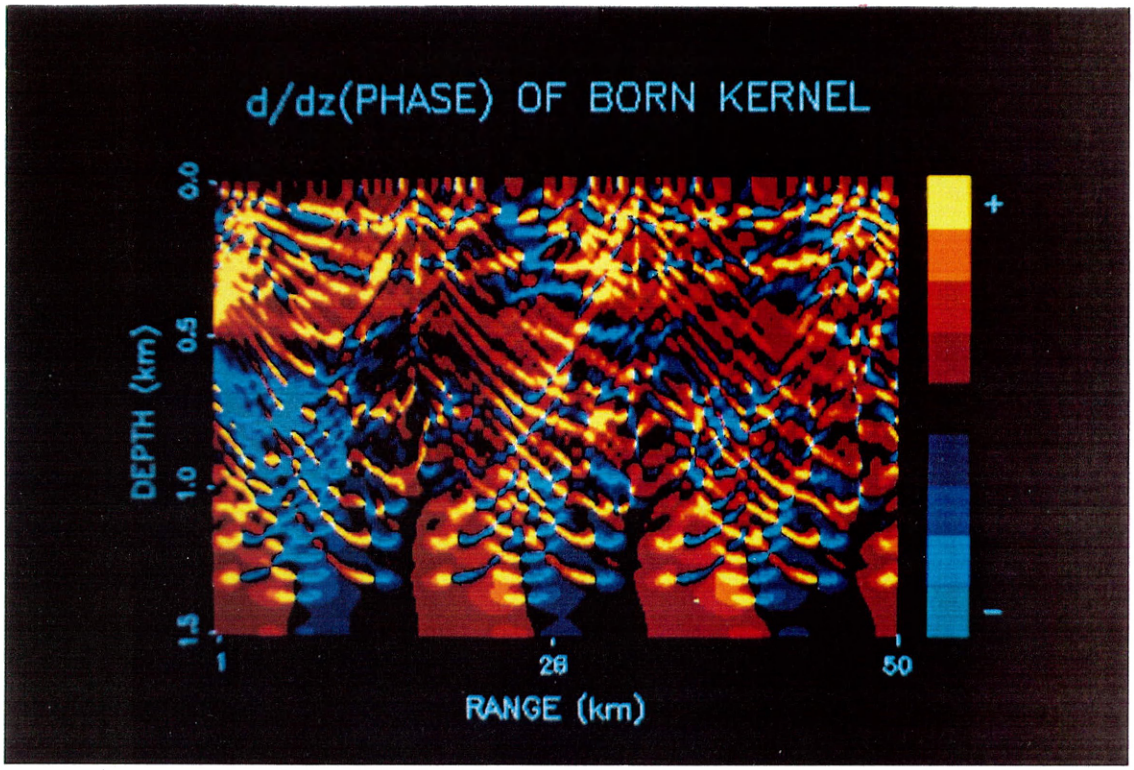

Figure 66. Derivative of the phase with respect to depth for the NORDA 2A profile. The source is placed at a depth of .5 km and the source frequency is 50 Hz. The complicated pattern of zero crossings is due to the interference of reflected and refracted energy.

The next step is to check the frequency dependence of the amplitude and phase derivative or equivalently, the phase, at a fixed range (the phase is constructed from the phase derivative to avoid phase unwrapping). The amplitude was found to have a $1/k_o$ approximate dependence and so are multiplied by k_o. The phase derivative, on the other hand goes approximately like k_o, and accordingly, is divided by k_o. The resultant amplitude and phase derivative curves are illustrated in Figures 67 and 68, respectively, for 10 frequency values ranging from 5 to 50 Hz. Although the curves in each plot are of the same order of magnitude, they are not identical. Therefore, only frequency-averaged versions of these functions are available for use in the inversion algorithm. In addition, because the phase is numerically constructed from its derivative, the spikes in the latter must be selectively removed using a local mean amplitude comparison in order for the algorithm to be stable. We also note that the zero crossings in Figure 68 occur at different depths for different frequencies; therefore, for this profile, the phase monotinicity is a function of frequency. The averaged (over depth and frequency) curves for the amplitude and phase derivative are illustrated in Figures 69 and 70, respectively. Note that it is these averaged functions that will be used in an inversion.

Earlier in the discussion, we postulated that a reconstruction could be attempted over a compact region in depth if the phase were locally monotonic. However, we first need to consider how band-limiting, in particular the absence of

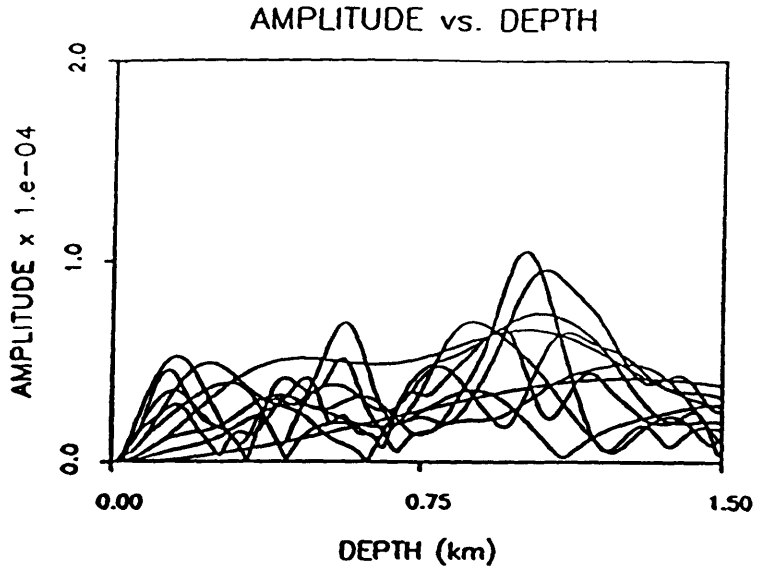

Figure 67. Amplitude of DWB kernel for 10 source frequencies generated using the NORDA 2A profile. The source depth is .5 km and the range is 30 km.

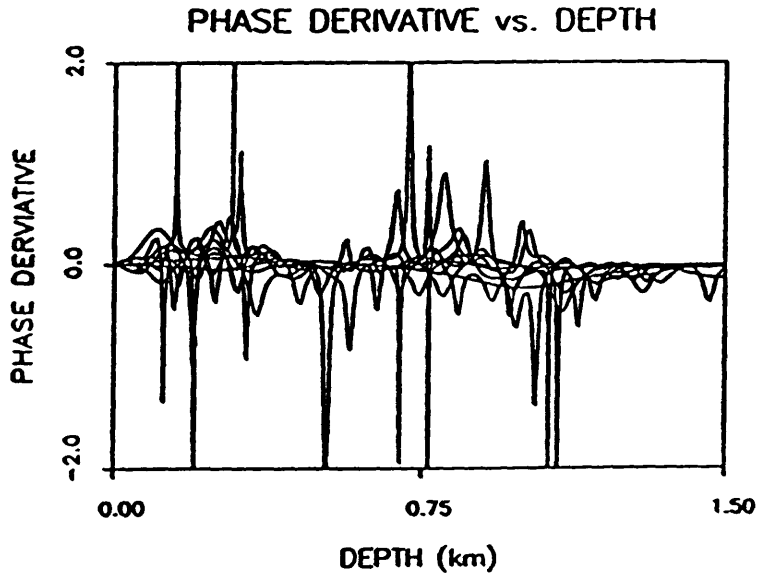

Figure 68. Derivative of the phase with respect to depth for 10 source frequencies generated using the NORDA 2A profile. The source depth is .5 km and the range is 30 km.

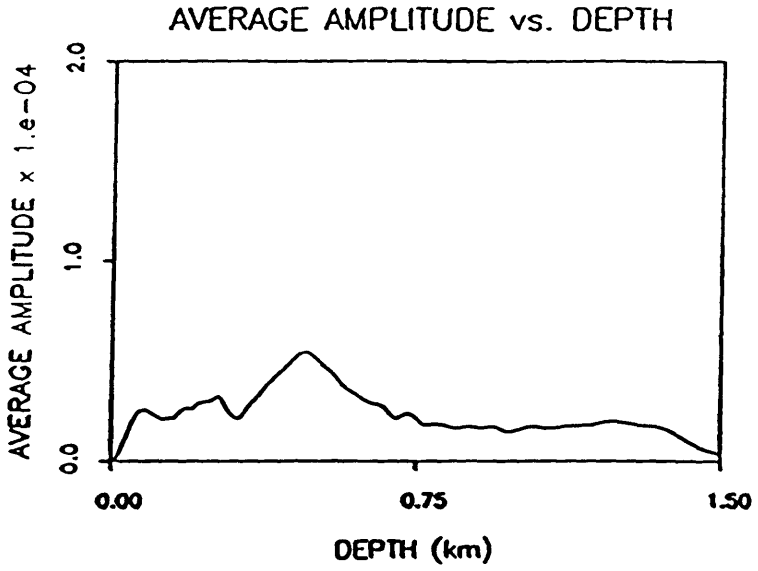

Figure 69. Frequency-averaged amplitude of DWB kernel generated using the NORDA 2A profile. The source depth is .5 km and the range is 30 km.

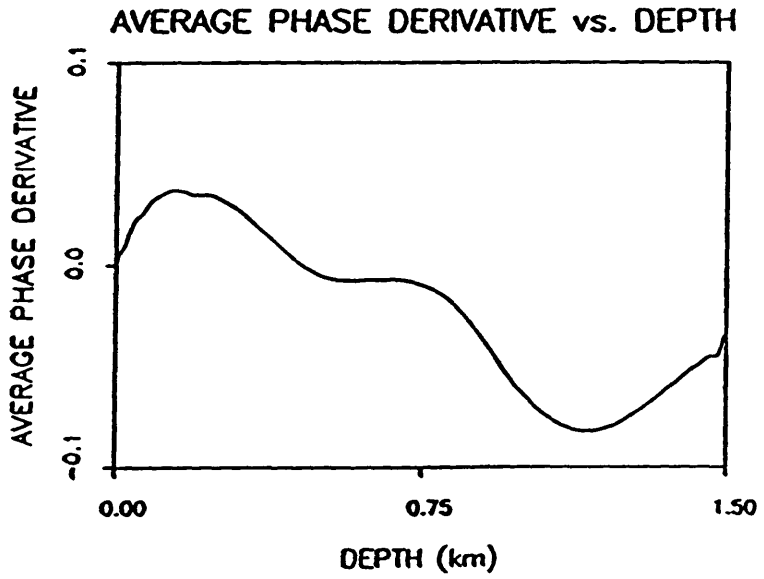

Figure 70. Frequency and depth-averaged derivative of the phase with respect to depth generated using the NORDA 2A profile. The source depth is .5 km and the range is 30 km.

zero frequency, affects the recovery of a given perturbation. Also of importance in the reconstruction process is the effect of using numerically constructed averaged quantities. For these reasons, we next investigate the effects of phase averaging and band-limiting on the Fourier reconstruction of two different perturbations.

We first look at our ability to reconstruct a simple triangular perturbation (see Figure 71, the true perturbation has a maximum value of 1 at 100 m). The perturbation is centered at 100 m and its extent is 200 meters. The entire region over which the inversion is performed is assumed to be 700 meters. Because the perturbation is a real positive function, we know from Fourier analysis that zero frequency is required to fully reconstruct the amplitude of the perturbation. However, very low frequencies are unavailable in an actual inversion, and so first we illustrate the effect that systematically removing the lowest frequency values has on the perturbation recovery. If the sampling interval is taken to be .684 m (1024 samples), then the sampling interval in frequency (where c_o is 1500 m/s) is $\sim 1.0\, s^{-1}$. If we generate the Fourier transform of the triangular function, zero the low frequency components of the transform one sample at a time, and then inverse transform, we obtain the curves in Figure 71. The actual function has a maximum amplitude of 1. Successively smaller amplitudes represent the reconstruction with one less frequency component. As the near-zero components are discarded the maximum amplitude of the function decreases correspondingly and the function is shifted as a result of the removal of the zero frequency component.

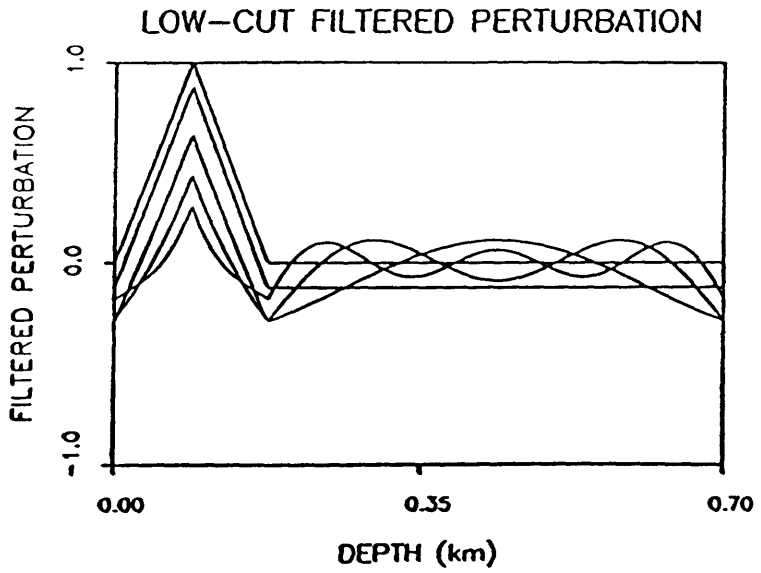

Figure 71. Effect of low-cut filtering on the Fourier reconstruction of a positive triangular perturbation.

We next investigate the effect of numerically constructing the phase from the phase derivative. The first step is to obtain the transform of the triangular perturbation. Next, we calculate the derivative of the phase of the transform kernel and from this function we integrate to find the unwrapped phase. If the phase derivative is a smooth function of depth, then the previous step is stable. However, as discussed above, the phase derivative (e.g. Figure 68) has large local spikes and must be smoothed before calculation of the phase and this smoothing process has a significant effect on the Fourier inversion.

Illustrated in Figure 72, are the perturbation reconstructions obtained from averaging over 0 to 250 points in 50 m increments. It is important to note that

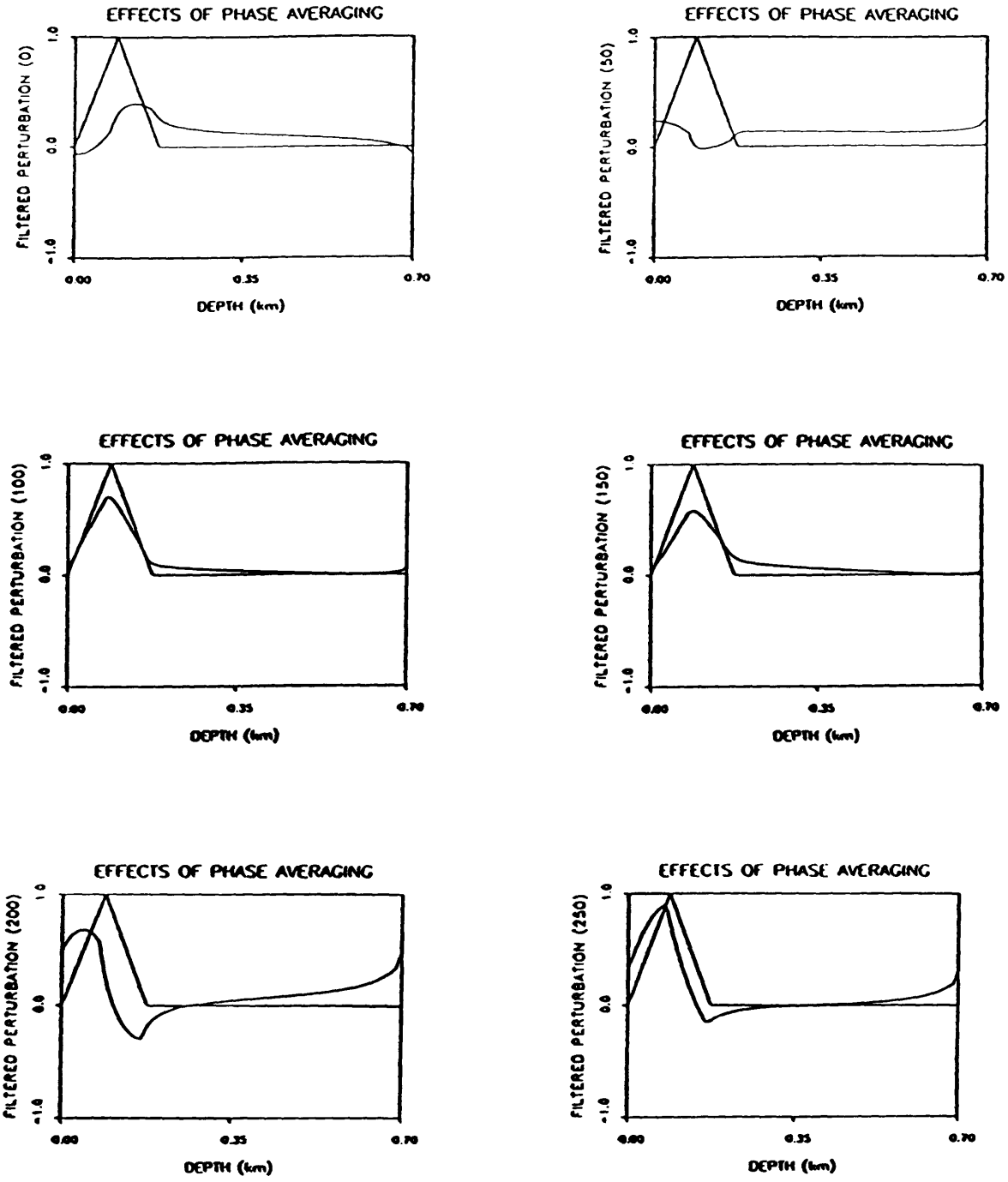

Figure 72. Effect of phase-averaging on the Fourier reconstruction of a positive triangular perturbation.

these curves are the real part of the function obtained from the inverse transform. The averaging process has destroyed the original symmetry of the transform; the spectrum no longer corresponds to that of a real function. Although in the actual inversion process we are not averaging the phase of the data (as done here), but instead, averaging the Fourier phase, the effect is the same; components needed to reconstruct the perturbation are in error.

We now investigate the effects that band-limiting and phase averaging have on the recovery of a second perturbation. The perturbation has the same extent and amplitude of the previous example, but now is placed evenly about zero. The effect of band-limiting is illustrated in Figure 73. Because the DC component is

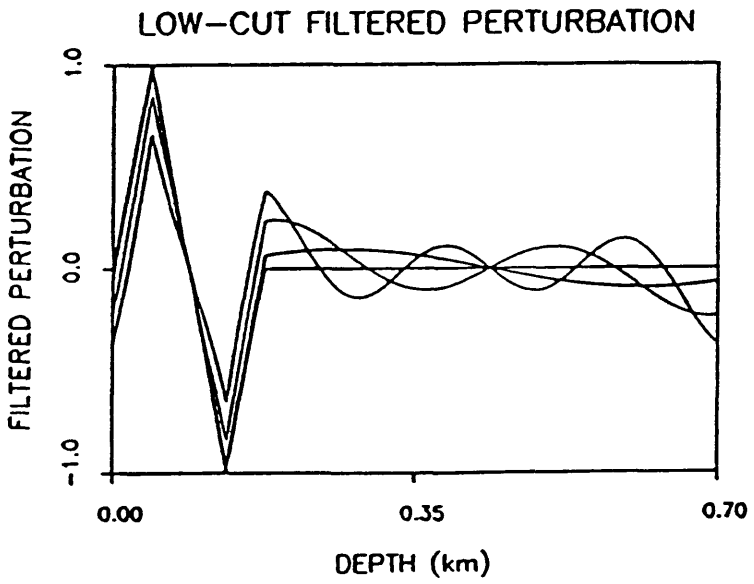

Figure 73. Effect of low-cut filtering on the Fourier reconstruction of a symmetric (about zero) perturbation.

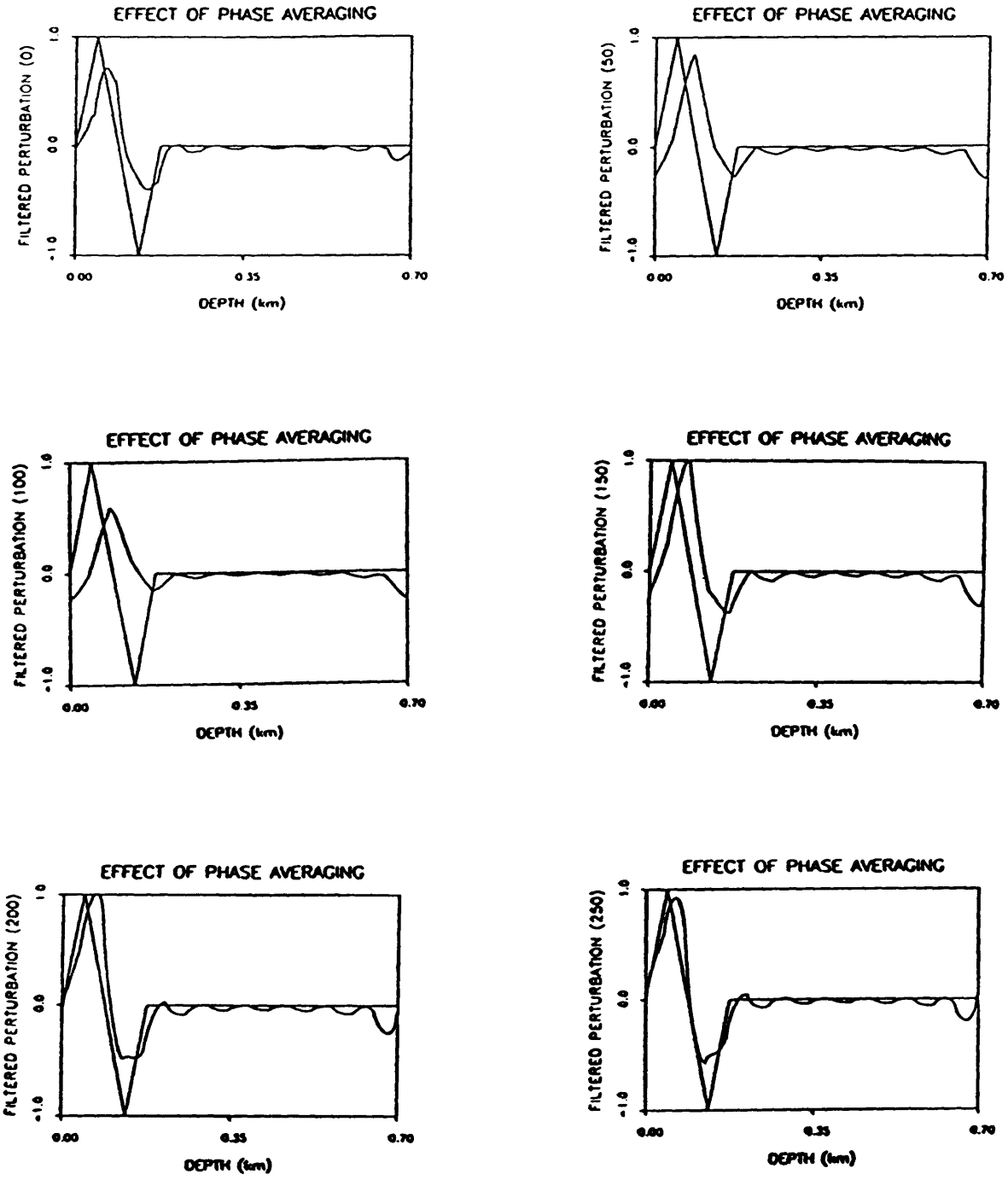

Figure 74. Effect of phase-averaging on the Fourier reconstruction of a symmetric perturbation.

identically zero, elimination of the near-zero components (0-4 Hz) results in only half the amplitude loss as compared to Figure 71.

The results obtained from averaging the phase of the spectrum are illustrated in Figure 74. The reconstructions are more consistent as compared to Figure 72; the structure is well-identified for any average filter length.

From the examples discussed above, it appears that the second type of perturbation would be a good choice to try in the inversion algorithm. However, no consistent reconstructions could be obtained for either type of perturbation in the NORDA 2A environment. In fact, although we will briefly discuss the deep ocean examples (test cases 6 and 7, chapter 4), no reconstructions were obtained for any profiles studied.

Several explanations for the failure of the algorithm can be offered. First is the behavior of the amplitude and phase with frequency. Because these functions vary with frequency, only averages are available for use in the reconstruction. As previously discussed, the effect of averaging, in particular, phase averaging has a strong effect on the output of the Fourier transform. Second, the phase is not monotonic; the transformation from depth to phase is not one-to-one. Therefore, there exists a neighborhood (of unknown extent) about the stationary phase point in which the inversion formulation is invalid.

Although we are unable to recover a perturbation using this inversion

technique, we nonetheless investigate the behavior of the Born kernel for the deep ocean profiles (examples 6 and 7, chapter 4) in order to gain additional insight. Illustrated in Figures 75, 76 and 77 are the transmission loss of the field and the amplitude and phase derivative of the Born kernel, respectively, constructed using the parameters of test case 6. Because this is a strongly refractive profile, the structure in the three figures is sharply defined. The energy is almost purely refractive. The amplitude and phase derivative curves for 10 frequencies (5 to 50 Hz) at a range of 30 km are illustrated in Figures 78 and 79 with their respective averages in Figures 80 and 81. As compared to the Figures 67 and 68, these curves are nearly identical, except at the localized spikes and low frequencies. In this case, the stationary points consistently occur within a small region at a depth of 2 km. However, at a range of 30 km and a receiver depth of 500 m, we are in a shadow zone. From the modeling results of chapter 4, we recall that the DWB and DWR solutions were unable to give a valid approximation to the true solution. Unfortunately, if we move farther out in range the amplitude and phase derivative behavior again varies with wavenumber. Therefore, although the DWB kernel is stable (in the sense that the Fourier inversion is valid) over the upper region of the waveguide, the lack of field structure in this region makes a perturbation reconstruction impossible.

In the last example, we investigate the DWB kernel when the waveguide is strongly refractive and well-illuminated; test case 7. The transmission loss and the

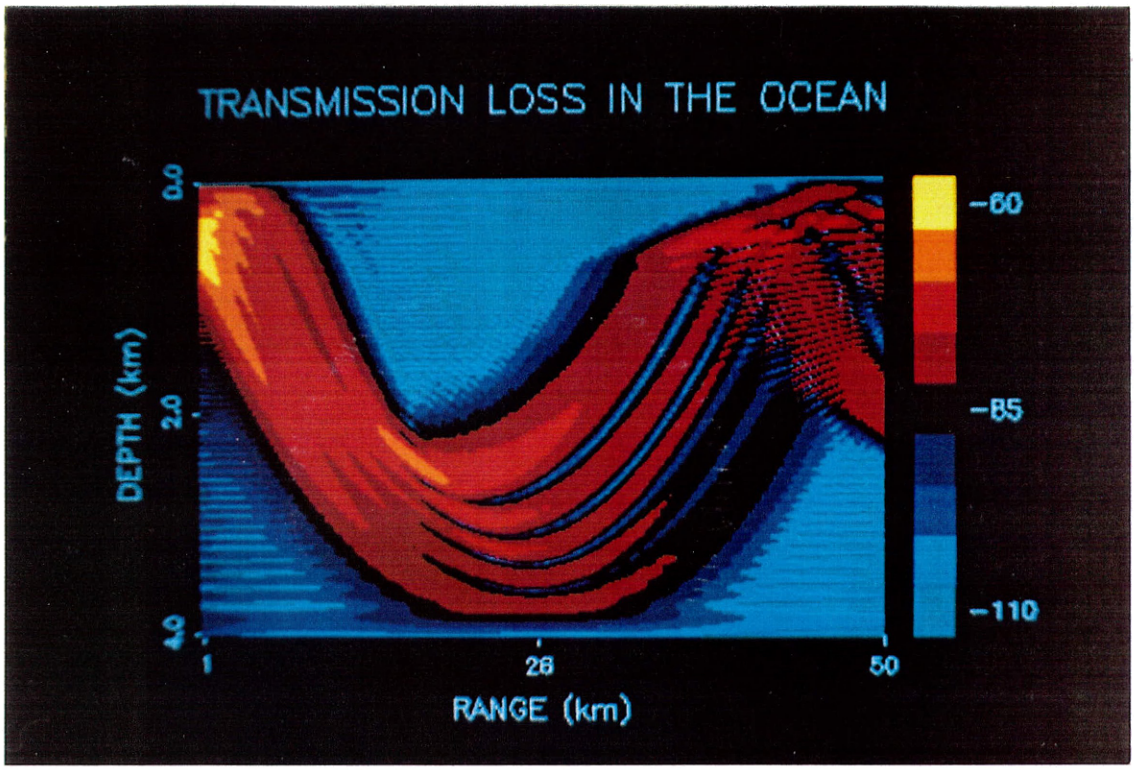

Figure 75. Transmission loss calculated using the profile and source-receiver geometry of test case 6. The source frequency is 50 Hz.

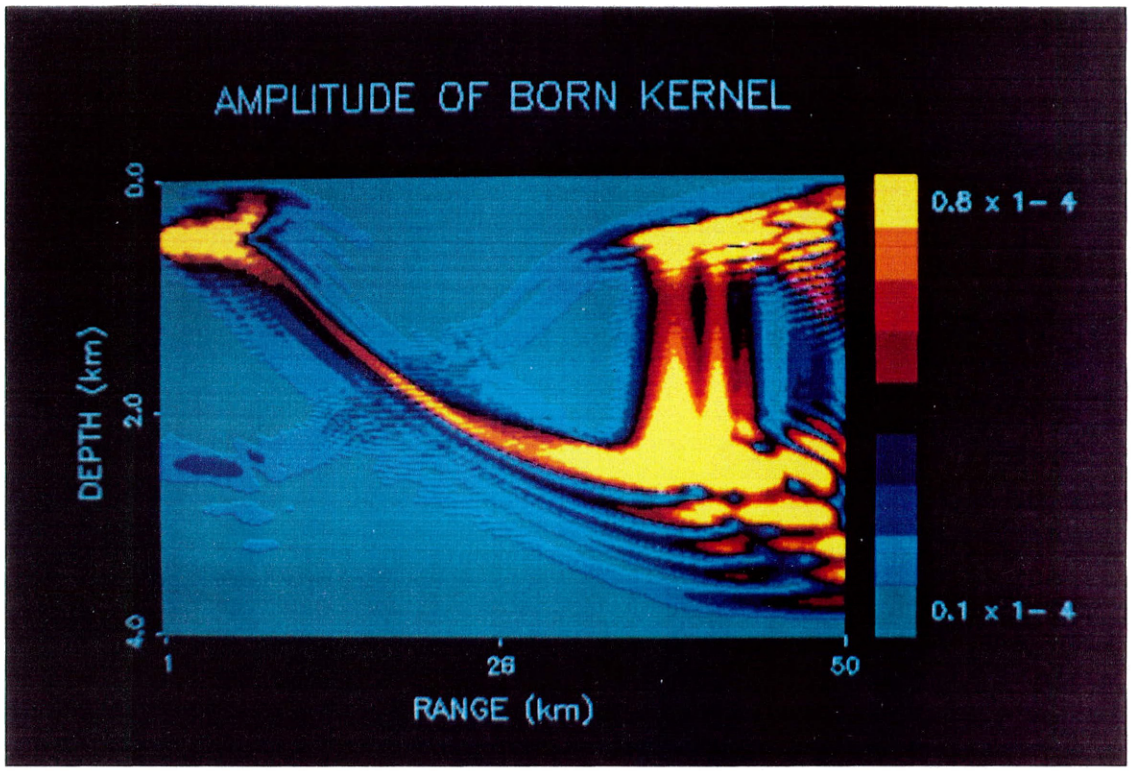

Figure 76. Amplitude of the DWB kernel calculated using the profile and source-receiver geometry of test case 6. Note the trapping of energy in narrow bands due to the source placement.

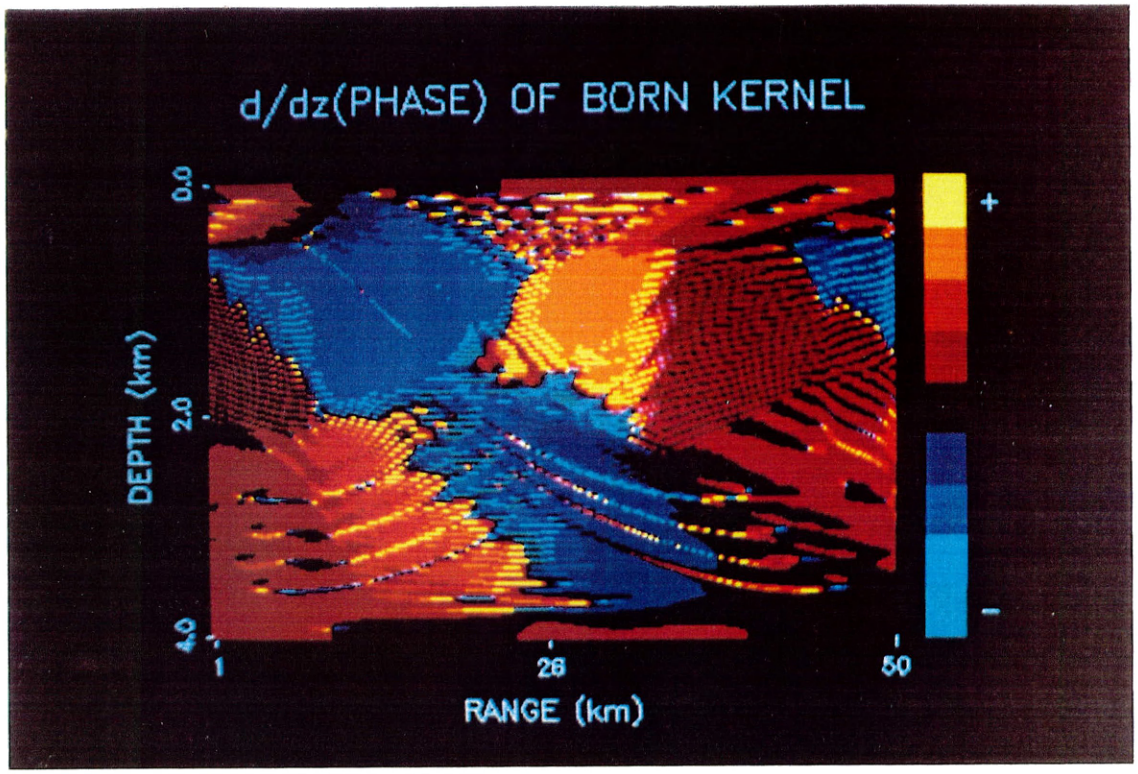

Figure 77. Derivative of the phase with respect to depth calculated using the profile and source-receiver geometry of test case 6. As compared to Figure 66, there are broad regions in depth for which the phase is monotonic.

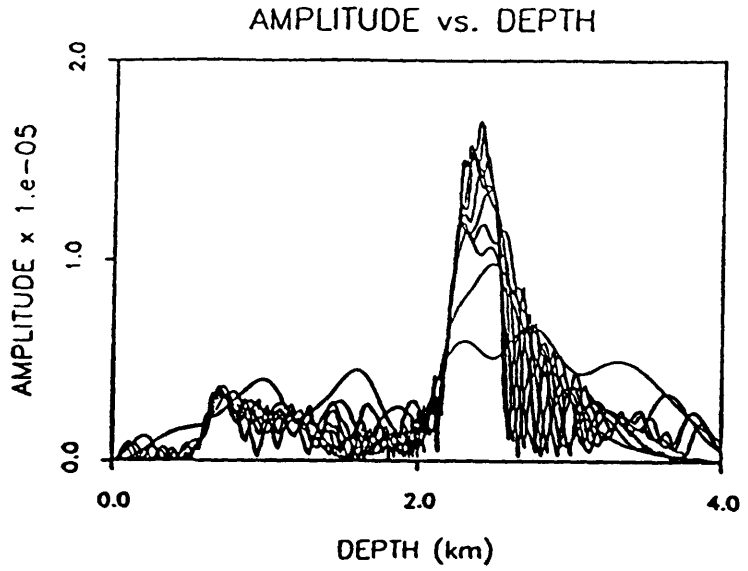

Figure 78. Amplitude of DWB kernel for 10 source frequencies generated using the profile and source-receiver geometry of test case 6. The range is 30 km.

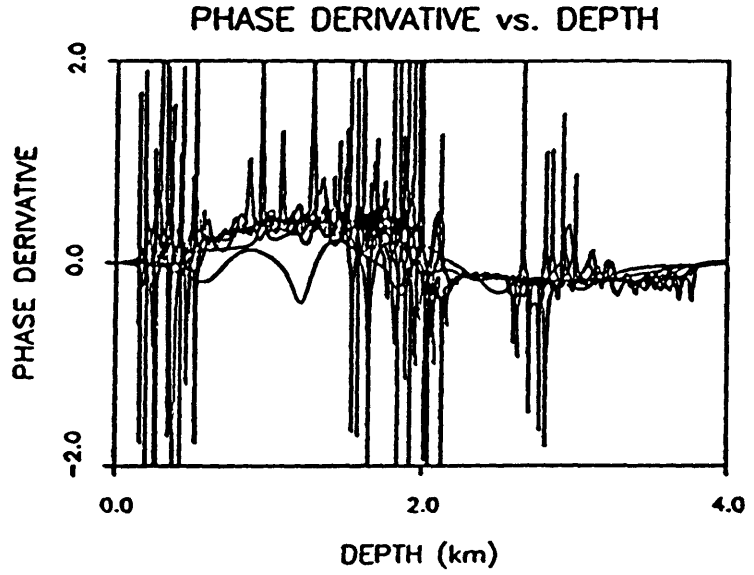

Figure 79. Derivative of the phase with respect to depth for 10 source frequencies generated using the profile and source-receiver geometry of test case 6. The range is 30 km.

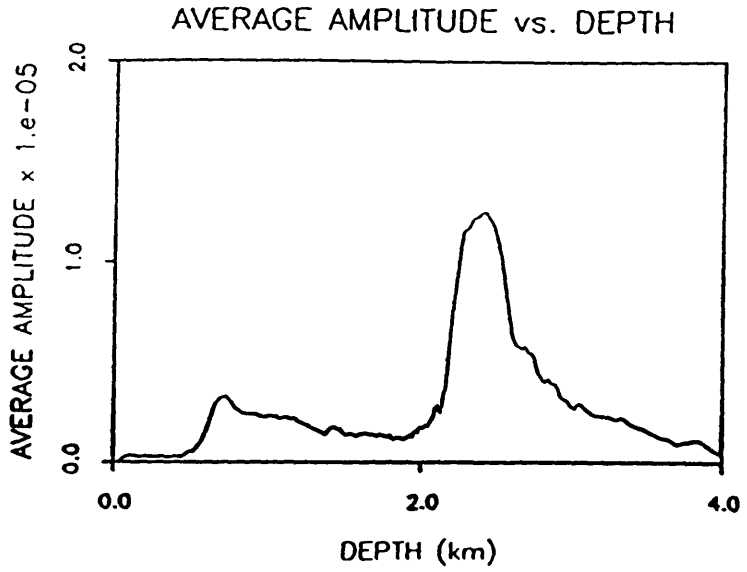

Figure 80. Frequency-averaged amplitude of DWB kernel generated using the profile and source-receiver geometry of test case 6. The range is 30 km.

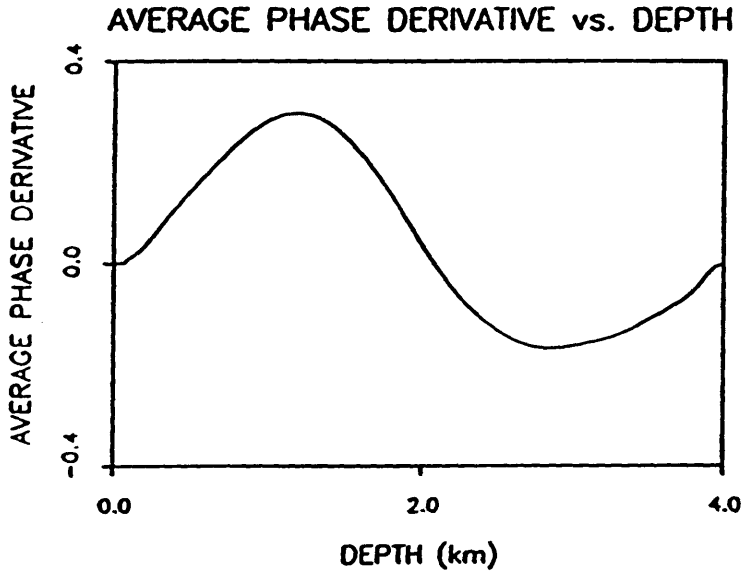

Figure 81. Frequency and depth-averaged derivative of the phase with respect to depth generated using the profile and source-receiver geometry of test case 6. The range is 30 km.

amplitude and phase derivative of the DWB kernel are illustrated in Figures 82, 83 and 84. Although the structure is regular as compared to the NORDA 2A test case, we see from the phase derivative that there are many zero crossings over the depth of the waveguide. As illustrated by the amplitude and phase derivative curves versus wavenumber, (Figures 85 and 86) and their averages (Figures 87 and 88), the behavior of the DWB kernel varies with wavenumber. In Figure 88, we observe two stationary points and, in addition, a higher order stationary point in the vicinity of the source. Therefore, for this source geometry, we have a well-illuminated waveguide, but the points of stationarity render the inversion algorithm invalid.

5.4 Summary of the Inverse Problem

The refractive nature of propagation in the ocean waveguide makes a wide-band Fourier-like inversion for a single source-receiver, invalid. In regions where the waveguide is well-illuminated, there are multiple turning points (where the Jacobian goes through a zero) and the transformation relating the scattered field data and a depth-dependent perturbation is no longer 1 to 1. If the energy is trapped within a narrow beam due to source placement, then the regions in which the phase is monotonic coincide with shadow zones in the waveguide; in these regions, the DWB and DWR approximations yield inaccurate results.

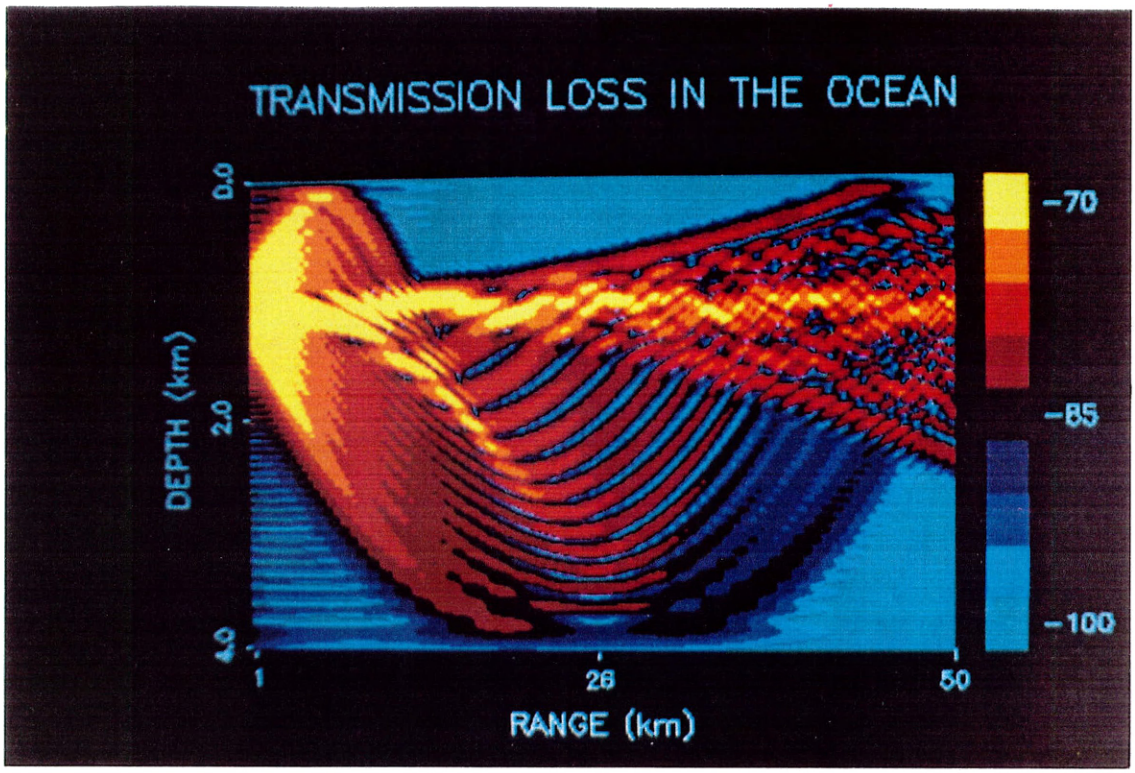

Figure 82. Transmission loss calculated using the profile and source-receiver geometry of test case 7. The source frequency is 50 Hz.

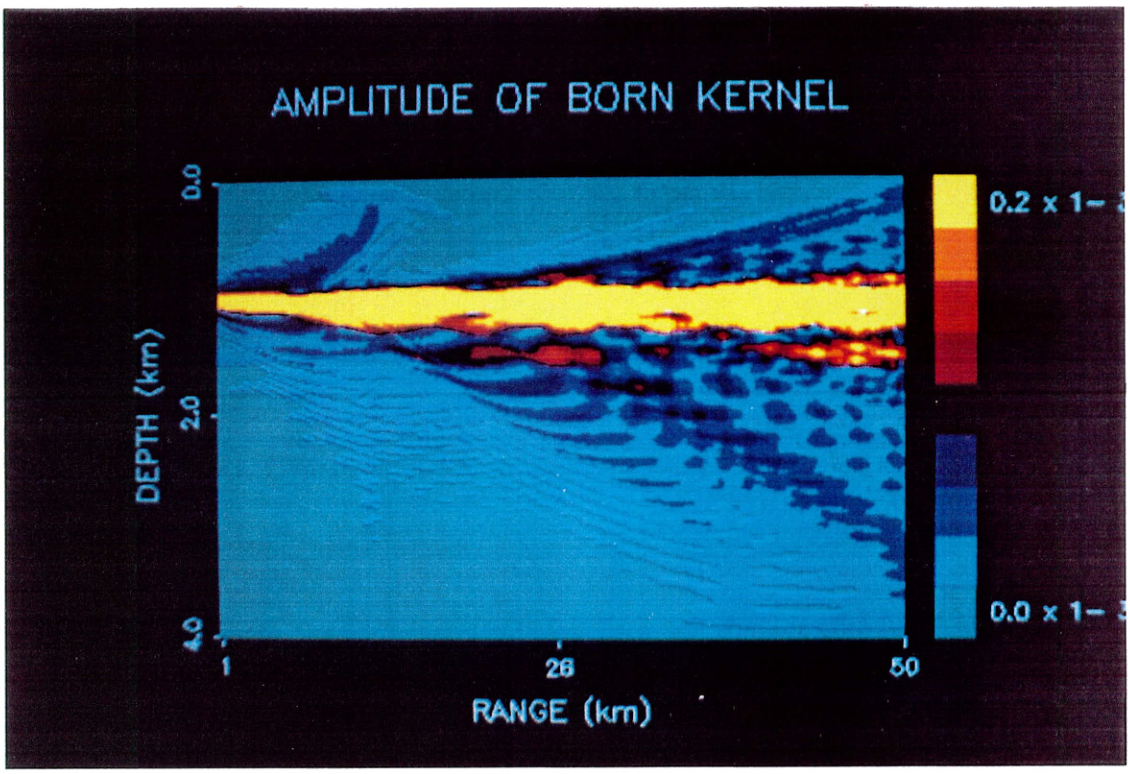

Figure 83. Amplitude of the DWB kernel calculated using the profile and source-receiver geometry of test case 7. Note the trapping of energy near the channel axis.

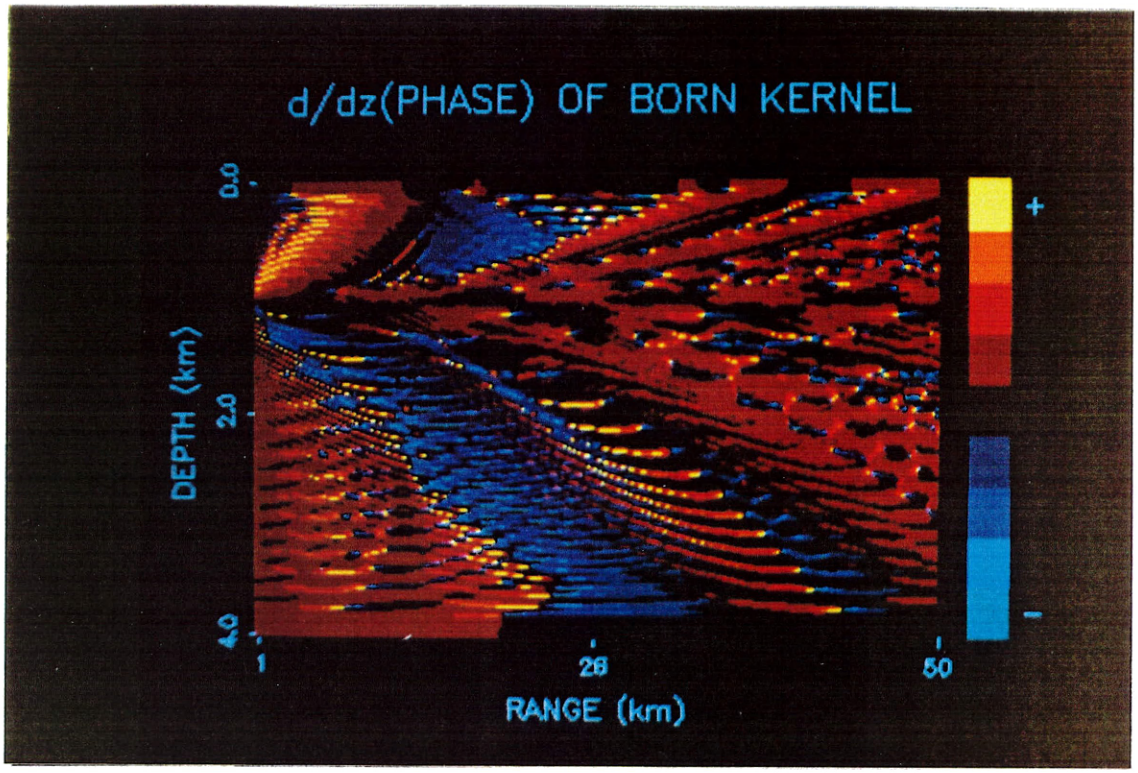

Figure 84. Derivative of the phase with respect to depth calculated using the profile and source-receiver geometry of test case 7. As in Figure 66, there are many zero crossings. In this case the turning points are due to refraction within the waveguide.

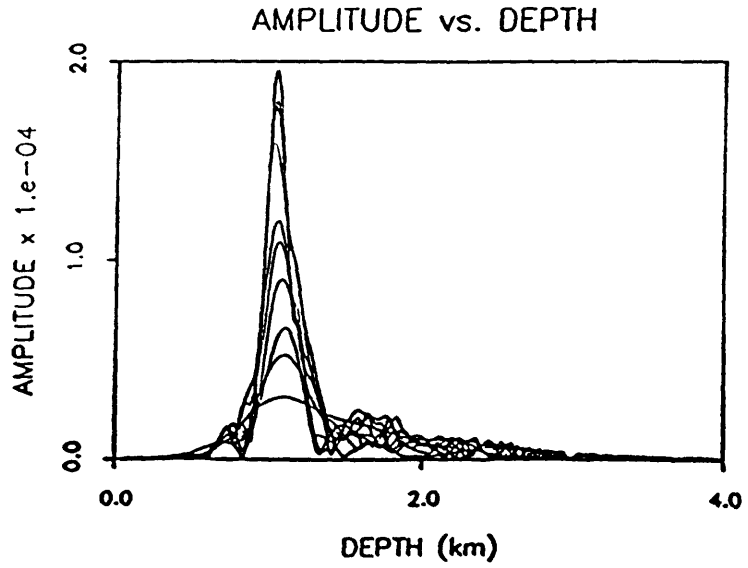

Figure 85. Amplitude of DWB kernel for 10 source frequencies generated using the profile and source-receiver geometry of test case 7. The range is 30 km.

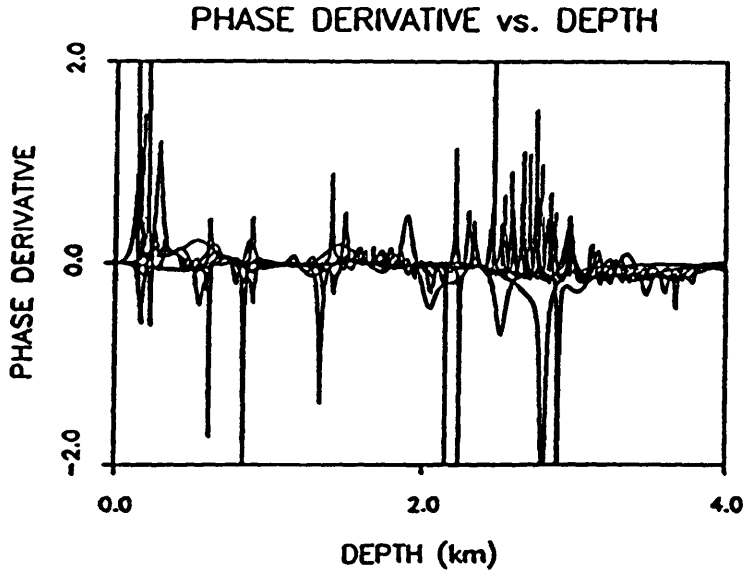

Figure 86. Derivative of the phase with respect to depth for 10 source frequencies generated using the profile and source-receiver geometry of test case 7. The range is 30 km.

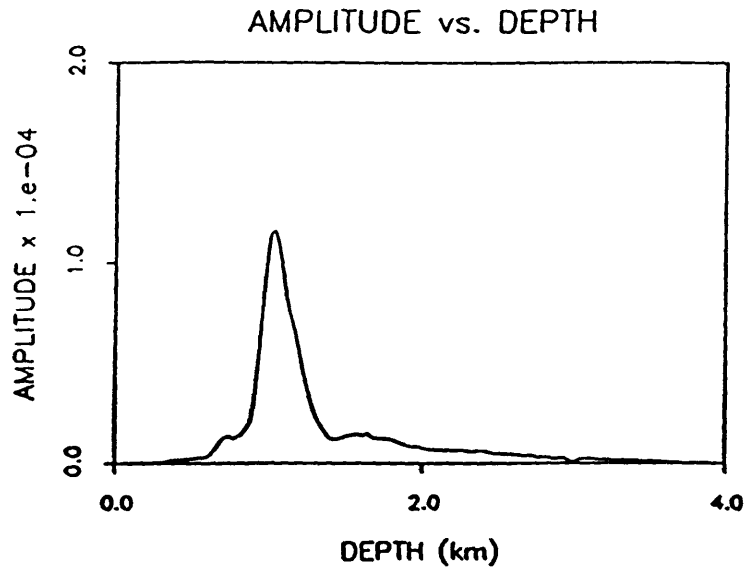

Figure 87. Frequency-averaged amplitude of DWB kernel generated using the profile and source-receiver geometry of test case 7. The range is 30 km.

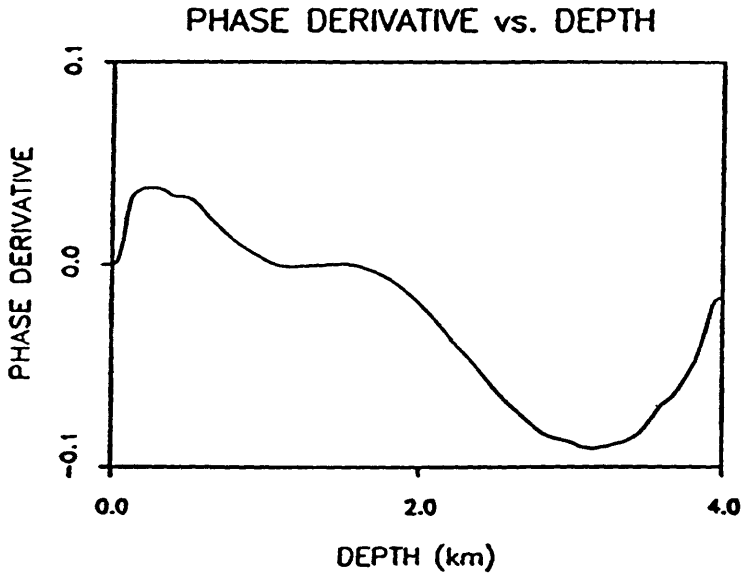

Figure 88. Frequency and depth-averaged derivative of the phase with respect to depth generated using the profile and source-receiver geometry of test case 7. The range is 30 km.

As an alternative to a wavenumber inversion, we could formulate the inverse given multiple receiver configurations, either horizontal or vertical arrays, for a single frequency source. For example, a closely-spaced horizontal array would permit the tracking of stationary points in the phase of the kernel, (which are related to the eigenray arrivals) and therefore, differentiation of the arrivals. Recovery of a profile perturbation could be attempted by first evaluating the depth integral at all receiver ranges using the method of stationary phase. If we then assume that the magnitude of the perturbation at the stationary point for a given depth is the same at all receivers, the perturbation at each depth can be recovered using a matrix inversion.

CONCLUSIONS

The Born and Rytov approximations to the transmitted field, in which the direction of propagation is in range and the perturbation is in depth, behave in much the same way as the solutions in a layered earth. In a constant velocity earth, the depth-dependent wave functions are have the same functional form for the true and background fields; therefore, the errors are simple to derive and interpret. In fact, the Born and Rytov mode coefficients can be projected from the solutions to give the exact error in the approximations for a single mode. As verified by the constant velocity example, the validity of the Born solution depends on the size and extent of the perturbation; the scattered field must be less than the incident field in order to obtain an accurate approximation. The Rytov solution, however, in insensitive to the distance traveled in the perturbed medium. The accuracy of the approximation instead depends on the gradient of the ratio of the scattered to incident fields.

The behavior of the solutions in a layered waveguide is a bit more difficult to quantize. The true and background eigenfunctions no longer have the same form and the projected mode coefficients are difficult to interpret. However, through numerical examples, we found the mode functions can differ by up to 7%; at this limit, accurate representations of the true field will be obtained for ranges less than

25 km.

The information obtained from the two-layer test cases is used to estimate the magnitude and extent of perturbations permissible when the background sound speed depends on depth. The accuracy of the approximations depends both on the profile and the source-receiver configuration. If the receiver is in a shadow zone, the correct field structure is not well approximated. In general, however, if the receiver is well- illuminated, the behavior of the DWB and DWR fields (for a depth-dependent perturbation) follows that predicted in the two layer case. Accordingly, the extent to which the background profile can deviate from the true profile in an inhomogeneous environment can be estimated; therefore indicating the size and extent of profile perturbations which can be recovered in an inverse problem using either the DWB and DWR approximations to the scattered field.

The inverse algorithm was formulated as a Fourier inversion assuming the phase of the DWB kernel and the wavenumber to be Fourier transform variables. Because the kernel is written as a modal sum, no explicit expressions for the amplitude and phase were available; therefore, the analysis was completely numerical. Although the gross wavenumber dependence was determined and numerically removed from the amplitude and phase, the functions were necessarily averaged over wavenumber to smooth any local dependence. When the averaging process is applied to the phase, the information content of the Fourier constituents

is distorted; in effect the phase function is no longer contins the correct information on the perturbation. In addition, the phase was not monotonic in regions in which the waveguide was well-illuminated and so in these regions the inverse algorithm was no longer valid. As a result of these limitations (plus band-limiting), no perturbations were recovered using either the DWB or DWR scattered field. Therefore, although the inversion could be posed using other parameter configurations, we conclude that for a single source-receiver geometry, a wide-band Fourier inversion is not a valid formulation for recovering depth-dependent perturbation in the deep-ocean waveguide.

REFERENCES

Abramowitz, M., and I. A. Stegun, 1972, Handbook of Mathematical Functions, Dover, New York.

Bender, C. M., and Orszag, S. A., 1978, Advanced Mathematical Methoods for Scientists and Engineers, McGraw-Hill, New York.

Beydoun, W. B., and A. Tarantola, 1988, First Born and Rytov approximations: Modeling and inversion conditions in a canonical example, J. Acoust. Soc. of Am., **83**, No. 3, 1045-1055.

Beylkin, G., and M. L. Oristaglio, 1985, Distorted-Wave Born and Distorted-Wave Rytov Approximations, Optics Communications, **53**, No. 4, 213-216.

Born, M., 1926, Quantum mechanics of impact processes, Z. Physik **38**, 803-827.

Born, M., and E. Wolf, 1965, Principles of Optics, Pergamon Press, New York.

Brekhowskikh, L., and Yu. Lysanov, 1982, Fundamentals of Ocean Acoustics, Springer-Verlag, New York.

Brown, M. G., W. H. Munk, J. Spiesberger, and P. F. Worcester, 1980, Long range acoustics in the northwest Atlantic., J. Geophys. Res., **85**, 2699-2703.

Butkov, E., 1968, Mathematical Physics, Addison-Wesley Publishing, Reading, Massachusetts.

Chernov, L. A., 1960, Wave Propagation in a Random Medium, McGraw-Hill, New York.

Cohen, J. K., and N. Bleistein, 1977, An inverse method for determining small variations in propagation speed, SIAM J. Appl. Math. **32**, 784-799.

Davis, J. A., D. W. White, and R. Cavanagh, 1981, NORDA Parabolic Equation Workshop, NORDA Technical Note 143.

DeSanto, J.A., J. S. Perkins, and R. N. Baer, 1978, A correction to the parabolic equation, J. Acoust. Soc. Am., **64**, No. 6, 1664-1666.

DiNapoli, F. R. and R. L. Deavenport, 1979, Numerical models of underwater acoustic propagation, Ocean Acoustics, ed. by J. A. DeSanto, Topics in Current Physics, **8**, Springer-Verlag, New York.

Ewing, M., W. S. Jardetzky and F. Press, 1957, Elastic Waves in Layered Media, McGraw-Hill, New York.

Ewing, M., and J. L. Worzel, 1948, Long range sound transmission, Geol. Soc. Am., Mem. 27.

Fiddy, M. A., 1986, Inversion of optical scattered field data, J. Phys. D., Appl. Phys. **19**, 301-317.

Hardin, R. H., and F. D. Tappert, 1973, Applications of the split-step Fourier method to the numerical solution of nonlinear and variable coefficient wave equations, SIAM Rev. **15**, 423.

Leontovich, M. A. and V. A. Fock, 1946, Zh. Eksp. Teor. Fiz. **16**, 557-573, English transl., 1946, J. Phys. USSR **10, 13-24.**

Kamel, A., and L. B. Felsen, 1982, On the ray equivalent of a group of modes, J. Acoust. Soc. of Am. **71**, 1445-1452.

Keller, J. B., 1969, Accuracy and validity of the Born and Rytov approximations, J. Opt. Soc. Am., **59**, 1003-1004.

Mueller, R. K., M. Kaveh and G. Wade, 1979, Reconstructive Tomography and Applications to Ultrasonics, Proc. of the IEEE, **67**, No. 4, 567-587.

Munk, W. H. and C. Wunsch, 1979, Ocean acoustic tomography: a scheme for large scale monitoring, Deep Sea Res., **26**, 123-161.

Munk, W. H. and C. Wunsch, 1982, Up-down resolution in ocean acoustic tomography, Deep Sea Res., **29**, 1415-1436.

Munk, W. H. and C. Wunsch, 1983, Ocean acoustic tomography: rays and modes for large scale monitoring, Reviews of Geophys. and Space Phys., **21**, No. 4, 777-793.

Officer, C. B., 1966, Introduction to the Theory of Sound Transmission, McGraw-Hill, New York.

Pedersen, M. A., and D. F. Gorden, 1972, Normal-mode and ray theory applied to underwater acoustic conditions of extreme downward refraction, J. Acoust. Soc. Am. **51**, 323-368.

Porter, M., 1988, The KRAKEN Normal Mode Program (DRAFT), personal communication.

Raz, S., 1981, Direct reconstruction of velocity and density profiles from scattered field data, Geophys. **46**, No. 6, 832-836.

Rytov, S. M., 1937, Diffraction of light by ultrasonic waves, Izv., Akad. Nauk SSSR Ser. Fiz. **2**, 223-259. (In Russian)

Slaney, M., A. C. Kak and L. E. Larsen, 1984, Limitations of imaging with first-order diffraction tomography, IEEE Trans. on Microwave Theory and Techniques, **MTT-32**, No. 8, 860-873.

Spiesberger, J., R. Spindel and K. Metzger, 1980, Stability and identification of ocean acoustic multipaths, J. Acoust. Soc. Amer., **67**, 2011-2017.

Spiesberger, J., P. F. Worcester, 1983, Perturbations in travel time and ray geometry due to mesoscale disturbances: A comparison of exact and approximate calculations, J. Acoust. Soc. Amer., **74**, 219-225.

Tolstoy, I., and C. S. Clay, 1966, Ocean Acoustics, McGraw-Hill, New York.

Tolstoy, I., and C. S. Clay, 1987, Ocean Acoustics: Theory and Experiment in Underwater Sound, American Institute of Physics, Inc., New York.

Taner, M. T., F. Koehler, and R. E. Sheriff, 1979, Complex seismic trace analysis, Geophys., **44**, No. 6, 1041-1963.

Tappert, F. D., 1977, The Parabolic Approximation Method, in Wave Propagation and Underwater Acoustics, ed. by J. B. Keller and J. S. Papadakis, Lecture Notes in Physics, **70**, Springer-Verlag, New York.

Zapalowski, L., S. Leeman and M. A. Fiddy, 1985, Image reconstruction fidelity using the Born and Rytov approximations, Acoust. Imaging, **14**, Plenum Press, New York.

APPENDIX A:

Derivation of the Normal Mode Representation of the Field

The integral representation of the sound field of a point source contains the normal modes (discrete spectrum) as well as the continuous spectrum. The discrete spectrum constitutes the main contribution since the normal modes are only weakly attenuated, whereas the continuous spectrum rapidly attenuates with range. If we are in the far field of the source, then, to a good approximation, only the normal modes contribute significantly to the pressure field. In this appendix, the modal field representation is derived for a specific set of boundary conditions.

We begin with the inhomogeneous Helmholtz equation

$$\left[\nabla^2 + k_o^2 n_o^2(z)\right] P_o(k_o, r, r_o, z, z_o) = -\frac{\delta(r-r_o)\delta(z-z_o)}{2\pi r} \tag{A.1}$$

in cylindrical coordinates for an arbitrary source point, (r_o, z_o). The boundary conditions are chosen to be

$$P_o(k_o, r, r_o, z, z_o) \mid_{z=o} = 0, \qquad \frac{\partial}{\partial z} P_o(k_o, r, r_o, z, z_o) \mid_{z=h} = 0$$

where h is the width of the ocean waveguide.

The homogeneous form of Eq. (A.1) is separable and the pressure field of a wave outgoing from a source located at r_o can be written as

$$P_o(k_o,r,r_o,z,z_o) = C(z_o,\xi)H_o^{(2)}(\xi r)J_o(\xi r_o)\psi(z,\xi) \qquad r > r_o \qquad \text{(A.2.a)}$$

$$P_o(k_o,r,r_o,z,z_o) = C(z_o,\xi)H_o^{(2)}(\xi r_o)J_o(\xi r)\psi(z,\xi) \qquad r < r_o \qquad \text{(A.2.b)}$$

The time dependence was chosen to be $\exp(i\omega t)$. In the first equation $H_o^{(2)}(\xi r)$ constitutes a right-traveling wave. The second equation contains both right and left-traveling components, but at large r the right-going wave is only seen in its effect due to the coupling with Eq. (A.2.a). The range-dependent solution, which I will call $G(\xi r \mid \xi r_o)$ for simplicity, is derived in Appendix B. The depth dependent solution, $\psi(z,\xi)$, satisfies

$$\left[\frac{d^2}{dz^2} + (k_o^2 n_o^2(z) - \xi^2)\right]\psi(z,\xi) = 0 \qquad \text{(A.3)}$$

with boundary conditions

$$\psi(z,\xi)\Big|_{z=o} = 0 \qquad \frac{d}{dz}\psi(z,\xi)\Big|_{z=h} = 0\,.$$

This system is solvable only for specific values of the separation parameter, ξ.

Chosing two linearly independent solutions of Eq. (A.3) to be $\psi_1(z,\xi)$ and $\psi_2(z,\xi)$ then the depth dependent solution is written

$$\psi(z,\xi) = C_1\psi_1(z,\xi) + C_2\psi_2(z,\xi)\,, \qquad \text{(A.4)}$$

where C_1 and C_2 are constants. Eq. (A.4) and the boundary conditions will give the relationship between the coefficients for all ξ_n

$$C_1 = -C_2 \frac{\psi_2(0,\xi_n)}{\psi_1(0,\xi_n)}$$

and also the characteristic equation for the eigenvalues, ξ_n

$$\psi_1(0,\xi_n)\psi_2'(h,\xi_n) - \psi_2(0,\xi_n)\psi_1'(h,\xi_n) = 0\,. \tag{A.5}$$

The solution of the inhomogeneous equation can now be represented as the sum of normal modes

$$P_o(k_o,r,r_o,z,z_o) = \sum_n C(z_o,\xi_n)G(\xi_n r \mid \xi_n r_o)\psi(z,\xi_n)\,. \tag{A.6}$$

The excitation coefficients, $C(z_o,\xi_n)$, are found by substituting Eq. (A.6) into the inhomogeneous equation, (A.1).

$$\sum_n \frac{\partial^2}{\partial r^2}\left[C(z_o,\xi_n)G(\xi_n r \mid \xi_n r_o)\psi(z,\xi_n)\right] + \frac{1}{r}\frac{\partial}{\partial r}\left[C(z_o,\xi_n)G(\xi_n r \mid \xi_n r_o)\psi(z,\xi_n)\right]$$
$$+ \frac{\partial^2}{\partial z^2}\left[C(z_o,\xi_n)G(\xi_n r \mid \xi_n r_o)\psi(z,\xi_n)\right] + k_o^2 n_o^2(z)C(z_o,\xi_n)G(\xi_n r \mid \xi_n r_o)\psi(z,\xi_n)$$
$$= -\frac{\delta(r-r_o)\delta(z-z_o)}{2\pi r}\,. \tag{A.7}$$

Using the equation for $G(\xi_n r \mid \xi_n r_o)$,

$$\left[\frac{d^2}{dr^2} + \frac{1}{r}\frac{d}{dr} + {\xi_n}^2\right]G(\xi_n r \mid \xi_n r_o) = \frac{2i}{\pi r}\delta(r-r_o)\,, \tag{A.8}$$

Eq. (A.7) reduces to

$$\sum_n C(z_o,\xi_n)\psi(z,\xi_n) = \frac{i}{4}\delta(z-z_o)\,. \tag{A.9}$$

Multiplying by $\psi(z,\xi_m)$, integrating over the depth of the waveguide and using orthogonality of the normal modes gives

$$C(z_o,\xi_n) = \frac{i}{4}\frac{\psi(z_o,\xi_n)}{\int_0^h \psi(z,\xi_n)\psi(z,\xi_n)\,dz}. \tag{A.10}$$

Normalizing the $\psi's$ in such a way that the integral is equal to 1, $C(z_o,\xi_n)$ is equal to $\frac{i}{4}\psi(z_o,\xi_n)$, and the final solution is written as

$$P_o(k_o,r,r_o,z,z_o) = \frac{i}{4}\sum_n G(\xi_n r \mid \xi_n r_o)\psi(z,\xi_n)\psi(z_o,\xi_n)\,. \tag{A.11}$$

Substituting the $G(\xi_n r \mid \xi_n r_o)$ from Appendix B, the incident field modal solution is

$$P_o(k_o,r,r_o,z,z_o) = \frac{i}{4}\sum_n H_o^{(2)}(\xi_n r)J_o(\xi_n r_o)\psi(z,\xi_n)\psi(z_o,\xi_n) \qquad r>r_o$$

$$P_o(k_o,r,r_o,z,z_o) = \frac{i}{4}\sum_n H_o^{(2)}(\xi_n r_o)J_o(\xi_n r)\psi(z,\xi_n)\psi(z_o,\xi_n) \qquad r<r_o. \tag{A.12}$$

APPENDIX B:

Derivation of the Range Dependent Solution

Bessel's equation for an arbitrary source point, $r = r_o$, is

$$\left[\frac{d^2}{dr^2} + \frac{1}{r}\frac{d}{dr} + {\xi_n}^2\right] G(\xi_n r \mid \xi_n r_o) = \frac{2i}{\pi r}\delta(r - r_o)\,. \tag{B.1}$$

The zero order forward Hankel transform is defined to be

$$\tilde{g}(k_r) = \int_o^\infty g(r) J_o(k_r r)\, r\, dr$$

and the corresponding inverse transform is

$$g(r) = \int_o^\infty \tilde{g}(k_r) J_o(k_r r)\, k_r\, dk_r$$

where k_r is the radial wavenumber. Applying a Hankel transform to Eq. (B.1), integrating by parts twice and using the relationships between the zeroth and first order Bessel functions results in the transformed Green's function

$$\tilde{G} = \frac{2i}{\pi}\frac{J_o(k_r r_o)}{k_r^2 - {\xi_n}^2}\,. \tag{B.2}$$

Inverse transforming gives

$$G(\xi_n r \mid \xi_n r_o) = -\frac{2i}{\pi}\int_0^\infty \frac{J_o(k_r r_o) J_o(k_r r)}{k_r^2 - {\xi_n}^2} k_r\, dk_r\,. \tag{B.3}$$

Using the relationship between Bessel and Hankel functions

$$J_o(k_r r_o)J_o(k_r r) = \frac{1}{4}[\,H_o^{(1)}(k_r r_o) + H_o^{(2)}(k_r r_o)\,]\,[\,H_o^{(1)}(k_r r) + H_o^{(2)}(k_r r)\,] \quad \text{(B.4)}$$

to rewrite the integrand and the relation

$$H_o^{(1)}(-k_r r) = -H_o^{(2)}(k_r r) \quad \text{(B.5)}$$

to reduce the four integrals to two, gives

$$G(\xi_n r \mid \xi_n r_o) = -\frac{i}{2\pi}\int_{-\infty}^{\infty} \frac{H_o^{(1)}(k_r r_o)H_o^{(1)}(k_r r)k_r dk_r}{k_r^2 - {\xi_n}^2}$$

$$- \frac{i}{2\pi}\int_{-\infty}^{\infty} \frac{H_o^{(1)}(k_r r)H_o^{(2)}(k_r r_o)k_r dk_r}{k_r^2 - {\xi_n}^2}\,. \quad \text{(B.6)}$$

If we now change the integration along the real line into a contour integral by making k_r complex, the evaluation of these integrals is accomplished using the residue theorem. If the time dependence is chosen to be $e^{i\omega t}$, then the form of an outgoing wave is $e^{-ik_r r}$. Using the asymptotic form of the Hankel functions, these integrals can be rewritten as

$$G(\xi_n r \mid \xi_n r_o) \sim -\frac{1}{\pi^2}(r r_o)^{-1/2}\int_C \frac{e^{ik_r(r+r_o)}}{k_r^2 - {\xi_n}^2}dk_r$$

$$- \frac{1}{\pi^2}(r r_o)^{-1/2}\int_C \frac{e^{ik_r(r-r_o)}}{k_r^2 - {\xi_n}^2}dk_r\,. \quad \text{(B.7)}$$

The asymptotic forms are used simply to make the pole evaluation more transparent. In the first integral of Eq. (B.7), $r + r_o$ is always greater than 0; therefore, if k_r is positive imaginary, we have convergence in the upper half plane.

We have two poles at which to evaluate the integrand. Evaluation at the positive pole results in an incoming wave and so this solution is discarded. Evaluation at the negative pole gives the outgoing wave contribution. Asymptotically, the first integral becomes

$$\frac{i}{\pi\xi_n}(rr_o)^{-1/2}\, e^{-i\xi_n(r+r_o)}\,, \tag{B.8}$$

and therefore, the solution is

$$\frac{1}{2}H_o^{(2)}(\xi_n r_o)H_o^{(2)}(\xi_n r)\,. \tag{B.9}$$

The phase of the second integral looks like $k_r(r-r_o)$ and must be evaluated depending on whether r is greater than or less than r_o. For $r>r_o$, we have convergence in the upper half plane. Evaluation at $k_r=-\xi_n$ gives the outgoing wave and the solution is

$$\frac{1}{2}H_o^{(1)}(\xi_n r_o)H_o^{(2)}(\xi_n r)\,. \tag{B.10}$$

For $r<r_o$, we have convergence in the lower half plane. Evaluation at the positive pole gives the outgoing wave solution

$$\frac{1}{2}H_o^{(2)}(\xi_n r_o)H_o^{(1)}(\xi_n r)\,. \tag{B.11}$$

Summing Eqs. (B.9) and (B.10) and using Eq. (B.4), we obtain the solution for r greater r_o.

$$G(\xi_n r \mid \xi_n r_o) = \frac{1}{2} J_o(\xi_n r_o) H_o^{(2)}(\xi_n r) \qquad r > r_o \,. \tag{B.12}$$

Summing Eqs. (B.9) and (B.11) and using Eq. (B.4), we obtain the solution for r less than r_o

$$G(\xi_n r \mid \xi_n r_o) = \frac{1}{2} H_o^{(2)}(\xi_n r_o) J_o(\xi_n r) \qquad r < r_o \,. \tag{B.13}$$

Eqs. (B.12) and (B.13) are the range-dependent Green's function for a point source located at $r = r_o$.

Note that Eqs. (B.12) and (B.13) are a general result for $r_o \neq 0$. In the special (and usual) case where the source is located at $r_o = 0$, we see from Eq. (B.12) that we recover the usual radial Green's function

$$G(\xi_n r \mid \xi_n r_o) = \frac{1}{2} H_o^{(2)}(\xi_n r) \qquad r_o = 0 \,. \tag{B.14}$$

APPENDIX C:

Derivation of the Full DWR Solution

The DWR approximation is derived by first assuming the total field solution can be written as

$$P(k_o,r,r_o,z,z_o) = P_o(k_o,r,r_o,z,z_o)e^{\Phi(k_o,r,r_o,z,z_o)}, \tag{C.1}$$

where $P_o(k_o,r,r_o,z,z_o)$ is a known incident field and $\Phi(k_o,r,r_o,z,z_o)$ is a complex phase function. Substituting Eq. (C.1) into the Helmholtz equation, (1), and performing the differentiation gives

$$\left[\nabla^2 + \left(\nabla^2\Phi + (\nabla\Phi)^2 + k_o^2 n^2(r,z)\right)\right]P_o + 2\,\nabla P_o\cdot\nabla\Phi = -\frac{\delta(r-r_o)\delta(z-z_o)}{2\pi r}e^{-\Phi}. \tag{C.2}$$

From Chapter 2, we know the incident field satisfies

$$\left[\nabla^2 + k_o^2 n_o^2(z)\right]P_o = -\frac{\delta(r-r_o)\delta(z-z_o)}{2\pi r}. \tag{C.3}$$

Therefore, by evaluating $e^{-\Phi}$ at the source (Φ is zero at the source because the scattered field is zero), Eq. (C.2) can be reduced to

$$P_o\,\nabla^2\Phi + 2\,\nabla P_o\cdot\nabla\Phi = -P_o\,(\nabla\Phi)^2 - k_o^2(n^2(r,z) - n_o^2(z))P_o\,. \tag{C.4}$$

We would like to write Eq. (C.4) in the form of a Helmholtz equation and solve for Φ using our Green's function, P_o. Away from the source, we can set

$$P_o \nabla^2\Phi + 2\nabla P_o \cdot \nabla\Phi = \left[\nabla^2 + k_o^2 n_o^2(z)\right](P_o\Phi) \tag{C.5}$$

so using Eq. (C.5) our differential equation, (C.4), becomes

$$\left[\nabla^2 + k_o^2 n_o^2(z)\right](P_o\Phi) = -P_o\,(\nabla\Phi)^2 - k_o^2(n^2(r,z) - n_o^2(z))P_o\,. \tag{C.6}$$

Therefore, the complex phase function, Φ, is given by the non-linear integral equation

$$\Phi = \frac{2\pi k_o^2}{P_o}\int_0^\infty\int_0^h P_o(k_o,r,r',z,z')(n^2(r,z) - n_o^2(z))P_o(k_o,r',r_o,z',z_o)r'\,dr'\,dz'$$
$$+ \frac{k_o^2}{P_o}\int_0^\infty\int_0^h P_o(k_o,r,r',z,z')[\nabla\Phi(r',z')]^2 P_o(k_o,r',r_o,z',z_o)r'\,dr'\,dz'\,. \tag{C.7}$$

To obtain the *first* DWR approximation, we expand the complex phase in powers of ϵ

$$\Phi(k_o,r,r_o,z,z_o) = \phi_1 + \phi_2 + \cdots \tag{C.8}$$

and use Eq. (4) (the expansion on the difference of the squares of the index of refraction). We substitute the expansions into Eq. (C.7), and equate powers of ϵ.

The second line in Eq. (C.7) is assumed to be order ϵ^2 due to the square of the phase gradient. This suggests that the field must vary smoothly in order for the *first* DWR approximation to be valid. The first integral has one term of order ϵ; therefore, to $O(\epsilon)$, the complex phase is approximated as

$$\Phi(k_o,r,r_o,z,z_o) \sim \phi_1(k_o,r,r_o,z,z_o)$$

$$= \frac{2\pi k_o^2}{P_o} \int_o^\infty \int_o^h P_o(k_o,r,r',z,z') n_1(r',z') P_o(k_o,r',r_o,z',z_o) r' dr' dz' \tag{C.9}$$

and the *first* DWR approximation is

$$P_1^{(R)} = P_o e^{\phi_1} \tag{C.10}$$

as derived from the *first* DWB in Chapter 2.

APPENDIX D:

Evaluation of the Range-Dependent Solution

As defined in chapter 2, the range-dependent solution for a point source located at $r = 0$ is given by

$$I(n,m) = H_o^{(2)}(\xi_n r)\int_o^r J_o(\xi_n r')H_o^{(2)}(\xi_m r')r'\,dr' + J_o(\xi_n r)\int_r^\infty H_o^{(2)}(\xi_n r')H_o^{(2)}(\xi_m r')r'\,dr' . \tag{D.1}$$

For clarity in the evaluation, the first integral is defined to be I_1 and the second to be I_2. The integrals are evaluated differently depending on whether $\xi_n = \xi_m$ or $\xi_n \neq \xi_m$.

For $\xi_n \neq \xi_m$, the integrals are evaluated as follows. We know $J_o(\xi_n r)$ and $H_o^{(2)}(\xi_m r)$ satisfy Bessel's equation. Choosing $x(r)$ and $y(r)$ to represent any Bessel functions, we write

$$x'' + \frac{1}{r}x' + \xi_n{}^2 x = 0$$

and

$$y'' + \frac{1}{r}y' + \xi_m{}^2 y = 0.$$

Multiplying the first equation by $r\,y$, the second by $r\,x$, subtracting the two equations and combining terms gives

$$r\left[y\,x'' - x\,y''\right] + x'\,y - y'\,x = (\xi_n{}^2 - \xi_m{}^2)\,r\,x\,y$$

or

$$\left[r(x\,y' - y\,x')\right]' = \left[\xi_n{}^2 - \xi_m{}^2\right] r\,x\,y\,.$$

To evaluate the first integral in Eq. (D.1), we set $J_o(\xi_n r) = x$, $H_o^{(2)}(\xi_m r) = y$ and integrate from 0 to r to obtain

$$\int_o^r J_o(\xi_n r')H_o^{(2)}(\xi_m r')r'\,dr' = \frac{\left[r'\,\xi_m J_o(\xi_n r')\,H_1^{(2)}(\xi_n r') - r'\,\xi_n J_1(\xi_n r')H_o^{(2)}(\xi_n r')\right]\Big|_o^r}{\xi_n{}^2 - \xi_m{}^2}. \tag{D.2}$$

The solution of the second integral is obtained in a similar manner. Multiplying the terms by their respective constants, I_1 and I_2 become

$$I_1 = \frac{H_o^{(2)}(\xi_n r)}{\xi_n{}^2 - \xi_m{}^2}\left[\xi_m r' H_1^{(2)}(\xi_m r')J_o(\xi_n r') - \xi_n r' J_1(\xi_n r')H_o^{(2)}(\xi_m r')\right]\Big|_o^r \tag{D.3}$$

$$I_2 = \frac{J_o(\xi_n r)}{\xi_n{}^2 - \xi_m{}^2}\left[\xi_m r' H_1^{(2)}(\xi_m r')H_o^{(2)}(\xi_n r') - \xi_n r' H_1^{(2)}(\xi_n r')H_o^{(2)}(\xi_m r')\right]\Big|_r^\infty.$$

Summing the contributions from the limit at r gives

$$I\Big|_r = I_1\Big|^r + I_2\Big|_r$$

$$= \frac{\xi_n r}{\xi_m{}^2 - \xi_n{}^2} H_o^{(2)}(\xi_m r)\left[J_o(\xi_n r)H_1^{(2)}(\xi_n r) - J_1(\xi_n r)H_o^{(2)}(\xi_n r)\right]. \tag{D.4}$$

Substituting the relations

$$J_o(\xi_n r) = \frac{1}{2}\left[H_o^{(1)}(\xi_n r) + H_o^{(2)}(\xi_n r)\right]$$

$$J_1(\xi_n r) = \frac{1}{2}\left[H_1^{(1)}(\xi_n r) + H_1^{(2)}(\xi_n r)\right] \tag{D.5}$$

into Eq. (D.4) and recognizing the Wronskian

$$-\frac{1}{2}\left[H_o^{(2)}(\xi_n r)H_1^{(1)}(\xi_n r) - H_1^{(2)}(\xi_n r)H_o^{(1)}(\xi_n r)\right] = \frac{2i}{\pi\xi_n r}, \tag{D.6}$$

we obtain the result

$$I(n,m)\Big|_r = \frac{2i}{\pi}\frac{H_o^{(2)}(\xi_m r)}{\xi_n{}^2 - \xi_m{}^2}. \tag{D.7}$$

Evaluation of I_1 at zero gives 0. Evaluation of I_2 at $r = \infty$ is zero assuming that ξ_n and ξ_m have a small negative imaginary part. The solution then for $\xi_n \neq \xi_m$ is given by Eq. (D.7).

The evaluation for $\xi_n = \xi_m$ is somewhat more complicated. Setting $\xi_m = \xi_n$ explicitly in the integrals gives

$$I(n,n) = H_o^{(2)}(\xi_n r)\int_o^r J_o(\xi_n r')H_o^{(2)}(\xi_n r')r'\,dr' + J_o(\xi_n r)\int_r^\infty H_o^{(2)}(\xi_n r')H_o^{(2)}(\xi_n r')r'\,dr'. \tag{D.8}$$

The first step is to make a change of variables. Setting $y = \xi_n r'$ and $dr' = dy/\xi_n$, the integrals become

$$I = \frac{H_o^{(2)}(\xi_n r)}{{\xi_n}^2} \int_o^{\xi_n r} J_o(y) H_o^{(2)}(y) y dy + \frac{J_o(\xi_n r)}{{\xi_n}^2} \int_{\xi_n r}^{\infty} H_o^{(2)}(y) H_o^{(2)}(y) y dy \,. \tag{D.9}$$

Again, we define the first integral as I_1 and the second as I_2 and integrate by parts. To evaluate I_1, we write

$$u = J_o(y) H_o^{(2)}(y) \qquad du = -\left[J_o(y) H_1^{(2)}(y) + J_1(y) H_o^{(2)}(y) \right] dy$$

$$dv = y dy \qquad v = \frac{y^2}{2}$$

to obtain

$$I_1 = \frac{H_o^{(2)}(\xi_n r)}{{\xi_n}^2} \cdot \left[\frac{y^2}{2} J_o(y) H_o^{(2)}(y) \Big|_o^{\xi_n r} - \int_o^{\xi_n r} \frac{y^2}{2} [J_o(y) H_1^{(2)}(y) + J_1(y) H_o^{(2)}(y)] dy \right] \tag{D.10}$$

Evaluating the first term at $\xi_n r$, (the expression is zero at $y = 0$), we obtain

$$\frac{r^2 H_o^{(2)}(\xi_n r)}{2} J_o(\xi_n r) H_o^{(2)}(\xi_n r) \,. \tag{D.11}$$

To evaluate the remaining integral, I_{11}, in Eq. (D.10), we substitute Eqs. (D.5) for $J_o(y)$ and $J_1(y)$ and combine terms. The result is

$$I_{11} = -\frac{H_o^{(2)}(\xi_n r)}{{\xi_n}^2} \cdot \int_o^{\xi_n r} \frac{y^2}{4} \left[2 H_o^{(2)}(y) H_1^{(2)}(y) + H_o^{(1)}(y) H_1^{(2)}(y) + H_1^{(1)}(y) H_o^{(2)}(y) \right] dy \,. \tag{D.12}$$

Defining the first term as I_{111} and using Bessel's Equation

$$y^2 H_o^{(2)}(y) = -yH_o'^{(2)}(y) - y^2 H_o''^{(2)}(y) \tag{D.13}$$

we obtain

$$I_{111} = \frac{H_o^{(2)}(\xi_n r)}{2{\xi_n}^2} \int_o^{\xi_n r} \left[yH_o'^{(2)}(y) + y^2 H_o''^{(2)}(y) \right] H_o'^{(2)}(y)\, dy$$

$$= \frac{H_o^{(2)}(\xi_n r)}{2{\xi_n}^2} \int_o^{\xi_n r} \frac{d}{dy} \left[\frac{y^2}{2} (H_o'^{(2)}(y))^2 \right] dy\,. \tag{D.14}$$

Integrating and evaluating at the limits, I_{111} becomes

$$I_{111} = \frac{r^2}{4} H_o^{(2)}(\xi_n r) \left[H_1^{(2)}(\xi_n r) \right]^2. \tag{D.15}$$

Writing the last two terms as I_{112}, using the relations

$$H_o^{(1)}(y) = J_o(y) + iY_o(y)\ ,\ H_o^{(2)}(y) = J_o(y) - iY_o(y)$$
$$H_1^{(2)}(y) = J_1(y) - iY_1(y)\ ,\ H_1^{(1)}(y) = J_1(y) + iY_1(y) \tag{D.16}$$

and combining terms gives

$$I_{112} = -\frac{H_o^{(2)}(\xi_n r)}{2{\xi_n}^2} \int_o^{\xi_n r} \left[y^2 J_o(y) J_o'(y) + y^2\, Y_o(y)\, Y_o'(y) \right] dy\,. \tag{D.17}$$

Using Bessel's equation, I_{112} becomes

$$\frac{H_o^{(2)}(\xi_n r)}{4} r^2 \left[\left\{ J_1(\xi_n r) \right\}^2 + \left\{ Y_1(\xi_n r) \right\}^2 \right]. \tag{D.18}$$

The second integral in Eq. (D.9) is found using the same techniques, but the

evaluation is simplier because the integrand is the product of identical Bessel functions. The solution, found by integration by parts and Bessel's equation is

$$I_2 = -\frac{J_o(\xi_n r)r^2}{2}\left[(H_o^{(2)}(\xi_n r))^2 + (H_1^{(2)}(\xi_n r))^2\right] \tag{D.19}$$

The terms contributing to the solution, $I = I_1 + I_2$, are in Eqs. (D.11), (D.15), (D.18) and (D.19). Canceling like terms, we obtain

$$\begin{aligned} I = & -\frac{J_o(\xi_n r)r^2}{2}\left[H_1^{(2)}(\xi_n r)\right]^2 + \frac{H_o^{(2)}(\xi_n r)r^2}{4}\left[H_1^{(2)}(\xi_n r)\right]^2 \\ & + \frac{H_o^{(2)}(\xi_n r)r^2}{4}\left[J_1(\xi_n r)\right]^2 + \frac{H_o^{(2)}(\xi_n r)r^2}{4}\left[Y_1(\xi_n r)\right]^2 \end{aligned} \tag{D.20}$$

Writing $H_o^{(2)}(\xi_n r) = J_o(\xi_n r) - iY_o(\xi_n r)$ in the second term and recombining terms gives

$$I = -\frac{H_o^{(1)}(\xi_n r)r^2}{4}\left[H_1^{(2)}(\xi_n r)\right]^2 + \frac{H_o^{(2)}(\xi_n r)r^2}{4}\left[H_1^{(1)}(\xi_n r)\left(H_1^{(1)}(\xi_n r)\right)^*\right] \tag{D.21}$$

where * denotes complex conjugate. Now, $\left[H_1^{(1)}(\xi_n r)\right]^* = H_1^{(2)}(\xi_n{}^* r)$, so for real eigenvalues

$$I = -\frac{H_o^{(1)}(\xi_n r)r^2}{4}\left[H_1^{(2)}(\xi_n r)\right]^2 + \frac{H_o^{(2)}(\xi_n r)r^2}{4}\left[H_1^{(1)}(\xi_n r)H_1^{(2)}(\xi_n r)\right] \tag{D.22}$$

or recognizing the Wronskian

$$H_1^{(1)}(\xi_n r)H_1^{(2)}(\xi_n r) - H_o^{(1)}(\xi_n r)H_1^{(2)}(\xi_n r) = -\frac{4i}{\pi\xi_n r} \tag{D.23}$$

we obtain the solution when $\xi_n = \xi_m$ as

$$I = -\frac{ir}{\pi}\frac{H_1^{(2)}(\xi_n r)}{\xi_n} \tag{D.24}$$

Therefore, evaluation of the range integral for a depth-dependent profile results in the solutions

$$\frac{2i}{\pi}\frac{H_o^{(2)}(\xi_m r)}{\xi_m{}^2 - \xi_n{}^2}. \qquad \xi_n \neq \xi_m \tag{D.25.a}$$

$$-\frac{ir}{\pi}\frac{H_1^{(2)}(\xi_n r)}{\xi_n} \qquad \xi_n = \xi_m . \tag{D.25.b}$$

It is interesting to note that Eq. (D.25.b) also follows by applying l'Hospital's rule to Eq. (D.25.a), in which case the result is not confined to real eigenvalues.

APPENDIX E :

Modal Decomposition of the Perturbative Solutions

In this Appendix, we discuss the modal decomposition of the DWB and DWR solutions. The DWB and DWR mode coefficients are first derived for the full field solutions. These expressions are later reduced to that of a single mode calculation and the mode coefficients are given explicitly for the test cases in Chapter 3.

The DWB solution for a strictly depth-dependent profile is given in Eqs. (18) and the DWR solution in Eqs. (19). Multiplying both sides of the DWB solution by the eigenfunctions, $\psi(z,\xi_l)$, and integrating over the width of the waveguide, we obtain

$$\int_o^h P_1^{(B)}(k_o,r,0,z,z_o)\,\psi(z,\xi_l)\,dz = \int_o^h \Big[P_o(k_o,r,0,z,z_o) + P_{sn}(k_o,r,0,z,z_o)\Big]\psi(z,\xi_l)\,dz \qquad \xi_n = \xi_m \quad \text{(E.1.a)}$$

and

$$\int_o^h P_1^{(B)}(k_o,r,0,z,z_o)\,\psi(z,\xi_l)\,dz = \int_o^h \Big[P_o(k_o,r,0,z,z_o) + P_{snm}(k_o,r,0,z,z_o)\Big]\psi(z,\xi_l)\,dz \qquad \xi_n \neq \xi_m\,. \quad \text{(E.1.b)}$$

Perfor= $\int \Big[P_o(k_o,r,0,z,z_o) + P_{snm}(k_o,r,0,z,z_o)\Big]\psi(z,\xi_l)\,dz \qquad \xi_n \neq \xi_m\,.$ (E.1.b)

$$\int_o^h P_1^{(R)}(k_o, r, 0, z, z_o)\, \psi(z, \xi_l)\, dz$$

$$= \int_o^h \left[P_o(k_o, r, 0, z, z_o) \exp\left[\frac{P_{sn}}{P_o} \right] \right] \psi(z, \xi_l)\, dz \qquad \xi_n = \xi_m \qquad \text{(E.2.a)}$$

and

$$\int_o^h P_1^{(R)}(k_o, r, 0, z, z_o)\, \psi(z, \xi_l)\, dz$$

$$= \int_o^h \left[P_o(k_o, r, 0, z, z_o) \exp\left[\frac{P_{snm}}{P_o} \right] \right]. \qquad \text{(E.2.b)}$$

Because the eigenfunctions are orthonormal over the width of the waveguide, the dz integrals are 1 if $l = n$ and zero otherwise. Eqs. (E.1) and (E.2) are the general expressions used in determining the DWB and DWR mode coefficients. For simplicity, the expressions will now be evaluated for a single mode for the test cases discussed in Chapter 3.

The first example is of a constant velocity waveguide in which the perturbation spans the entire waveguide. Eqs. (E.1.b) and (E.2.b) do not contribute because the perturbation is constant. In addition, we are finding solutions for only 1 mode. From Eq. (26), the eigenfunctions are sines; replacing the ψ's with sines (see also Eq. (18.b)) in Eq. (E.1.a) and combining terms, the single mode Born expression becomes

$$\left(\frac{2}{h}\right)^{1/2} \int_o^h P_{11}{}^{(B)}(k_o, r, 0, z, z_o) \sin\lambda_1 z \, dz = \frac{i}{4} H_o^{(2)}(\xi_1 r)$$

$$\cdot \left(\frac{2}{h}\right)^{3/2} \sin\left(\frac{\pi z_o}{2h}\right) \int_o^h \left[\sin\left(\frac{\pi z}{2h}\right) - \frac{irk_o^2 n_1}{2\xi_1} \sin\left(\frac{\pi z}{2h}\right)\right] \sin\left(\frac{\pi z}{2h}\right) dz \qquad \text{(E.3)}$$

where λ_1 has been replaced by $\frac{\pi}{2h}$. Integrating the right hand side yields

$$\left(\frac{2}{h}\right)^{1/2} \int_o^h P_{11}{}^{(B)}(k_o, r, 0, z, z_o) \sin\left(\frac{\pi z}{2h}\right) dz$$

$$= \frac{i}{4} H_o^{(2)}(\xi_1 r) \left(\frac{2}{h}\right)^{1/2} \sin\left(\frac{\pi z_o}{2h}\right) \left[1 - \frac{irk_o^2 n_1}{2\xi_1}\right]. \qquad \text{(E.4)}$$

Dividing through by the range solution, $\frac{i}{4} H_o^{(2)}(\xi_1 r)$, the resulting Born mode coefficient, C_{1B}, in a constant velocity waveguide is given by

$$C_{1B} = \left(\frac{2}{h}\right)^{1/2} \sin\left(\frac{\pi z_o}{2h}\right) \left[1 + \frac{irk_o^2 n_1}{2\xi_1}\right]. \qquad \text{(E.5)}$$

Because the Rytov solution is essentially an exponentiated Born, to avoid the simple analysis, we will simply state the result. The Rytov mode coefficient, C_{1R} is

$$C_{1R} = \left(\frac{2}{h}\right)^{1/2} \sin\left(\frac{\pi z_o}{2h}\right) \exp\left[\frac{irk_o^2 n_1}{2\xi_1}\right]. \qquad \text{(E.6)}$$

The second example for which the first mode coefficient is derived is a two-layer waveguide. The velocity is constant in each layer and the background profile a

constant over the entire waveguide. Again, Eqs. (E.1.b) and (E.2.b) are not evaluated because we are interested in single mode analytic solutions.

In this case, the mode functions are not the same for the true and background profiles. The true mode functions are given in Eq. (38) and the background modes are sines. The Born and Rytov approximations, although constructed from the guess modes, are multiplied by the true mode functions to obtain the mode coefficients.

From Eqs. (E.1.a), (38) and (40.a), the Born projection equation is

$$\int_o^h P_1^{(B)}(k_o,r,0,z,z_o)\psi_1(z,\xi)\,dz = \frac{i}{2h}\sin(\frac{\pi z_o}{2h})H_o^{(2)}(\xi_1 r)\sqrt{A_1}$$

$$\cdot\left[\frac{\cos\lambda_{o1}(h-z_1)}{\sin\lambda_{11}z_1}\int_o^{z_1}\sin(\frac{\pi z}{2h})\sin\lambda_{11}\,dz + \int_{z_1}^h \sin(\frac{\pi z}{2h})\cos\lambda_{o1}(h-z)\,dz\right]$$

$$+\frac{ik_o^2 rn_1}{4\xi_1 h}H_1^{(2)}(\xi_1 r)\sin(\frac{\pi z_o}{2h})\left[\frac{z_1}{h} - \frac{\sin(\frac{\pi z_1}{h})}{\pi}\right]\sqrt{A_1}$$

$$\cdot\left[\frac{\cos\lambda_{o1}(h-z_1)}{\sin\lambda_{11}z_1}\int_o^{z_1}\sin(\frac{\pi z}{2h})\sin\lambda_{11}\,dz + \int_{z_1}^h \sin(\frac{\pi z}{2h})\cos\lambda_{o1}(h-z)\,dz\right]. \qquad \text{(E.7)}$$

Integrating, combining terms and dividing by the range solution yields

$$C_{1B} = \sqrt{A_1}\,\sin(\frac{\pi z_o}{2h})\left[1 + \frac{ik_o^2 rn_1}{2h\xi_1}\left(\frac{z_1}{h} - \frac{\sin(\frac{\pi z_1}{h})}{\pi}\right)\right] \qquad \text{(E.8)}$$

where $\sqrt{A_1}$ is given by

$$\sqrt{A_1} = \sqrt{A_1}\,16h^2\sin\left(\frac{\pi z_1}{2h}\right)\cos\lambda_{o1}(h-z_1)$$

$$\cdot\frac{\left[2h\lambda_{11}{}^2\lambda_{o1}\tan\lambda_{o1}(h-z_1)-2h\lambda_{o1}{}^2\lambda_{11}\cot\lambda_{11}z_1+\pi\left(\lambda_{o1}{}^2-\lambda_{11}{}^2\right)\cot\left(\frac{\pi z_1}{2h}\right)\right]}{\left(\pi^2-4h^2\lambda_{o1}{}^2\right)\left(\pi^2-4h^2\lambda_{11}{}^2\right)}. \qquad \text{(E.9)}$$

Accordingly, the Rytov is

$$C_{1_R} = \sqrt{A_1}\,\sin\left(\frac{\pi z_o}{2h}\right)\exp\left[\frac{ik_o^2 rn_1}{2h\xi_1}\left(\frac{z_1}{h}-\frac{\sin\left(\frac{\pi z_1}{h}\right)}{\pi}\right)\right]. \qquad \text{(E.10)}$$